THE ASTRONOMICAL JOURNAL, 129:1117–1162, 2005 February
© 2005. The American Astronomical Society. All rights reserved. Printed in U.S.A.

THE DEEP ECLIPTIC SURVEY: A SEARCH FOR KUIPER BELT OBJECTS AND CENTAURS. II. DYNAMICAL CLASSIFICATION, THE KUIPER BELT PLANE, AND THE CORE POPULATION

J. L. ELLIOT,[1,2,3,4] S. D. KERN,[1,2] K. B. CLANCY,[2] A. A. S. GULBIS,[2] R. L. MILLIS,[1,4] M. W. BUIE,[1,4] L. H. WASSERMAN,[1,4] E. I. CHIANG,[1,5,6] A. B. JORDAN,[1,5,7] D. E. TRILLING,[1,8,9] AND K. J. MEECH[10]

Received 2004 July 20; accepted 2004 November 12

ABSTRACT

The Deep Ecliptic Survey (DES)—a search optimized for the discovery of Kuiper belt objects (KBOs) with the Blanco and Mayall 4 m telescopes at the Cerro Tololo Inter-American Observatory and Kitt Peak National Observatory—has covered 550 deg^2 from its inception in 1998 through the end of 2003. This survey has a mean 50% sensitivity at *VR* magnitude 22.5. We report here the discoveries of 320 designated KBOs and Centaurs for the period 2000 March through 2003 December and describe improvements to our discovery and recovery procedures. Our data and the data products needed to reproduce our analyses in this paper are available through the NOAO survey database. Here we present a dynamical classification scheme, based on the behavior of orbital integrations over 10 Myr. The dynamical classes, in order of testing, are "Resonant," "Centaur," "Scattered-Near," "Scattered-Extended," and "Classical." (These terms are capitalized when referring to our rigorous definitions.) Of the 382 total designated KBOs discovered by the DES, a subset of 196 objects have sufficiently accurate orbits for dynamical classification. Summary information is given for an additional 240 undesignated objects also discovered by the DES from its inception through the end of 2003. The number of classified DES objects (uncorrected for observational bias) are Classical, 96; Resonant, 54; Scattered-Near, 24; Scattered-Extended, 9; and Centaur, 13. We use subsets of the DES objects (which can have observational biases removed) and larger samples to perform dynamical analyses on the Kuiper belt. The first of these is a determination of the Kuiper belt plane (KBP), for which the Classical objects with inclinations less than 5° from the mean orbit pole yield a pole at R.A. = 273.°92 ± 0.°62 and decl. = 66.°70 ± 0.°20 (J2000), consistent with the invariable plane of the solar system. A general method for removing observational biases from the DES data set is presented and used to find a provisional magnitude distribution and the distribution of orbital inclinations relative to the KBP. A power-law model fit to the cumulative magnitude distribution of all KBOs discovered by the DES in the *VR* filter yields an index of 0.86 ± 0.10 (with the efficiency parameters for the DES fitted simultaneously with the population power law). With the DES sensitivity parameters fixed, we derive power-law indices of 0.74 ± 0.05, 0.52 ± 0.08, and 0.74 ± 0.15, respectively, for the Classical, Resonant, and Scattered classes. Plans for calibration of the DES detection efficiency function and DES magnitudes are discussed. The inclination distribution confirms the presence of "hot" and "cold" populations; when the geometric sin *i* factor is removed from the inclination distribution function, the cold population shows a concentrated "core" with a full width at half-maximum of approximately 4.°6, while the hot population appears as a "halo," extending beyond 30°. The inclination distribution is used to infer the KBO distribution in the sky, as a function of latitude relative to the KBP. This inferred latitude distribution is reasonably consistent with the latitude distribution derived from direct observation, but the agreement is not perfect. We find no clear boundary between the Classical and Scattered classes either in their orbital inclinations with respect to the KBP or in their power-law indices in their respective magnitude distributions. This leaves open the possibility that common processes have shaped the distribution of orbital parameters for the two classes.

Key words: astrometry — comets: general — Kuiper belt — methods: observational — planets and satellites: general — solar system: general — surveys

Online material: machine-readable tables

1. INTRODUCTION

The Kuiper belt is a large population of icy bodies that orbit the Sun beyond Neptune and is thought to have originated from a primordial disk in which the Sun and planets formed (Edgeworth 1949; Kuiper 1951; Joss 1973; Fernández 1980; Duncan et al. 1988; Jewitt & Luu 1993, 2000). The Kuiper belt objects (KBOs) remaining in nearly circular, low-inclination orbits—so-called classical KBOs—are presumably those that

[1] Visiting Astronomer, Kitt Peak National Observatory and Cerro Tololo Inter-American Observatory, National Optical Astronomy Observatory, which is operated by the Association of Universities for Research in Astronomy, Inc., under cooperative agreement with the National Science Foundation.

[2] Department of Earth, Atmospheric, and Planetary Sciences, Massachusetts Institute of Technology, 77 Massachusetts Avenue, Cambridge, MA 02139; jle@mit.edu, susank@mit.edu, kclancy@mit.edu, gulbis@mit.edu.

[3] Department of Physics, Massachusetts Institute of Technology, 77 Massachusetts Avenue, Cambridge, MA 02139.

[4] Lowell Observatory, 1400 West Mars Hill Road, Flagstaff, AZ 86001; rlm@lowell.edu, buie@lowell.edu, lhw@lowell.edu.

[5] Center for Integrative Planetary Sciences, Department of Astronomy, University of California at Berkeley, Berkeley, CA 94720; echiang@astron.berkeley.edu.

[6] Alfred P. Sloan Research Fellow.

[7] Current address: Department of Astrophysical and Planetary Sciences, Campus Box 391, University of Colorado, Boulder, CO 80309; jordanab@colorado.edu.

[8] Department of Physics and Astronomy, University of Pennsylvania, 209 South 33rd Street, Philadelphia, PA 19104.

[9] Current address: Steward Observatory, University of Arizona, 933 North Cherry Avenue, Tucson, AZ 85721; trilling@as.arizona.edu.

[10] Institute for Astronomy, 2680 Woodlawn Drive, Honolulu, HI 96822; meech@nihoa.ifa.hawaii.edu.

have not been significantly perturbed over the age of the solar system. Perturbation of the primordial belt included resonant capture and scattering of KBOs by an outwardly migrating Neptune (Malhotra 1995; Gomes 2003b). Even after its migration ended, Neptune has continued to erode the Kuiper belt by gravitational scattering (Holman & Wisdom 1993; Duncan et al. 1995; Duncan & Levison 1997), sending objects inward to become "Centaurs" or outward to become "scattered disk objects," or removing them from the solar system. Collisions among the KBOs have also sculpted the belt, influencing their size distribution (Kenyon & Luu 1998, 1999) and possibly forming binaries (Weidenschilling 2002). Mutual gravitational interactions may also form binaries (Goldreich et al. 2002; see also Sheppard & Jewitt 2004).

Insight into the dynamical processes—at work both in the past and today—can be gained through surveys of the Kuiper belt, which can establish the populations of dynamical classes and facilitate physical studies of the bodies within these classes. The most recently published survey is the *Hubble Space Telescope* (*HST*) survey of Bernstein et al. (2004), who also include the results of six earlier efforts (Chiang & Brown 1999; Trujillo et al. 2001; Gladman et al. 2001; Larsen et al. 2001; Allen et al. 2002; Trujillo & Brown 2003).

Here we present results of the Deep Ecliptic Survey (DES; Millis et al. 2002, hereafter Paper I). The survey employs the wide-field Mosaic cameras (Muller et al. 1998) on the 4 m Mayall and Blanco Telescopes to image the ecliptic in both the Northern and Southern Hemispheres. Granted formal survey status from 2001 to 2005 by the National Optical Astronomy Observatory (NOAO), the DES is designed to discover and determine the orbits of hundreds of Kuiper belt objects to understand how dynamical phase space is filled in the outermost solar system.

Important niches in this phase space are now known to be inhabited by virtue of DES data. Numerous mean motion resonances established by Neptune—not only the 3:2, but also the 4:3, 7:4, 2:1, and 5:2 resonances—are occupied by KBOs having large orbital eccentricities and inclinations (Chiang et al. 2003a, 2003b). Their existence testifies to Neptune's having migrated outward within its parent circumstellar disk (Malhotra 1995; Hahn & Malhotra 1999; Chiang & Jordan 2002). The first Neptunian Trojan was discovered by the DES collaboration; it is one of probably dozens of similarly sized Trojan librators whose total mass rivals, if not exceeds, that of the Jovian Trojans (Chiang et al. 2003a). Paper I also reported the first (2000 CR_{105}) of what is becoming a class of distant-perihelion objects, whose large eccentricities and inclinations are not easily understood by appealing to gravitational scatterings off the giant planets in their current configurations (Gladman et al. 2002; Gomes 2003a, 2003b; Brown et al. 2004).

In this paper, we extend our discussion and analysis of the DES data set to include objects discovered through the end of 2003. We report the addition of 320 KBOs and Centaurs to the sample of 62 designated objects described in Paper I. For analyses that require observational biases to be removed, we work with only the DES-discovered KBOs; in other cases, we can use the entire Minor Planet Center (MPC) database. To accomplish our analytical goals, we set forth a new, physically grounded classification scheme to sharpen the definitions of the traditional dynamical classes: "Resonant," "Centaur," "Scattered-Near," "Scattered-Extended," and "Classical." These classes are capitalized throughout the paper when referring to our rigorous definitions. We then choose subsets of objects from the MPC based on these dynamical classifications to establish the most thorough and precise determinations to date of the plane of the Kuiper belt (Collander-Brown et al. 2003; Brown & Pan 2004) and the distribution of orbital inclinations about this plane.

Search and recovery observations are documented in § 2. Our dynamical classification algorithm is described in § 3. A general strategy to remove observational biases from our data is laid out in § 4. Analytical determination of the pole of the Kuiper belt plane is made in § 5. Population distributions with respect to magnitude, orbital latitude, and orbital inclination (suitably debiased) are calculated in §§ 6–8. Finally, we discuss our results in § 9 and present our conclusions in § 10. Appendix A describes additional electronic resources supporting our analyses, Appendix B contains equations for integrations in Kuiper belt coordinate space, and Appendix C is a glossary of symbols used throughout the paper.

2. OBSERVATIONS

In this section, we discuss revisions to our search procedures since Paper I (cutoff date 2000 February) and update the results of our observations through the end of 2003. We also describe our recovery program, which has been implemented on several telescopes. For analyses in this paper we use the DES objects with 1998–2003 designations, based on measurements that appeared in the Lowell Observatory database[11] on 2004 April 15. These data include discoveries of 622 KBOs and Centaurs, of which 382 have been observed on more than one night and consequently have received designations by the MPC. An additional 100,000 measurements of moving objects of other types in the DES data have been reported to the MPC but will not be discussed here.

2.1. *Search*

Through the end of the period covered by this paper, the DES was assigned 88 nights with the Mosaic cameras (Muller et al. 1998) on the Mayall and Blanco 4 m telescopes at Kitt Peak National Observatory (KPNO) and the Cerro Tololo Inter-American Observatory (CTIO), respectively. Of the total 873 hours available, 655 hours (75%) were used for observations, with 23% of the time lost to weather and 2% lost to equipment failure. A summary of these observations listed by night appears in Table 1, which includes (1) sky conditions, (2) dark hours available and the percentage used, (3) the average seeing for all the frames, (4) the average limiting magnitude for the night (denoted by $\bar{m}_{2\sigma}$), (5) the total solid angle searched, (6) the number of KBOs and Centaurs discovered and, of those, the number given designations by the MPC, and (7) the number of search and recovery fields observed. All observations were made with a *VR* filter, with the exception of two runs (as noted) when this filter was unavailable. A *VR* filter provides approximately a factor of 2 increase in throughput relative to that of an *R* filter, with only a small increase in the sky background, owing to the exclusion of the OH bands above 7000 Å (Jewitt et al. 1996).

Figure 1 summarizes the sky coverage of our search fields, which were selected as described in Paper I. A complete tabulation of the search fields used for the analyses in this paper is contained in Table A3, the format of which is documented in Appendix A. Our observational strategy has been modified since 2002 February, from attempting two exposures of

[11] At http://asteroid.lowell.edu/.

TABLE 1

LOG OF OBSERVATIONS

UT Date	Obs. Site (4 m)	Weather[a]	Time Avail. (hr)	Time Used (%)	Average Seeing (arcsec)	Limiting Mag., $\bar{m}_{2\sigma}$	Search Solid Angle (deg^2)	Objects Found[b]	Objects Desig.[b]	Paired Search Fields[c]	Paired Recovery Fields[c]
2000 Apr 9	KPNO[d]	5	8.5	0	...	...	0	0	0	0	0
2000 Apr 10	KPNO[d]	4	8.5	100	1.6	22.8	10.8	11	0	30	8
2000 Jul 28	CTIO	1	10.6	100	1.4	23.3	16.6	10	7	46	0
2000 Jul 29	CTIO	1	10.6	100	1.9	22.8	15.8	4	0	44 (2s)	0
2000 Jul 30	CTIO	1	10.6	100	1.5	22.9	10.8	4	3	30 (15s)	0
2000 Jul 31	CTIO	1	10.6	100	1.5	23.3	19.1	3	1	53 (2s)	0
2000 Aug 24	CTIO	1	8.9	94	2.0	23.3	13.0	16	4	36 (1s)	0 (1s)
2000 Aug 25	CTIO[e]	1	9.2	97	1.5	23.7	13.3	12	4	37	1
2000 Aug 26	CTIO[e]	1	10.3	100	1.5	23.6	11.2	13	5	31 (1s)	11 (1s)
2000 Aug 27	CTIO[e]	1	10.2	100	1.6	23.5	12.6	15	4	35 (5s)	4
2000 Sep 19	KPNO	4	9.0	52	1.9	22.7	5.8	4	0	16 (7s)	4
2000 Sep 20	KPNO	4	9.0	41	2.2	22.6	2.5	1	0	7	9
2000 Sep 21	KPNO	4	9.0	78	2.0	23.0	7.2	6	0	20 (4s)	11
2000 Oct 22	KPNO	5	10.0	0	...	...	0	0	0	0	0
2000 Oct 23	KPNO	5	10.0	0	...	...	0	0	0	0	0
2001 Feb 25	KPNO	5	9.8	10	1.6	23.0	1.1	0	0	3	0
2001 Feb 26	KPNO	5	9.8	0	...	...	0	0	0	0	0
2001 Mar 25	KPNO	4	9.3	100	2.0	23.1	9.0	5	2	25 (5s)	6 (8s)
2001 Mar 26	KPNO	1	9.1	100	1.6	23.5	13.3	24	11	37 (2s)	1
2001 May 20	CTIO	4	11.3	25	1.8	23.3	0.0	0	0	0	7 (17s)
2001 May 21	CTIO	1	11.8	96	1.5	23.6	7.6	15	9	21	38
2001 May 22	CTIO	1	11.5	100	1.6	23.5	13.0	23	12	36	24 (1s)
2001 May 23	CTIO	1	11.2	100	1.5	23.7	16.9	23	11	47 (1s)	12 (3s)
2001 Aug 17	CTIO	5	10.6	0	...	...	0	0	0	0	0
2001 Aug 18	CTIO	1	10.6	100	1.7	23.3	14.0	15	8	39 (10sL)	1 (14s)
2001 Aug 19	CTIO	1	10.7	100	1.9	23.1	13.7	7	5	38 (10sL)	1 (14s)
2001 Aug 20	CTIO	1	10.3	95	1.6	23.5	12.6	13	7	35 (9sL, 2L)	0 (15s)
2001 Sep 12	KPNO	1	8.8	72	1.7	23.4	11.9	10	7	33	1
2001 Sep 13	KPNO	5	8.8	0	...	...	0	0	0	0	0
2001 Sep 14	KPNO	5	8.8	0	...	...	0	0	0	0	0
2001 Oct 19	KPNO	4	10.6	52	[f]	[f]	6.1	4	3	17 (12s)	2 (4s)
2001 Oct 20	KPNO	4	10.6	91	1.6	22.7	9.0	0	0	25 (17s)	12 (5s)
2001 Oct 21	KPNO	4	10.6	100	1.8	23.3	16.6	5	4	46 (9s)	4 (9s)
2002 Feb 6	KPNO	1	10.8	97	1.7	23.4	15.8	17	16	44 (6s)	0 (3s)
2002 Feb 7	KPNO	1	10.5	97	1.9	23.1	6.5	2	1	18 (59s, 2L)	1 (2s)
2002 Feb 8	KPNO	1	10.5	100	1.7	23.4	13.7	15	7	38 (18s, 2sL)	0 (3s)
2002 Mar 18	KPNO	4	8.7	77	2.0	22.9	3.6	5	2	10 (35s)	6
2002 Mar 19	KPNO	5	9.0	0	...	...	0	0	0	0	0
2002 Mar 20	KPNO	4	9.0	92	2.2	22.4	7.9	3	1	22 (2s)	10
2002 Apr 5	CTIO	1	9.9	100	1.6	23.7	11.9	10	10	33 (2s)	8 (4s)
2002 Apr 6	CTIO	1	9.9	100	1.5	23.7	7.2	6	6	20 (34s)	6 (8s)
2002 Apr 7	CTIO	1	9.8	100	1.6	23.6	7.9	7	3	22 (52s)	4 (1s)
2002 Apr 8	CTIO	1	9.8	100	1.6	23.8	13.7	15	13	38 (17s)	1 (2s)
2002 Aug 8	CTIO	1	10.5	100	1.6	23.2	6.5	0	0	18 (33s, 1sL)	0 (19s)
2002 Aug 9	CTIO	1	10.5	100	1.7	23.3	10.1	2	2	28 (23s, 1sL)	1 (19s)
2002 Aug 10	CTIO	1	10.5	100	1.5	23.5	1.8	2	2	5 (32s, 1sL)	1 (28s)
2002 Aug 11	CTIO	1	10.5	100	1.6	23.5	11.5	16	14	32 (7s, 1sL)	10 (19s)
2002 Nov 7	KPNO	1	10.3	100	1.6	23.5	14.0	21	16	39 (2s)	7 (4s)
2002 Nov 8	KPNO	4	10.3	22	1.7	22.8	0.0	0	0	0 (20s)	0 (5s)
2002 Nov 9	KPNO	4	10.3	42	1.8	23.3	6.5	6	3	18	0
2002 Dec 4	KPNO	1	5.6	86	1.3	23.7	8.3	9	6	23 (1s)	0
2002 Dec 5	KPNO	1	10.8	75	1.7	23.6	17.3	2	1	48 (10s)	2
2002 Dec 6	KPNO	4	10.8	89	2.0	22.8	16.6	0	0	46 (36s)	2
2002 Dec 7	KPNO	4	5.2	100	1.3	23.4	8.3	3	0	23 (23s)	0
2003 Mar 1	KPNO	5	9.8	0	...	...	0	0	0	0	0
2003 Mar 2	KPNO	5	9.8	0	...	...	0	0	0	0	0
2003 Mar 3	KPNO	6	9.8	0	...	...	0	0	0	0	0
2003 Mar 30	KPNO	1	8.8	94	2.1	22.7	11.2	5	5	31	5 (8s)
2003 Mar 31	KPNO	1	8.8	100	1.9	23.2	1.4	1	1	4 (63s)	0 (12s)
2003 Apr 1	KPNO	1	8.8	100	1.6	23.5	13.7	8	7	38 (3s)	0 (8s)
2003 May 30	CTIO	3	10.8	100	1.7	23.6	7.6	5	3	21 (21s)	16 (3s)
2003 May 31	CTIO	3	10.8	100	1.6	22.3	8.6	0	0	24 (21s)	5 (23s)
2003 June 1	CTIO	2	10.8	100	1.8	23.7	6.5	1	1	18 (25s)	4 (14s)

TABLE 1—*Continued*

UT Date	Obs. Site (4 m)	Weather[a]	Time Avail. (hr)	Time Used (%)	Average Seeing (arcsec)	Limiting Mag., $\bar{m}_{2\sigma}$	Search Solid Angle (deg^2)	Objects Found[b]	Objects Desig.[b]	Paired Search Fields[c]	Paired Recovery Fields[c]
2003 June 2.....	CTIO	4	10.8	58	1.9	22.9	5.8	9	9	16 (11s)	0 (18s)
2003 Aug 23.....	CTIO	2	10.1	50	1.7	23.7	5.4	7	5	15 (31s)	1
2003 Aug 24.....	CTIO	1	10.1	100	1.6	23.9	11.9	16	14	33 (29s)	0 (2s)
2003 Aug 25.....	CTIO	1	10.1	100	1.7	23.7	11.2	14	13	31 (37s)	0 (2s)
2003 Aug 26.....	CTIO	1	10.1	100	1.6	23.7	15.8	14	11	44 (4s)	1 (2s)
2003 Oct 22	KPNO	1	10.1	100	1.7	23.5	10.8	10	5	30 (1s)	14 (2s)
2003 Oct 23	KPNO	1	10.1	100	1.6	23.5	14.8	16	15	41 (2s)	0 (8s)
2003 Oct 24	KPNO	1	10.1	100	1.5	23.6	13.0	16	14	36 (1s)	8 (7s)
2003 Nov 20.....	KPNO	1	10.8	100	1.6	23.8	15.1	13	4	42 (1sL)	5 (4s)
2003 Nov 21.....	KPNO	1	10.8	100	1.4	23.8	11.2	17	1	31 (14s, 1sL)	8 (3s)
2003 Nov 22.....	KPNO	4	10.8	37	1.9	22.9	2.5	2	0	7 (5s, 1sL)	8 (2s)
2003 Nov 23.....	KPNO	1	10.8	100	2.8	22.7	4.3	1	0	12 (13s, 3sL)	4 (4s)
2003 Nov 24.....	KPNO	1	10.8	100	2.0	23.3	7.6	5	1	21 (14s, 1sL)	13 (1s)

NOTE.—All observations made in a *VR* filter (see Table 3 for specifications) unless otherwise noted.

[a] Weather key: (1) photometric; (2) clear; (3) thin cirrus; (4) variable clouds; (5) clouds/overcast; (6) iced shut.

[b] Objects include KBOs and Centaurs.

[c] Numbers in parentheses followed by "s" or "L" indicate additional unpaired frames (or frames paired on multiple nights) and prograde search fields acquired, respectively. We note that no KBOs were found in the prograde search fields.

[d] Observations made using Nearly-Mould *I* filter (center wavelength 8220 Å, passband FWHM 1930 Å).

[e] Observations made using Sloan r' filter (see Table 3 for specifications). The *VR* filter was used during the first night of this run, but it was unavailable for the other three nights.

[f] Information missing because of disk crash.

a field per run to three: a pair of frames on a single night and the third frame on the preceding or following night.[12] With this strategy, a suspected moving object can be confirmed, and the orbital arc on newly discovered KBOs and Centaurs is extended from ~2 hr (on a single night) to ~24 hr. This longer arc reduces the error in near-term extrapolated positions by approximately an order of magnitude, keeping objects available to smaller field instruments approximately 10 times longer after discovery than for the single-night search strategy. Also, the frame on the second night allows the MPC to issue a provisional designation, increasing the chances that others will observe the object.

Since the inception of the DES (through the end of 2003), we have surveyed approximately 12% of the solid angle within 6° of the ecliptic. This estimate of the coverage is complicated by the longevity of our survey. Consider the extreme case of two adjacent fields observed in the survey: field A and field B. Field A can be reobserved in subsequent lunations as new search area. This field must therefore be counted twice even though it is physically the same section of sky, because new KBOs will have moved into the field during the intervening time interval. Field B can also be observed as new search area. However, if field B is "downstream" (in the direction of KBO motion) from field A, some potential KBO orbits that fell within field A will also fall within field B at the time of observation. Thus, some KBOs in field A may later be found (or not found) in field B. Field B does not truly represent 100% new sky coverage.

This problem is greatest when the observations are separated by only one lunation: in this case, the greatest number of KBO orbits from field A fall within field B one month later. As the fields are further separated in sky location or in time, the fraction of all field B potential KBO orbits that also fell within field A decreases. From detailed examination of our typical observing cadence from month to month and year to year (shown in Table 1), we find that the amount of sky area affected by this "downstream" problem is no more than a few percent of the total survey. The precise magnitude of the "downstream" sky coverage area problem would have to be calculated through Monte Carlo modeling of KBO orbits and survey procedures, work that we have not done. We are confident, however, that the magnitude of this uncertainty is small compared with other sources of error (§ 9.6); hence, we ignore the "downstream" problem for the remainder of the analyses presented here.

[12] This is different from the three-frame strategy employed at the beginning of our survey (Paper I), for which we would record three frame sequences on the same night.

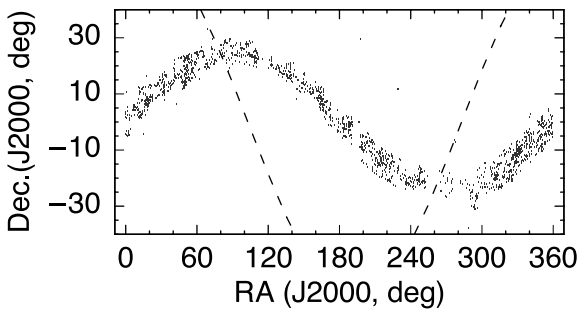

FIG. 1.—Search fields covered by the DES through the end of 2003. Each point represents a 0.36 deg^2 Mosaic frame, while the dashed lines represent the Galactic equator. The paucity of search fields near 270° in right ascension is due to the difficulty in searching high-density star fields near the Galactic center. Some fields have been observed in two or more lunations.

2.2. *Reduction of Mosaic Observations*

2.2.1. *Identification of Candidate KBOs*

As described in Paper I, moving objects are identified both with software and direct inspection. The first pass on a pair of

frames on a field is with automatic detection software, which has been modified over the lifetime of the DES but has had only a 20% success rate overall.[13] The first pass by the automatic detection software is followed by a sequence of two human inspections, each by a different person. Finally, a single individual carefully examines all putative discoveries of KBOs and Centaurs, and then he or she applies a consistent set of criteria to ensure that each paired set of images is a real moving object. The criteria used for this final examination are that (1) both images are evident in more than 1 pixel, (2) the rate and direction of inferred motion of the object is appropriate for that of a KBO or Centaur in the section of sky being searched, (3) the magnitude of the object remains consistent in the two frames, (4) neither image appears elongated (indicative of a fast-moving object that has been erroneously paired), and (5) the object appears on the third frame (if three exposures were recorded), at the position extrapolated from the positions on the original pair. Objects that pass this "final exam" are submitted to the MPC.

2.2.2. *Magnitudes*

The magnitudes assigned to DES objects are based on photometric reductions with respect to the red magnitudes in the USNO-A2.0 catalog, irrespective of the filter used for the Mosaic observations. After 2003 October 1, we switched to using the USNO-B1.0 catalog. DES magnitudes have been reported as "*R*" magnitudes to the MPC. As discussed in Paper I, individual discrepancies for the A2.0 and B1.0 catalog stars can be as large as 0.5 mag, but typical rms differences for all stars used in the reduction of a single Mosaic element are $\sim$0.1–0.2 mag for declinations north of -5° to -10° and $\sim$0.2–0.3 mag for more southern declinations. Better photometric accuracy should be possible, and a photometric calibration effort is in progress (as described in § 9.6.1).

2.3. *Recovery*

Of the putative KBOs and Centaurs submitted to the MPC, some have been observed on two or more nights (eligible for designation), while others need an additional observation for designation. Both types of objects need further observations to firmly establish their orbits. Our current objective is to obtain observations over three apparitions: two lunations in the discovery apparition, two lunations in the next apparition, and a further observation in the second apparition following the discovery (Buie et al. 2003). To achieve this, we have established a concerted recovery program with the following telescopes: the University of Hawaii 2.2 m (UH 2.2 m) at Mauna Kea, the Magellan 6.5 m (Baade and Clay) at Las Campanas, the Shane 3 m at Lick, and the Perkins 1.8 m at Lowell. Even with these efforts—and occasional recoveries with other telescopes, such as WIYN, the Steward 90 inch (2.3 m), and MDM—we have found it necessary to devote a significant amount of Mosaic time to recoveries. These recoveries at later apparitions are timed (if possible) to be near opposition so that a recovery field can also be used as a distinct search field. Table 2 details the instruments and recovery efforts for each telescope. Details for the filters used for the discoveries and recoveries can be found in Table 3.

[13] One reason for the low success rate of the automatic detection software is its operation on only a pair of frames—rather than the three- to five-frame sequence used by other surveys (e.g., Trujillo et al. 2001; Stokes et al. 2002).

We use the Bernstein & Khushalani (2000) method for calculating the initial orbits of our objects, since this approach yields error estimates for the orbital parameters (see Virtanen et al. 2003 and Paper I for a comparison with other approaches). These uncertainties guide our decision of which telescope and instrument combination should be employed for the recovery observations. Depending on the quality of the night, moonlight, telescope, and instrument, objects are selected based on their magnitudes and positional error ellipses. In general we use half the field of view of the instrument to define the cutoff for objects targeted (at the 1–2 σ level for their positional error). Objects are followed until their orbits are accurate enough for our purpose, that is, dynamical classification—although even greater accuracy is required for other goals, for example, occultation predictions (Elliot & Kern 2003). The positions and magnitudes, reported as *R*-filter observations, are submitted to the MPC. Of the 16,000 (nondiscovery) measurements of KBOs in the MPC database, the DES has contributed about 3000 (prior to 2004 April 12). The recovery magnitudes are based on reductions with the USNO-A2.0 and -B1.0 catalogs. For the Raymond and Beverly Sackler Magellan Instant Camera (MagIC) on Magellan, which has only a 2.′4 field, sometimes the reported magnitudes are based on that of a single catalog star, resulting in typical errors between 0.1 and 0.3 mag.

Once orbits have been established, further recoveries are possible with "directed searches" of the archived data. In one recovery effort of this type with the Mosaic data, positional calculations showed 160 DES archive fields (pairs of frames) on which objects should be present but had not been reported in our initial search of the field. Of these, 66 objects were successfully recovered (or "precovered"). Fourteen of these should have been discovered in the original pass. The remaining 52 required directed information about where to look in the image to find the object: 40 were missed because the object was close to the magnitude limit of the field, and 12 were missed as a result of interference by a bright star or main-belt asteroid. The positions of the recovered objects were submitted to the MPC. Such searches can be repeated as improved orbits become available.

2.4. *Undesignated Objects*

As mentioned earlier, not all our discoveries of KBOs and Centaurs have received MPC provisional designations, because they were never observed on a second night, as a consequence of poor weather or inadequate access to appropriate telescopes. This problem was mitigated after adopting our two-night search strategy (§ 2.1). The undesignated objects cannot be ignored, however, since ignoring them for certain analyses—such as the magnitude and latitude distributions—would introduce a large "nonrecovery" bias. After all, the undesignated objects passed the "final exam" criteria discussed in § 2.2.1 (except for recovery on a second night) and became lost because of the vagaries of the recovery process. Discovery information that is essential for the analyses carried out in this paper is recorded in Table A4 (see Appendix A). The set of undesignated objects discovered in valid search fields by the DES is listed as sample 1.1 in Table 4. This table summarizes each sample of objects used in this paper; the remaining samples in Table 4 (denoted by "sample *n*...") will be discussed as they are needed.

In order to understand the undesignated objects as a group, we have compared some properties of the undesignated objects with those of the designated objects (sample 1.2) in Figure 2. For each of the three panels in Figure 2, the total number of Centaurs and KBOs discovered by the DES in each bin is

TABLE 2

RECOVERY TELESCOPES

Telescope	Aperture (m)	Instrument	Filter[a]	Scale (arcsec pixel^{-1})	FOV (arcmin)	Exp. Time (s)	Typical Seeing (arcsec)	Recov. Tries	Recov.[b]
Baade and Clay.....	6.5	MagIC	Sloan r'	0.069	2.4	120–180	0.3–1.1	138	109
		LDSS2	Harris R	0.378	7.5[c]	180	0.3–1.1		
Blanco and Mayall.....	4	Mosaic	VR	0.519[d]	36	240–300	1.0–1.5	[e]	[e]
WIYN.....	3.5	Mini-Mosaic	Sloan r'	0.14	9.6	300–1800	0.8–2.0	45	31
Shane.....	3	PFCam	Spinrad R	0.6[d]	10	1200	1.0+	87	45
MDM.....	2.4	SITe 2K × 4K SITe	Wide R	0.173	25	600	1.0–1.5	31	11
Steward.....	2.3	Bok direct imaging	Harris R	0.45	2–3	900	1.0–1.5	39	10
UH 2.2 m.....	2.2	Tek 2K × 2K	Kron-Cousins V	0.219	7.5	500–1200	0.5–1.1	230	140
		Lincoln Labs 2K × 4K	Kron-Cousins R	0.275[d]	9.4 × 18.7	500–1200	0.5–1.1		
Perkins.....	1.8	SITe 2K × 2K	Unfiltered, Kron-Cousins R, VR	0.15[f]	5	1200	1.6–1.8	179	75

NOTE.—Telescopes coordinated by the DES; observations were also made using the 2.6 m Nordic Optical Telescope (NOT) and the 2.5 m Isaac Newton Telescope (INT) prior to 2001.

[a] See Table 3 for center wavelengths and passbands.

[b] From 2001 January 1 to 2003 December 31.

[c] Circular field of view.

[d] Binned, 2 × 2.

[e] Recovery information for the Blanco and Mayall Telescopes appears in Table 1.

[f] Binned, 4 × 4.

TABLE 3
FILTER SPECIFICATIONS

Filter	Effective Wavelength (Å)	Passband FWHM (Å)
Kron-Cousins V	5450	836
VR	6100	2000
Sloan r'	6254	1388
Harris R	6300	1180
Kron-Cousins R	6460	1245
Wide R	6725	1325
Spinrad R	6993	850

represented by the sum of the open, gray, and black areas. The undesignated objects are represented by the open areas of the histogram, and the designated objects are represented by the sum of the black (dynamically classified, sample 1.2.1; see § 2.5) and gray (unclassified, sample 1.2.2) areas. For the purpose of the present discussion, we note that the errors in the orbital parameters are smaller for designated objects than for undesignated objects and smaller for dynamically classified objects than for unclassified objects. We also note that a significant number of designated objects are lost to present observational programs, since their positional errors have become too large for easy recovery with current instruments—although these should eventually be recovered in more extensive surveys. The short open, gray, and black bars at the top of each panel represent the mean of the undesignated, unclassified, and dynamically classified samples, respectively. The width of each bar is two standard deviations of the sample mean.

Figure 2*a* shows the differential magnitude distribution in 0.5 mag intervals. It is not surprising to note that undesignated objects have the faintest mean magnitude, since the recovery of fainter objects requires larger telescopes or better observing conditions. Figure 2*b* compares the three populations with respect to heliocentric discovery distance, and Figure 2*c* compares the three groups with respect to inclination. Each of these panels shows a trend, as the accuracy of the orbit improves. Taken as a group, the undesignated objects have smaller mean distances, which is likely a manifestation of a recovery bias against faster moving objects. The undesignated objects also show significantly larger derived inclinations. This is a result of the much larger inclination errors of the undesignated objects, which—coupled with the fact that inclinations are defined to always be positive—bias their mean to larger values.

2.5. *KBO Binaries*

It is noteworthy that of the 13 currently known KBO binaries, seven systems were originally detected as KBOs by the DES, including the first binary to be identified after Pluto, 1998 WW_{31} (Veillet et al. 2002). Only the comparatively wide pair 2003 UN_{284}, however, was recognized to be binary during the initial scrutiny of the DES frames (Millis 2003), because of the poorer resolution of the Mosaic data compared with some of the other instruments used for recovery and other follow-up observations. The binary natures of 2001 QT_{297} and 2003 QY_{90} (Elliot 2001a, 2001b, 2003; Osip et al. 2003) were noted in recovery observations by DES team members at Magellan (§ 2.3), and 2000 CF_{105}, 2000 CQ_{114}, and 2001 QC_{298} were found to be binary with *HST* (Noll et al. 2002a, 2002b; Noll 2003). Targeting these objects for *HST* would not have been possible without the recovery observations needed to establish high-quality orbits.

3. DYNAMICAL CLASSIFICATION

Traditionally, orbits of KBOs have been classified by noting their locations in the space of osculating eccentricity versus osculating semimajor axis. For example, "Plutinos" tend to lie on a line that is centered at semimajor axis $a \approx 39.4$ AU and extends from eccentricity $e \approx 0.1$ to $e \approx 0.3$. "Classical" KBOs do not lie in the vicinity of any low-order resonance and are considered to have small eccentricities, $e \leq 0.2$. "Scattered" KBOs are nonresonant KBOs with substantial eccentricities, $e > 0.2$.

Presently, no community-wide agreement exists as to precisely where these taxonomic boundaries should be drawn. Resonant widths as computed by Malhotra (1996) are commonly overlaid on an *a*-*e* plot to help judge whether an object inhabits a resonance, but these widths are approximate; they are computed with the restricted, circular, planar three-body model for the Sun-Neptune-KBO system, their resolution in eccentricity is crude, and most importantly, they do not account for the influence of the other orbital elements on resonance membership. The distinction between "classical" and "scattered" is, in our view, particularly murky, and since the former class might be thought to imply dynamical or chemical primitiveness, adoption of a particular labeling scheme can involve more than just semantics.

Here we set forth a new, simple, and quantitatively precise orbit classification procedure. The scheme is physically grounded and, while relatively free of biases, still reflects some of the current thinking about the different origins of various subpopulations. It has the added advantage of accounting for observational uncertainties in the fitted orbits. Some results from our procedure have been reported in Chiang et al. (2003a, 2003b) and Buie et al. (2003).

Our basic method is to integrate forward the trajectory of each object in the gravitational fields of the Sun and the four giant planets. By examining the object's long-term dynamical behavior, we place the object into one (and only one) of the five orbit classes described below. We list these classes in the order in which they should be tested for membership. All computations described in this section are performed in a heliocentric, J2000 coordinate system, and we perform this analysis for all KBOs and Centaurs in the MPC database (sample 2).

3.1. *Resonant KBOs*

"Resonant" KBOs are those objects for which one or more resonant arguments librate, that is, undergo bounded oscillations with time. Mean motion resonances (MMRs) established by Neptune are characterized by resonant arguments (angles) of the form $\phi = p\lambda - q\lambda_{\rm N} - m\varpi - n\Omega - r\varpi_{\rm N} - s\Omega_{\rm N}$, where λ, ϖ, and Ω are the mean longitude, longitude of perihelion, and longitude of the ascending node of the KBO, $\lambda_{\rm N}$, $\varpi_{\rm N}$, and $\Omega_{\rm N}$ are those same angles for Neptune, and p, q, m, n, r, and s are integers. By rotational invariance, $p - q - m - n - r - s = 0$. The strength of a particular resonance, that is, a measure of the depth of its potential well, is proportional to $e^{|m|}e_{\rm N}^{|r|}(\sin i)^{|n|}(\sin i_{\rm N})^{|s|}$, where e and i are respectively the orbital eccentricity and inclination and $e_{\rm N}$ and $i_{\rm N}$ are the eccentricity and inclination of Neptune's orbit. The order of a resonance equals $|p - q|$; high-order resonances are weaker than low-order resonances. In our current implementation, 107 different arguments are tested for libration; our chosen values for $\{p, q, m, n, r\}$ are listed in Table 5. We set $s = 0$ to neglect resonances whose strengths depend on the orbital inclination of Neptune; this decision has been made partly out of convenience,

TABLE 4

SAMPLES OF KBOs USED FOR ANALYSES

Sample	Objects	Description	Where Used	Use
1. DES	622	All objects discovered by the DES before 2003 Dec 31 that are highly likely to be KBOs and Centaurs	§ 2	
1.1. Undesignated	227[a]	Subset of DES objects discovered on search fields that have not qualified for provisional designations from the MPC	§ 2.4	Comparison of data samples
1.2. Designated	373[a]	Subset of DES objects discovered on search fields that have been designated by the MPC	§ 2.4	Comparison of data samples
1.2.1. Designated, classified	189	Subset of designated DES objects that are given a classification in § 3	§ 2.4	Comparison of data samples
1.2.2. Designated, unclassified	184	Subset of designated DES objects that are not given a classification in § 3	§ 2.4	Comparison of data samples
1.3. DES KBOs	512	All objects discovered by the DES on search fields excluding objects classified as Centaurs and unclassified objects with heliocentric distance less than 30 AU	§ 6.4, § 7, § 8.3, Table 14	Determination of magnitude distribution
1.3.1. *VR* filter	393	Subset of DES KBOs that were observed in a *VR* filter; provides a sample of consistent magnitudes	§ 6.3, § 6.4, Table 14	Determination of magnitude distribution
1.3.2. Designated	339	Subset of DES KBOs that are also designated by the MPC; provides objects with well-established orbital elements that can be debiased for this survey	§ 6.4, Table 14	Determination of latitude distribution
1.3.2.1. *VR* filter	270	Subset of designated DES KBOs that were observed in a *VR* filter; provides a sample of consistent magnitudes with well-constrained orbits	§ 6.4, Table 14	Determination of magnitude distribution
1.3.2.1.1. Classical	59	Subset of designated DES KBOs observed in *VR* that have been classified as Classical	§ 6.4, Table 14	Determination of magnitude distribution
1.3.2.1.2. Excited	59	Subset of designated DES KBOs observed in *VR* that have been classified as Resonant, Scattered-Near, or Scattered-Extended	§ 6.4, Table 14	Determination of magnitude distribution
1.3.2.1.2.1. Resonant	41	Subset of designated DES KBOs observed in *VR* that have been classified as Resonant	§ 6.4, Table 14	Determination of magnitude distribution
1.3.2.1.2.2. Scattered	18	Subset of designated DES KBOs observed in *VR* that have been classified as Scattered-Near or Scattered-Extended	§ 6.4, Table 14	Determination of magnitude distribution
1.3.2.2. $\sigma_i < 0.^{\circ}5$	240	Subset of designated DES KBOs with low error in inclination; provides a sample with accurate inclinations	§ 8.2, § 8.3, Table 15	Determination of inclination and latitude distributions
1.3.2.2.1. Classical	92	Subset of designated DES KBOs with low error in inclination that have been classified as Classical	§ 8.2	Determination of inclination distribution
1.3.2.2.2. Scattered	30	Subset of designated DES KBOs with low error in inclination that have been classified as Scattered-Near or Scattered-Extended	§ 8.2	Determination of inclination distribution
1.3.2.2.3. Resonant	52	Subset of designated DES KBOs with low error in inclination that have been classified as Resonant	§ 8.2	Determination of inclination distribution
1.3.2.2.4. Unclassified	66	Subset of designated DES KBOs with low error in inclination that have not been classified	§ 8.2	Determination of inclination distribution

TABLE 4—*Continued*

Sample	Objects	Description	Where Used	Use
2. All MPC	927	All objects listed by the MPC with perihelia beyond 5.5 AU; contains the largest number of KBOs and Centaurs	§ 5.4	Basic MPC sample for KBOs and Centaurs
2.1. BP[b]	728	All objects designated by the MPC as of 2003 Jul 1 and detected at heliocentric distances greater than 30 AU	§ 5.2, Table 12	Comparison of methods for determination of KBP
2.1.1. UpdatedBP	726	BP sample, excluding 1996 KW_1 and 2000 QM_{252} (linked to 2001 KO_{76} and 2002 PP_{149}, respectively)	§ 5.2, Table 12, § 5	Comparison of methods for determination of KBP
2.1.1.1. Limited BP	724	Subset of the Updated BP sample with high-latitude objects eliminated to keep computation times relatively short	§ 5.2, Table 12	Comparison of methods for determination of KBP
2.2. All MPC KBOs	872	Subset of MPC; excluding objects classified as Centaurs and unclassified objects with heliocentric distance less than 30 AU	§ 5.1, § 5.4, Table 13	Determination of KBP
2.2.1. $\sigma_p < 0.^{\circ}5$	565	Subset of all MPC KBOs having low pole errors; provides a large sample with accurate orbits	§ 5.4, Table 13	Determination of KBP
2.2.1.1. Classical	211	Subset of MPC KBOs with low pole errors that have been classified as Classical	§ 5.4, Table 13	Determination of KBP
2.2.1.1.1. $i_K < 5^{\circ}$	170	Subset of MPC Classical, low-inclination KBOs with low pole errors	§ 5.4, Table 13	Determination of KBP
2.2.1.1.1.1. $a < 44.01$ AU	85	Subset of MPC Classical, low-inclination KBOs with low pole errors, grouped by semimajor axis	§ 5.4, Table 13	Determination of KBP
2.2.1.1.1.2. $a > 44.01$ AU	85	Subset of MPC Classical, low-inclination KBOs with low pole errors, grouped by semimajor axis	§ 5.4, Table 13	Determination of KBP
2.2.1.2. Resonant (3:2)	66	Subset of all MPC KBOs, with low pole errors, in all 3:2 resonances (Table 5) with Neptune	§ 5.4, Table 13	Determination of KBP

[a] These samples represent DES objects discovered in valid search fields and do not include designations of 22 serendipitous discoveries in recovery fields, which bring the total number of undesignated objects to 239 and designated objects to 383 (with the subsets of classified and unclassified being 196 and 187, respectively).

[b] The object sample used by Brown & Pan (2004).

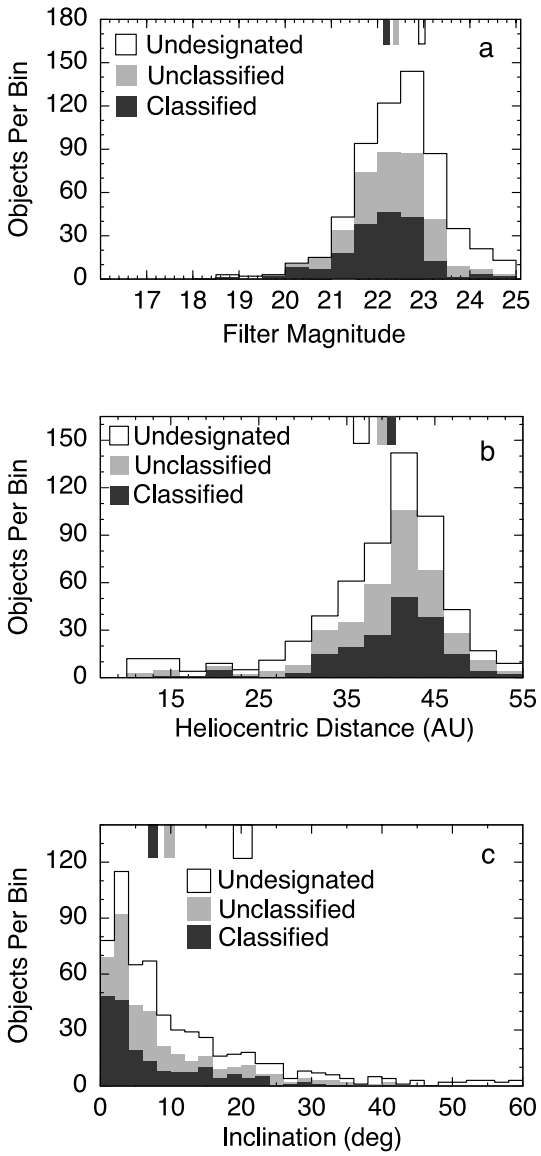

FIG. 2.—Comparison of objects with different degrees of orbital accuracy, ranging from undesignated to dynamically classified objects. The total number of Centaurs and KBOs discovered by the DES in each bin (of each panel) is represented by the combined black, gray, and open areas (i.e., the histograms have been stacked on top of each other, rather than overplotted). The units on the ordinate are the number of objects for the binned interval of the abscissa, and histograms are plotted for (*a*) apparent magnitude, (*b*) heliocentric distance, and (*c*) inclination. Working from less secure to more secure orbits, (1) the open areas of the histogram represent those objects without provisional designations, (2) the gray areas represent those objects with provisional designations but which are not yet dynamically classified, and (3) the black areas represent objects with secure dynamical classifications. The goal of the DES is to have a total of 500 objects with secure dynamical classifications (the total black area in each of the three panels; we currently have 189). The three short bars at the top of each panel indicate the mean and $\pm 1\ \sigma$ confidence limits for the three different sets of objects. Taken as a group, we see that the undesignated objects are systematically fainter, lie at smaller heliocentric distances, and have a systematic bias for larger inclination solutions. The differences in mean magnitude and heliocentric distance can be attributed to the increasing difficulty for recovery of fainter objects and faster moving objects, while the much higher mean inclination can be attributed to the systematic bias toward larger inclinations for objects with short observational arcs (i.e., 2–24 hr). The six undesignated objects in (*a*) that have magnitudes 19.5 or brighter were moving at rates ranging between 5.″3 and 13.″3 hr^{-1} at the time of discovery, indicating that these objects are either Centaurs or KBOs in highly eccentric orbits (near perihelion). This faster than average motion, possibly unusual orbits, and the limitations of our recovery program contributed to the loss of these objects. See § 2.4.

and partly because such resonances are typically weaker than MMRs that depend on the often substantial orbital inclinations of KBOs. Resonances of order ≤ 4 are included. Resonances as distant from Neptune as the 5:1 MMR at $a \approx 88$ AU and as near to Neptune as the 6:5 MMR at $a \approx 34$ AU are tested for membership. We do not test for membership in first-order resonances situated closer to Neptune than the 6:5, since these overlap and give rise to chaotic, planet-crossing motion. We do, however, test for the existence of Neptunian Trojans inhabiting the 1:1 MMR.

3.2. *Nonresonant KBOs*

An object for which all 107 arguments circulate (run the full gamut between 0 and 2π) is deemed "nonresonant." We distinguish the following four classes of nonresonant objects.

3.2.1. *Centaurs*

"Centaurs" are nonresonant objects whose osculating perihelia are less than the osculating semimajor axis of Neptune at any time during the integration. This definition is intended to be synonymous with "planet-crossing" and to suggest dynamically short lives—it is close to the common definition of a Centaur to be "an object that orbits the Sun between Jupiter and Neptune." See Tiscareno & Malhotra (2003) for a detailed discussion of the dynamics of Centaurs.

3.2.2. *Scattered-Near*

"Scattered-Near" KBOs are nonresonant, non–planet-crossing objects characterized by time-averaged Tisserand parameters less than 3, relative to Neptune. We evaluate the instantaneous Tisserand parameter, T, as

$$T = \frac{a_{\mathrm{N}}}{a} + 2\cos i_{\mathrm{kN}} \sqrt{(a/a_{\mathrm{N}})(1-e^2)}, \qquad (1)$$

where e and a refer to the osculating elements of the KBO, a_{N} is the osculating semimajor axis of Neptune, and i_{kN} is the osculating mutual inclination between the orbit of the KBO and that of Neptune. In deciding whether an object is a Scattered-Near KBO, we employ the value of T time-averaged over the duration of the integration. In the restricted, circular, three-body problem—an approximation to the Sun-Neptune-KBO system—an object whose nearly conserved Tisserand parameter is less than 3 and whose semimajor axis is greater than Neptune's can possess a perihelion inside Neptune's orbit, that is, be planet-crossing. This is a statement of principle, not necessarily one of practice. One could attribute, in principle, dynamically hot orbits of Scattered-Near KBOs to previous close encounters with Neptune, with the latter body in its current orbit. Whether such an explanation works in practice for any given Scattered-Near KBO depends on whether, after the putative scattering event, the perihelion of the object could have been raised to avoid further encounters.

3.2.3. *Scattered-Extended*

"Scattered-Extended" objects have time-averaged Tisserand parameters greater than 3 and time-averaged eccentricities greater than 0.2. This class is motivated by objects such as 2000 CR_{105} (Paper I)—and, more recently, 2003 VB_{12} (90377 Sedna; Brown et al. 2004)—whose large eccentricities and distant perihelia are difficult to understand if we appeal only to the planets in their present configuration (Gladman et al. 2002). The dividing line we draw in eccentricity is arbitrary. A simple,

TABLE 5
RESONANCES TESTED FOR MEMBERSHIP

Name	p	q	m	n	r	Name	p	q	m	n	r	Name	p	q	m	n	r
1:1	1	1	0	0	0	5:3 s^2	5	3	0	2	0	7:4 es^2	7	4	1	2	0
1:1 e^2s^2	1	1	−2	2	0	5:3 ee_N	5	3	1	0	1	7:4 e^2e_N	7	4	2	0	1
1:1 ee_N	1	1	−1	0	1	5:3 e^3e_N	5	3	3	0	−1	8:5 e^3	8	5	3	0	0
2:1 e	2	1	1	0	0	6:4 s^2	6	4	0	2	0	8:5 es^2	8	5	1	2	0
2:1 es^2	2	1	−1	2	0	6:4 ee_N	6	4	1	0	1	8:5 e^2e_N	8	5	2	0	1
2:1 e_N	2	1	0	0	1	6:4 e^3e_N	6	4	3	0	−1	9:6 es^2	9	6	1	2	0
2:1 e^2e_N	2	1	2	0	−1	7:5 e^2	7	5	2	0	0	9:6 e^2e_N	9	6	2	0	1
2:1 e_Ns^2	2	1	0	2	−1	7:5 s^2	7	5	0	2	0	10:7 e^3	10	7	3	0	0
3:2 e	3	2	1	0	0	7:5 ee_N	7	5	1	0	1	10:7 es^2	10	7	1	2	0
3:2 es^2	3	2	−1	2	0	7:5 e^3e_N	7	5	3	0	−1	10:7 e^2e_N	10	7	2	0	1
3:2 e_N	3	2	0	0	1	8:6 s^2	8	6	0	2	0	11:8 e^3	11	8	3	0	0
3:2 e^2e_N	3	2	2	0	−1	8:6 ee_N	8	6	1	0	1	11:8 es^2	11	8	1	2	0
3:2 e_Ns^2	3	2	0	2	−1	8:6 e^3e_N	8	6	3	0	−1	11:8 e^2e_N	11	8	2	0	1
4:3 e	4	3	1	0	0	9:7 e^2	9	7	2	0	0	12:9 es^2	12	9	1	2	0
4:3 es^2	4	3	−1	2	0	9:7 s^2	9	7	0	2	0	12:9 e^2e_N	12	9	2	0	1
4:3 e_N	4	3	0	0	1	9:7 ee_N	9	7	1	0	1	13:10 e^3	13	10	3	0	0
4:3 e^2e_N	4	3	2	0	−1	9:7 e^3e_N	9	7	3	0	−1	13:10 es^2	13	10	1	2	0
4:3 e_Ns^2	4	3	0	2	−1	10:8 s^2	10	8	0	2	0	13:10 e^2e_N	13	10	2	0	1
5:4 e	5	4	1	0	0	10:8 ee_N	10	8	1	0	1	14:11 e^3	14	11	3	0	0
5:4 es^2	5	4	−1	2	0	10:8 e^3e_N	10	8	3	0	−1	14:11 es^2	14	11	1	2	0
5:4 e_N	5	4	0	0	1	11:9 e^2	11	9	2	0	0	14:11 e^2e_N	14	11	2	0	1
5:4 e^2e_N	5	4	2	0	−1	11:9 s^2	11	9	0	2	0	15:12 es^2	15	12	1	2	0
5:4 e_Ns^2	5	4	0	2	−1	11:9 ee_N	11	9	1	0	1	15:12 e^2e_N	15	12	2	0	1
6:5 e	6	5	1	0	0	11:9 e^3e_N	11	9	3	0	−1	5:1 e^4	5	1	4	0	0
6:5 es^2	6	5	−1	2	0	12:10 s^2	12	10	0	2	0	5:1 e^2s^2	5	1	2	2	0
6:5 e_N	6	5	0	0	1	12:10 ee_N	12	10	1	0	1	5:1 s^4	5	1	0	4	0
6:5 e^2e_N	6	5	2	0	−1	12:10 e^3e_N	12	10	3	0	−1	5:1 e^3e_N	5	1	3	0	1
6:5 e_Ns^2	6	5	0	2	−1	4:1 e^3	4	1	3	0	0	7:3 e^4	7	3	4	0	0
3:1 e^2	3	1	2	0	0	4:1 ees^2	4	1	1	2	0	7:3 e^2s^2	7	3	2	2	0
3:1 s^2	3	1	0	2	0	4:1 e^2e_N	4	1	2	0	1	7:3 s^4	7	3	0	4	0
3:1 ee_N	3	1	1	0	1	5:2 e^3	5	2	3	0	0	7:3 e^3e_N	7	3	3	0	1
3:1 e^3e_N	3	1	3	0	−1	5:2 es^2	5	2	1	2	0	9:5 e^4	9	5	4	0	0
4:2 s^2	4	2	0	2	0	5:2 e^2e_N	5	2	2	0	1	9:5 e^2s^2	9	5	2	2	0
4:2 ee_N	4	2	1	0	1	6:3 es^2	6	3	1	2	0	9:5 s^4	9	5	0	4	0
4:2 e^3e_N	4	2	3	0	−1	6:3 e^2e_N	6	3	2	0	1	9:5 e^3e_N	9	5	3	0	1
5:3 e^2	5	3	2	0	0	7:4 e^3	7	4	3	0	0						

physically meaningful test would be preferred but remains elusive. Our current choice serves to cull out the more obvious objects in this category but leaves the nature of objects near the dividing line for future study. Orbital inclination may be useful as well in identifying Scattered-Extended objects.

3.2.4. *Classical*

"Classical" KBOs have mean Tisserand parameters greater than 3 and time-averaged eccentricities less than 0.2. Their relatively cold orbits are assumed not to have been significantly altered by Neptune in its current orbit. The comments above regarding the arbitrariness of our defining line in eccentricity apply for Classical objects as well.

3.3. *Implementation*

Orbit classification is rendered uncertain by errors in the initial positions and velocities of KBOs, that is, uncertainties in the elements of the osculating ellipses fitted to astrometric observations. As in Paper I, we employ methods devised by Bernstein & Khushalani (2000) to estimate these uncertainties. An exhaustive survey of all possible orbits in six-dimensional phase space for each KBO would be too expensive computationally. We proceed instead with a more restrictive algorithm that focuses on the most physically meaningful question of resonance membership. In the six-dimensional space of possible orbits for each object, we select three orbits to classify. The first ("solution 1") is the nominal best-fit orbit. The second orbit ("solution 2") lies on the 3 σ confidence surface in six-dimensional phase space and has a semimajor axis that is maximally greater than the nominal best-fit semimajor axis. The third orbit ("solution 3") also lies on the 3 σ confidence surface, but it is characterized by a semimajor axis that is maximally less than the nominal best-fit value. We favor exploring the widest excursion in semimajor axis because that is the parameter that most influences resonance membership. Another important parameter is eccentricity; however, as will be seen shortly, the uncertainty in eccentricity is often strongly correlated with the uncertainty in the semimajor axis. Thus, probing the greatest variation in the semimajor axis typically implies exploring the greatest variation in eccentricity.

We identify orbital solutions 2 and 3 as follows: For each object, we solve numerically for the eigenvectors, $\boldsymbol{e}_{i'}$, and eigenvalues, $\lambda_{i'}$, of the 6×6 covariance matrix, $\sigma_{\boldsymbol{jk}}$. The covariance matrix is calculated using the formalism of Bernstein & Khushalani (2000); here $\boldsymbol{j}$ and $\boldsymbol{k}$ refer to any one of the six Cartesian phase-space coordinates, $\{x, y, z, \dot{x}, \dot{y}, \dot{z}\}$. A random linear combination of these eigenvectors, $\sum_{i'=1}^{6} c_{i'}\lambda_{i'}^{1/2}\boldsymbol{e}_{i'}$, is created such that $\sum_{i'=1}^{6} c_{i'}^2 = N^2$. By construction, this vector lies on the $N\,\sigma$ confidence surface. In our present implementation, we fix $N = 3$. We generate a random sampling of 1000

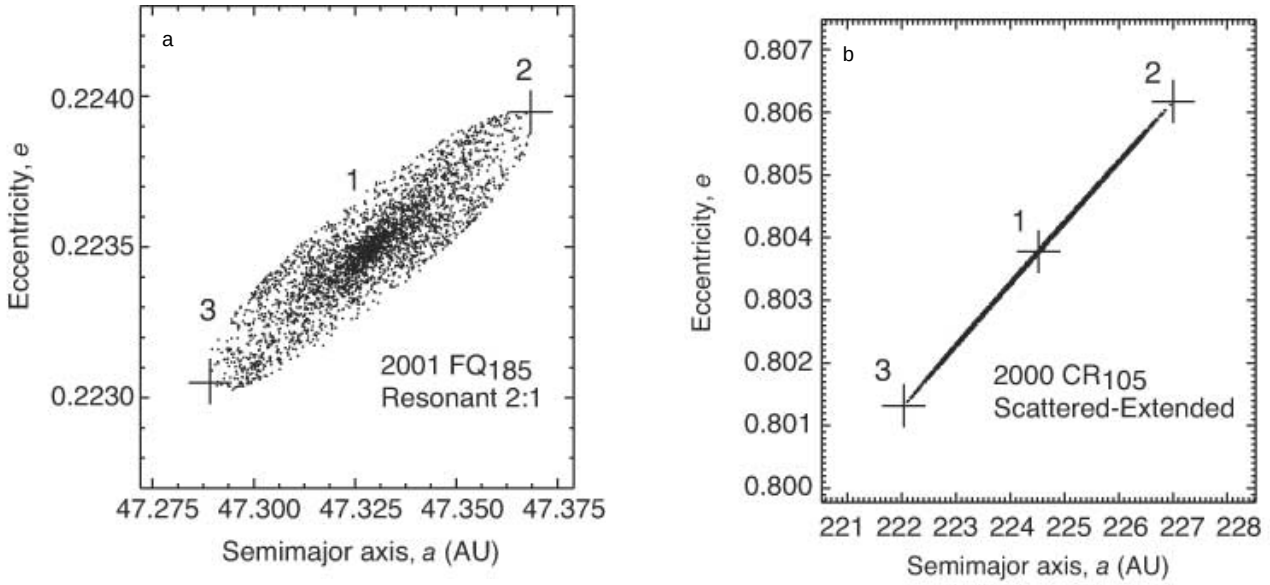

FIG. 3.—Sample projections onto the *a*-*e* plane of the 3 σ confidence surface in the six-dimensional phase space of possible osculating orbits for KBOs (*a*) 2001 FQ_{185} and (*b*) 2000 CR_{105}. Plus signs denote orbital solutions (orbital solution 1 is located at the center of each panel). Orbit classifications based on numerical integrations of these three solutions are compared to judge whether the identification of an object as Resonant or otherwise is secure. The KBOs featured in this figure have secure identifications.

such vectors, add each vector to the nominal best-fit orbital solution, and transform the Cartesian elements of each resultant orbit to Keplerian elements. The two orbits having semimajor axes that differ most from the nominal best-fit semimajor axis in positive and negative senses are selected for integration and classification.

Figure 3 displays, for two sample objects, the 3 σ confidence surface projected onto the *a*-*e* plane. The parameters *a* and *e* are positively correlated, reflecting the relatively certain value of the object's instantaneous heliocentric distance. Orbital solutions 2 and 3 are indicated in each panel; orbital solution 1 lies at the center of each panel. Of course, values for the four other orbital elements also differ from solution to solution, since all the elements are correlated to varying degrees.

We numerically integrate our triad of initial conditions for each KBO designated by the MPC, using the astrometric database maintained at Lowell Observatory. We employ the regularized, mixed-variable symplectic integrator RMVS3, developed by Levison & Duncan (1994) and based on the *N*-body map of Wisdom & Holman (1991). We include the influence of the four giant planets, treat each KBO as a massless test particle, and integrate trajectories forward for 10 Myr using a time step of 50 days, starting at Julian Date 2,451,545.0 (2000 January 1, 1200 UT). Any duration of integration longer than the resonant libration period, $\sim$0.01 Myr, would be adequate to test for membership in MMRs. However, we have found by numerical experiment that adopting durations less than $\sim$1 Myr yields membership in a host—often more than five—of weak MMRs for a given object. Upon integrating for longer durations, many objects escape most of these high-order resonances. Since we are interested in long-term, presumably primordial residents of resonances, we integrate for as long as is computationally practical, that is, 10 Myr. In cases of particular interest—for example, 2001 QR_{322}, the Neptunian Trojan (Chiang et al. 2003a)—we integrate trajectories up to 1000 Myr to test for long-term stability. Note that 10 Myr is sufficient to also test for membership in the Kozai secular resonance, in which the argument of perihelion librates. Figure 4 shows a sampling of the evolution of the resonant argument for four Resonant KBOs.

Initial positions and velocities for all objects, including planets, are computed at Lowell Observatory. The relative energy error over the integration is bounded to less than 10^{-7}. The software presently takes 12 hours to classify 100 objects on a single Pentium III 933 MHz processor.

An object is considered to have a "secure" orbit classification if all three sets of initial conditions yield the same classification and if the difference between semimajor axes in orbital solutions 2 and 3 is less than 10% of the nominal best-fit semimajor axis. We refer henceforth to the fractional difference in semimajor axes as the "3 σ fractional uncertainty." Objects for which the nominal position does not yield a classification are considered to be "unclassified"; the errors in their orbital elements are simply too large.

To test the robustness of our classification scheme, we have further examined the behavior of four objects that our scheme classifies as "Resonant 2:1 *e*" (2000 QL_{251}), "Classical" (2001 FO_{185}), "Scattered-Extended" (2000 CR_{105}), and "Resonant 7:4 e^3" (2001 KP_{77}). For each object, we integrated 100 orbital solutions distributed randomly over the 3 σ confidence surface in six-dimensional phase space for 10 Myr. For 2000 QL_{251}, 98 out of 100 orbital solutions yielded the same classification of Resonant 2:1 *e*; one solution yielded Resonant 2:1 $e + 4{:}2\ i^2$, and one solution was classified as Classical. For 2001 FO_{185}, 98 of 100 solutions yielded the same classification of Classical; one solution yielded 2:1 *e* and one solution yielded 4:2 i^2. For 2000 CR_{105}, all 100 solutions were classified as Scattered-Extended. Finally, for 2001 KP_{77} all 100 solutions were classified as Resonant 7:4 e^3. These explorations, while not exhaustive, support the robustness of our method.

3.4. *Classification of DES Objects*

For the purposes of this paper, we have placed all designated DES objects of a given dynamical class into a separate table: Resonant, Centaur, Scattered (Near and Extended), Classical, and unclassified. We emphasize that the order in which these

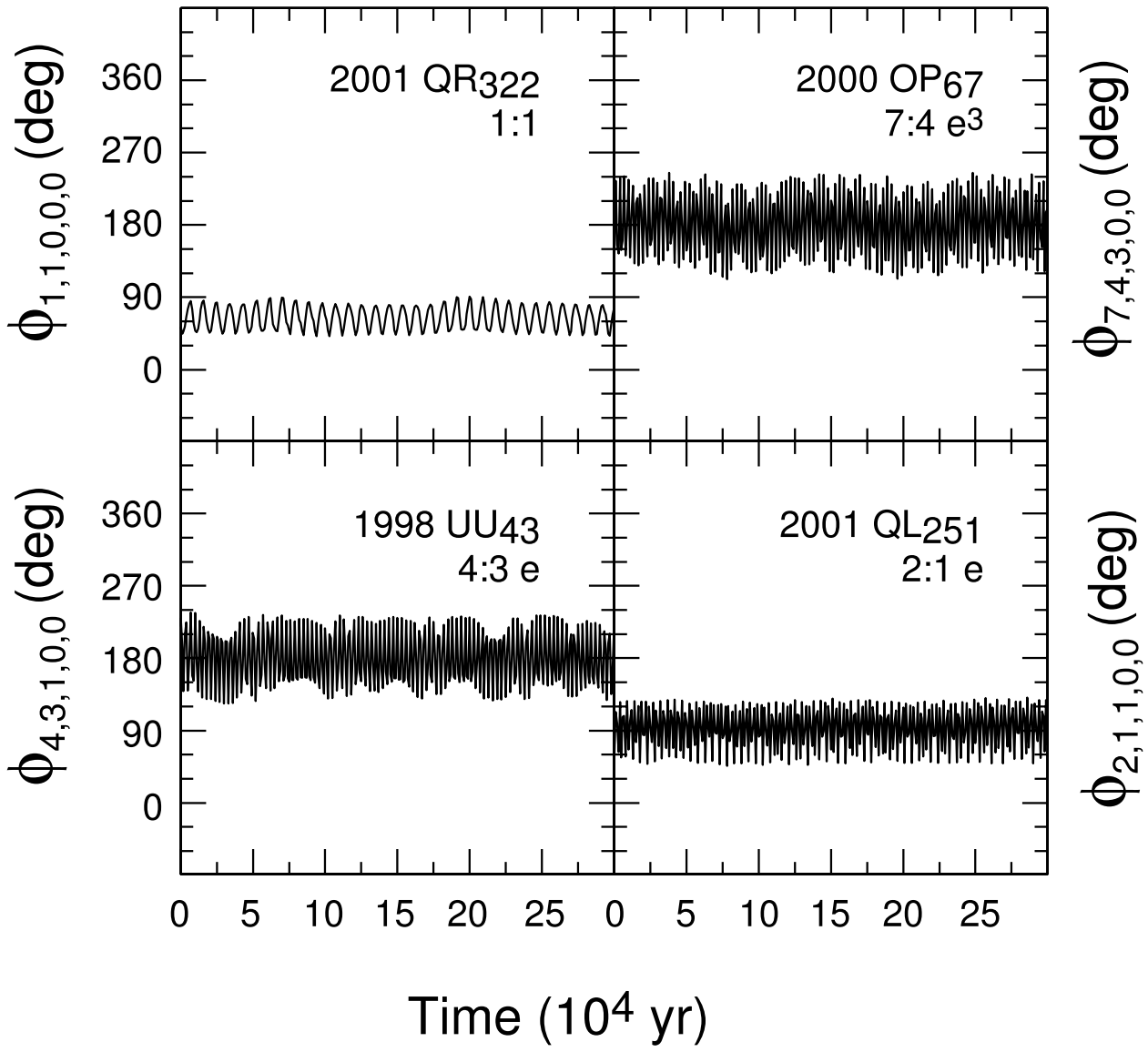

FIG. 4.—Evolutions of the resonant argument, $\phi_{p,q,m,n,r}$, vs. time, for four securely classified Resonant KBOs given their nominal best-fit initial conditions.

classes are tested for membership is significant. For example, Resonant KBOs are often planet-crossers but should not be labeled as Centaurs, because the former, unlike the latter, are phase-protected from close encounters with Neptune. The Resonant objects appear in Table 6 (sorted according to increasing semimajor axis). We find objects inhabiting 10 first-order resonances, ranging from zeroth order (1:1) to fourth order (9:5). Next, the Centaurs are listed in Table 7 (sorted by increasing perihelion distance). Following that, we present the Scattered-Near and Scattered-Extended objects in Table 8 (sorted according to increasing values of their mean Tisserand parameter) and the Classical objects in Table 9 (sorted according to increasing inclination relative to the calculated plane of the Kuiper belt, as described in § 5). Typically the instantaneous Tisserand parameter is observed to vary by no more than 0.02 over the duration of our integrations. The boundary between Scattered-Near objects and Classical/Scattered-Extended objects is blurred to this degree. We note that for our analyses we include 19 objects whose nominal position gives a classification but for which solutions 2 and 3 are not in agreement. We consider the nominal classification in this case "provisional" and note the affected objects in Tables 6–9.

Finally, Table 10 gives the unclassified objects (sorted according to decreasing "arc length," which is the time between the first and last reported observations of an object). Unclassified objects with the longest arc lengths may need just one additional observation to allow dynamical classification, while unclassified objects with the shortest arcs—especially those discovered prior to 2003—are "lost," which we define as having a positional error greater than 1000″ (half a Mosaic field). Ultimately, however, when wider field and deeper surveys come on line (e.g., Pan-STARRS [Jewitt 2003] and the Discovery Channel Telescope [Sebring et al. 2004]), most (if not all) of these objects will be rediscovered and linked to their first-epoch observations in the MPC database. Current positional errors for all KBOs and Centaurs given provisional designations by the MPC are computed daily and are available online (see Appendix A).

The number of objects classified into each dynamical category, uncorrected for observational and other biases, are summarized

TABLE 6

LOG OF DISCOVERIES: RESONANT OBJECTS (SORTED BY INCREASING SEMIMAJOR AXIS, a)

Designation	Resonance	a (AU)	e	i (deg)	UT Discovery Date	R.A. (J2000)	Decl. (J2000)	Frame Mag.	R (AU)	Desig. Telescope[a]	MPEC No.[b]
2001 QR_{322}	1:1	30.1	0.03	1.3	2001 Aug 21.31880	23 53 35.0	−01 19 57	21.2	29.6	5	2001-V11
2002 GW_{32}	5:4 e	35.1	0.07	6.4	2002 Apr 9.23285	14 41 48.4	−21 09 57	21.6	37.6	2	2002-K13
2003 FC_{128}	5:4 e	35.2	0.10	2.4	2003 Apr 1.18109	10 55 33.9	+09 28 54	21.8	32.6	3, 5	2003-H07
1998 UU_{43}	4:3 e	36.5	0.13	9.6	1998 Oct 22.35003	02 17 47.6	+16 18 22	22.5	37.8	4	1999-B23
1998 WV_{31}	3:2 e	39.2	0.27	5.7	1998 Nov 19.09014	02 29 45.2	+12 45 25	22.3	32.9	6	1999-A18
2001 KN_{77}[c]	3:2 e	39.2	0.24	2.4	2001 May 23.14650	15 25 30.9	−19 05 32	22.5	37.1	1	2002-B13
2001 QF_{298}	3:2 e	39.2	0.11	22.4	2001 Aug 19.23189	23 16 02.5	−06 01 39	20.0	42.5	7	2001-T54
2001 QG_{298}	3:2 e	39.2	0.19	6.5	2001 Aug 19.27979	23 33 00.4	−04 02 31	19.8	32.1	7	2001-T54
2001 QH_{298}	3:2 e	39.2	0.11	6.7	2001 Aug 19.31029	23 41 47.5	−07 04 52	22.2	36.5	2	2001-T54
2001 RX_{143}	3:2 e	39.2	0.30	19.3	2001 Sep 12.36378	00 56 04.3	+03 18 01	22.1	40.5	5	2001-V12
69990	3:2 e	39.3	0.19	6.6	1998 Nov 18.14056	03 07 05.7	+18 27 14	23.0	32.6	6	1999-A17
1998 US_{43}	3:2 e	39.3	0.13	10.6	1998 Oct 22.40628	03 08 48.4	+16 39 15	22.8	35.2	5	1998-X06
2001 KY_{76}	3:2 e	39.3	0.23	4.0	2001 May 22.25638	16 40 58.5	−20 52 24	21.6	39.0	1	2001-N01
2001 RU_{143}	3:2 e	39.3	0.15	6.5	2001 Sep 12.32603	00 41 52.6	+06 41 05	22.0	43.8	7	2001-V11
2002 VU_{130}[c]	3:2 e	39.3	0.22	1.4	2002 Nov 7.33949	03 53 56.7	+20 56 44	21.5	43.0	7	2002-X10
1998 WS_{31}	3:2 e	39.4	0.20	6.8	1998 Nov 18.09812	02 17 37.8	+16 33 43	22.5	31.5	6	1999-A15
2001 FR_{185}	3:2 e	39.4	0.19	5.6	2001 Mar 26.37387	13 13 47.7	−14 03 24	24.5	34.7	5	2001-M36
2002 CW_{224}	3:2 e	39.4	0.25	5.7	2001 Oct 21.30293	03 27 18.5	+23 36 03	22.3	39.0	5	2002-D39
2002 GF_{32}	3:2 e	39.4	0.18	2.8	2002 Apr 8.13603	14 38 13.4	−15 16 57	21.1	42.2	2	2002-K12
28978	3:2 e	39.5	0.24	19.6	2001 May 22.22320	16 16 06.1	−19 13 45	19.0	46.6	1, 7	2001-N01
69986	3:2 e	39.5	0.22	13.9	1998 Nov 18.14056	03 05 15.2	+18 38 37	22.3	31.3	11	1998-X13
1998 UR_{43}	3:2 e	39.5	0.22	8.8	1998 Oct 22.35531	02 20 42.9	+11 07 23	22.6	31.9	5	1998-X05
2001 KQ_{77}	3:2 e	39.5	0.16	15.6	2001 May 23.18666	15 55 51.9	−22 24 55	21.5	36.8	1	2002-B13
2001 UO_{18}	3:2 e	39.5	0.29	3.7	2001 Oct 19.38539	01 09 58.4	+06 10 53	22.3	32.5	5	2001-V13
2002 VX_{130}	3:2 e	39.5	0.22	1.3	2002 Nov 7.19001	01 54 56.6	+13 13 25	22.3	30.8	10	2002-X25
1998 WZ_{31}	3:2 e	39.6	0.17	14.6	1998 Nov 19.41122	03 35 42.1	+20 59 22	22.7	33.0	11	1999-B27
2000 CK_{105}	3:2 e	39.6	0.23	8.1	2000 Feb 6.27972	08 58 53.0	+19 20 30	22.7	48.5	1	2000-F02
2001 KD_{77}	3:2 e	39.6	0.12	2.3	2001 May 24.20319	16 32 01.9	−19 41 51	20.5	35.3	1, 7	2001-N03
2002 GW_{31}	3:2 e	39.6	0.24	2.6	2002 Apr 6.07682	11 30 37.9	+00 47 52	22.0	40.1	2, 10	2002-K12
2002 GY_{32}	3:2 e	39.6	0.09	1.8	2002 Apr 6.19153	14 09 13.3	−13 25 58	21.4	36.0	10	2002-K15
2001 KB_{77}	3:2 e	39.7	0.29	17.5	2001 May 23.02021	14 18 10.9	−15 28 04	21.9	31.6	1	2001-N03
2002 CE_{251}	3:2 e	39.7	0.27	9.3	2002 Feb 8.35489	10 58 20.2	+06 34 45	22.7	30.0	5	2002-G19
2002 GL_{32}	3:2 e	39.7	0.13	7.1	2002 Apr 6.17214	13 12 18.8	−08 52 47	22.5	34.5	10	2002-K13
2003 FF_{128}	3:2 e	39.8	0.22	1.9	2003 Apr 1.40718	14 05 27.0	−10 54 57	21.5	33.1	3, 5	2003-H07
2000 QN_{251}	5:3 e^2	42.0	0.12	0.3	2000 Aug 26.31447	23 43 27.1	−02 04 33	22.3	37.0	2	2001-M36
2000 OP_{67}	7:4 e^3	43.5	0.19	0.8	2000 Jul 31.28569	21 43 20.4	−13 09 54	22.9	38.8	2	2000-T42
2001 QE_{298}	7:4 e^3	43.5	0.15	3.7	2001 Aug 19.23189	23 15 34.6	−06 14 01	21.2	37.7	2	2001-T54
2001 KP_{76}[c]	7:4 e^3	43.6	0.19	7.2	2001 May 23.19031	15 57 09.6	−22 55 14	21.9	44.1	1	2001-M60
2001 KJ_{76}[c]	7:4 e^3	43.7	0.08	6.7	2001 May 23.18666	15 56 00.4	−22 04 42	22.2	42.7	1	2001-M59
1999 HG_{12}	7:4 e^3	43.8	0.15	1.0	1999 Apr 18.20550	13 29 03.8	−09 12 07	23.9	43.1	6	1999-N11
2001 KO_{76}	7:4 e^3	43.8	0.11	2.1	2001 May 23.04265	14 30 04.3	−14 38 02	23.0	46.2	1	2001-M60
2001 KP_{77}	7:4 e^3	43.8	0.18	3.3	2001 May 23.16475	15 46 16.8	−22 00 48	21.7	36.0	1	2002-B13
2001 KL_{76}	9:5 e^4	44.5	0.10	1.3	2001 May 22.20493	16 02 11.5	−20 59 17	23.0	48.4	1	2001-M60
2002 GD_{32}[c]	9:5 e^4	44.7	0.14	6.6	2002 Apr 7.17181	13 48 40.5	−12 05 32	21.4	50.2	2, 10	2002-K12
2000 QL_{251}	2:1 e	47.6	0.22	3.7	2000 Aug 25.22045	23 19 31.6	−01 03 41	22.2	38.2	5	2001-M34
2001 UP_{18}	2:1 e	47.6	0.08	1.2	2001 Oct 19.38539	01 10 14.2	+06 09 45	22.3	50.2	5	2001-V13
2002 VD_{130}	2:1 e	47.9	0.33	3.9	2002 Nov 7.34702	03 59 04.4	+22 11 41	22.0	33.4	5	2002-W30
2001 FQ_{185}	2:1 e	48.0	0.23	3.2	2001 Mar 26.36019	12 35 42.4	−00 56 41	23.2	37.0	7	2001-M36
2003 FE_{128}	2:1 e	48.3	0.26	3.4	2003 Apr 1.41931	13 58 13.9	−09 38 03	21.5	36.0	3, 5	2003-H07
2002 GX_{32}	7:3 e^4	53.1	0.37	13.9	2002 Apr 9.24395	14 48 38.0	−20 41 18	21.3	33.3	2	2002-K13
69988	5:2 e^3	55.1	0.43	9.5	1998 Nov 18.08751	02 14 16.2	+16 26 30	22.8	38.6	5	1998-X38
2001 KC_{77}	5:2 e^3	55.3	0.36	12.9	2001 May 23.17570	15 46 14.0	−20 09 22	21.5	35.4	1	2001-N03
2002 GP_{32}	5:2 e^3	55.7	0.43	1.6	2002 Apr 6.26486	14 53 40.7	−14 56 52	20.3	32.2	10	2002-K13
38084	5:2 e^3	56.1	0.42	13.1	1999 Apr 18.16414	12 40 36.8	+01 25 25	21.9	35.4	6	1999-K15

NOTE.—Units of right ascension are hours, minutes, and seconds, and units of declination are degrees, arcminutes, and arcseconds.

[a] Telescope(s) on which the frames used for object designation were taken: (1) Baade; (2) Blanco; (3) Clay; (4) INT; (5) Mayall; (6) NOT; (7) Perkins; (8) Shane; (9) Steward; (10) UH 2.2 m; (11) WIYN.

[b] Minor Planet Electronic Circular in which the object was designated.

[c] Classification based on nominal position and either the minus or plus 3 σ position.

TABLE 7

LOG OF DISCOVERIES: CENTAURS (SORTED BY INCREASING PERIHELION DISTANCE, R)

Designation	a (AU)	e	i (deg)	q (AU)	UT Discovery Date	R.A. (J2000)	Decl. (J2000)	Frame Mag.	R (AU)	Desig. Telescope[a]	MPEC No.[b]
54598	16.5	0.20	20.8	13.1	2000 Aug 27.13756	22 24 10.7	−11 50 11	19.5	16.5	7	2000-T42
2002 VR_{130}	23.9	0.38	3.5	14.7	2002 Nov 7.14797	01 12 45.0	+06 23 27	22.0	15.0	7	2002-X10
2000 QB_{243}	34.7	0.56	6.8	15.2	2000 Aug 25.03876	20 50 02.7	−20 13 22	20.4	18.1	2, 7	2000-T42
2001 KF_{77}	26.0	0.24	4.4	19.8	2001 May 23.98413	13 59 57.0	−13 49 58	23.2	22.4	5	2001-N04
2000 CO_{104}	24.3	0.15	3.1	20.6	2000 Feb 6.32413	09 58 09.3	+13 57 00	22.8	20.7	11	2000-E64
2002 PQ_{152}	25.6	0.20	9.4	20.6	2002 Aug 12.29280	22 37 21.3	−06 20 41	20.8	21.1	8, 7	2002-T24
2000 OO_{67}	514.3	0.96	20.1	20.8	2000 Jul 29.28459	22 16 07.3	−13 48 00	22.1	21.7	2	2000-T42
2002 XU_{93}	67.4	0.69	77.9	21.0	2002 Dec 4.37006	06 05 47.7	+24 08 04	20.8	22.0	7	2003-A15
2003 FH_{129}[c]	69.8	0.60	18.7	28.0	2003 Mar 30.24469	11 11 34.2	+03 50 24	23.0	34.0	10	2003-K17
2000 CQ_{104}[d]	36.9	0.24	13.5	28.2	2000 Feb 6.34631	10 10 34.0	+14 36 19	23.0	35.6	11	2000-E64
2003 FB_{128}	39.3	0.24	8.9	29.8	2003 Mar 30.38998	13 50 58.5	−11 27 24	21.4	32.2	3, 5	2003-H07
2003 FL_{127}[d]	39.2	0.21	3.5	30.8	2003 Apr 1.20889	10 57 26.1	+04 43 57	22.8	47.1	3, 5	2003-H05
2003 QW_{90}[c]	46.6	0.28	10.3	33.5	2003 Aug 25.29373	00 04 08.6	−03 17 27	19.9	44.2	2	2003-Q58

[a] Telescope(s) on which the frames used for object designation were taken: (1) Baade; (2) Blanco; (3) Clay; (4) INT; (5) Mayall; (6) NOT; (7) Perkins; (8) Shane; (9) Steward; (10) UH 2.2 m; (11) WIYN.
[b] Minor Planet Electronic Circular in which the object was designated.
[c] Classification based on nominal position.
[d] Classification based on nominal position and either the minus or plus 3 σ position.

TABLE 8

LOG OF DISCOVERIES: SCATTERED OBJECTS (SORTED BY INCREASING TISSERAND PARAMETER, T)

Designation	a (AU)	e	i (deg)	T	q (AU)	UT Discovery Date	R.A. (J2000)	Decl. (J2000)	Frame Mag.	R (AU)	Desig. Telescope[a]	MPEC No.[b]
Scattered-Near												
2001 FP_{185}	226.9	0.85	30.8	2.64	34.3	2001 Mar 26.19463	11 57 50.7	+00 21 42	22.2	34.4	7, 5	2001-M36
2002 PP_{149}	40.8	0.09	34.8	2.67	37.2	2002 Aug 12.30468	22 40 55.2	−07 24 54	22.3	38.4	2	2003-S21
2001 QC_{298}	46.1	0.12	30.6	2.75	40.6	2001 Aug 21.17631	22 33 59.6	−07 30 05	21.0	40.6	5	2001-T40
2002 GH_{32}	42.9	0.15	26.7	2.79	36.3	2002 Apr 9.21801	14 08 10.1	−16 02 38	20.7	42.6	2	2002-K12
1998 WT_{31}	46.0	0.18	28.7	2.80	37.5	1998 Nov 18.11955	02 43 38.7	+17 19 52	22.6	38.9	6	1999-A16
2000 CG_{105}	46.6	0.04	27.9	2.81	44.8	2000 Feb 5.17626	09 04 46.0	+16 54 11	22.6	46.4	11	2000-F02
2003 FJ_{127}	44.7	0.24	22.8	2.86	33.9	2003 Mar 30.24086	11 11 45.6	+07 13 35	23.3	41.2	3, 5	2003-H05
60458	60.2	0.41	19.7	2.90	35.6	2000 Feb 5.17189	08 58 49.9	+17 07 41	22.8	44.1	11	2000-J45
2001 FN_{185}	42.7	0.08	21.7	2.90	39.4	2001 Mar 26.36931	13 06 33.2	−09 11 23	24.4	39.5	5	2001-M34
2001 KO_{77}	44.0	0.15	20.7	2.90	37.3	2001 May 23.16475	15 45 33.6	−22 22 17	22.5	37.9	1	2002-B13
2001 QA_{298}	46.0	0.19	23.7	2.91	37.5	2000 Jul 29.20794	20 50 14.1	−23 02 00	22.2	38.6	2	2001-T40
38083	39.2	0.16	12.7	2.93	33.1	1999 Apr 17.13881	12 09 31.6	+00 51 49	22.4	38.3	6	1999-K15
2000 CQ_{105}	57.5	0.39	19.6	2.93	34.8	2000 Feb 5.18506	09 15 15.4	+17 53 09	21.9	50.9	9	2000-F07
2000 OM_{67}	97.3	0.60	23.4	2.93	39.2	2000 Jul 31.32091	22 28 26.0	−05 17 56	22.1	40.2	2	2000-T41
2000 QM_{251}	44.5	0.26	15.7	2.93	32.8	2000 Aug 25.30929	23 44 15.8	−01 54 15	22.2	35.0	2	2001-M36
2001 KG_{77}	61.8	0.45	15.5	2.94	34.0	2001 May 23.19031	15 56 59.8	−22 55 50	23.0	34.9	1	2001-N04
2002 VF_{130}[c]	46.1	0.13	19.5	2.94	40.0	2002 Nov 7.35859	04 14 15.2	+25 30 53	23.2	42.4	5	2002-W30
2000 CO_{105}	47.3	0.14	19.2	2.95	40.5	2000 Feb 5.13617	08 10 26.2	+22 38 16	22.4	49.3	11	2000-F07
2002 CY_{224}	54.4	0.35	15.7	2.96	35.3	2002 Feb 8.17569	08 53 59.5	+19 20 19	21.0	35.9	5	2002-D39
2002 GA_{32}	52.1	0.33	15.1	2.96	35.1	2002 Apr 7.28495	16 10 49.9	−21 21 20	22.1	41.8	2	2002-K12
2001 KV_{76}	70.1	0.51	15.3	2.97	34.3	2001 May 24.05018	14 20 52.6	−13 34 38	23.3	39.2	1	2002-K05
1999 HC_{12}	45.6	0.24	15.3	2.98	34.6	1999 Apr 18.34230	14 35 56.4	−10 10 06	22.4	39.2	6	1999-K15
2001 FT_{185}	47.4	0.11	19.5	2.99	42.3	2001 Mar 26.38324	13 12 10.8	−08 45 34	24.5	43.1	2, 1	2001-N01
2002 GB_{32}	216.1	0.84	14.2	2.99	35.4	2002 Apr 7.06373	12 28 25.9	−00 17 28	21.9	37.2	2, 10	2002-K12
Scattered-Extended												
1999 HW_{11}	53.0	0.26	17.2	3.01	39.2	1999 Apr 18.21595	13 35 38.8	−07 43 05	23.3	41.4	6	1999-K12
2002 GG_{32}[d]	55.2	0.35	14.7	3.02	36.1	2002 Apr 9.25531	14 54 55.7	−19 37 44	22.0	38.2	2	2002-K12
2001 QW_{297}	51.4	0.23	17.1	3.03	39.5	2000 Aug 26.07557	21 49 50.1	−14 25 35	22.1	46.1	2	2001-T39
2002 CX_{154}	72.2	0.47	15.9	3.03	38.0	2002 Feb 6.39463	11 00 09.4	+07 46 12	22.1	38.4	5	2002-D25
2001 KG_{76}	51.8	0.34	1.5	3.04	33.9	2001 May 22.20858	16 06 45.7	−20 01 22	22.0	43.9	1	2001-M59
42301	51.4	0.28	0.8	3.09	36.9	2001 Oct 21.19313	01 14 11.9	+08 39 55	20.5	43.8	7	2001-V57
2003 UY_{291}[c]	49.5	0.24	3.6	3.09	37.4	2003 Oct 24.39668	03 36 56.2	+22 33 04	22.8	42.9	5	2003-Y79
2002 GZ_{31}	50.5	0.24	1.1	3.11	38.5	2002 Apr 6.25380	14 42 55.2	−14 42 16	21.6	42.3	2, 10	2002-K12
2000 CR_{105}	228.2	0.81	22.7	3.17	44.3	2000 Feb 6.30637	09 14 02.4	+19 05 58	22.5	52.7	11	2000-F07

[a] Telescope(s) on which the frames used for object designation were taken: (1) Baade; (2) Blanco; (3) Clay; (4) INT; (5) Mayall; (6) NOT; (7) Perkins; (8) Shane; (9) Steward; (10) UH 2.2 m; (11) WIYN.
[b] Minor Planet Electronic Circular in which the object was designated.
[c] Classification based on nominal position.
[d] Classification based on nominal position and either the minus or plus 3 σ position.

TABLE 9

LOG OF DISCOVERIES: CLASSICAL OBJECTS (SORTED BY INCREASING KBP INCLINATION, i_K)

Designation	a (AU)	e	i (deg)	i_K (deg)	UT Discovery Date	R.A. (J2000)	Decl. (J2000)	Frame Mag.	R (AU)	Desig. Telescope[a]	MPEC No.[b]
2001 QY_{297}	43.6	0.07	1.5	0.2	2001 Aug 21.11215	20 40 21.1	−18 53 26	20.3	42.5	7	2001-T39
2001 QP_{297}	45.0	0.12	1.4	0.3	2001 Aug 19.27979	23 34 05.7	−04 10 39	21.9	43.3	2	2001-T38
2000 OJ_{67}	42.6	0.02	1.1	0.4	2000 Jul 29.24841	21 33 57.4	−15 17 48	21.6	42.6	2	2000-T41
2002 CS_{154}	43.5	0.05	1.2	0.4	2002 Feb 6.36691	10 50 43.1	+08 36 03	22.5	42.3	5	2002-D24
1998 WY_{24}	43.3	0.04	1.9	0.5	1998 Nov 18.43762	04 59 35.4	+21 49 05	22.6	41.9	11	1998-X15
2000 CN_{114}	44.2	0.04	1.6	0.5	2000 Feb 5.33597	09 23 24.6	+16 40 57	22.2	44.1	11	2000-J45
2001 KK_{76}	42.5	0.01	1.9	0.6	2001 May 24.17760	16 25 08.8	−21 00 30	21.9	42.2	1	2001-M59
2002 CY_{154}	44.6	0.07	1.0	0.6	2002 Feb 6.40649	11 07 54.1	+06 19 54	22.6	47.6	5	2002-D25
2002 VD_{131}	44.9	0.05	0.9	0.7	2002 Nov 7.16463	01 15 54.1	+07 10 50	22.3	43.3	10	2002-X26
1998 WG_{24}	45.8	0.13	2.2	0.8	1998 Nov 18.43220	05 00 31.5	+22 14 15	22.1	41.3	5	1998-X07
2001 DD_{106}[c, d]	44.4	0.10	1.8	0.8	2003 Apr 1.25000	10 59 50.7	+07 43 27	23.0	40.5	5	2003-N17
69987	42.5	0.02	1.0	0.9	1998 Nov 19.22553	03 09 07.0	+16 33 21	22.8	42.0	11	1998-X17
1998 WX_{24}	43.3	0.04	0.9	0.9	1998 Nov 18.38490	03 25 15.4	+18 34 38	22.5	45.1	11	1998-X14
2000 CL_{104}	44.8	0.08	1.2	1.0	2000 Feb 5.38927	10 12 09.9	+11 20 55	22.0	42.6	9	2000-E64
2000 CE_{105}	44.2	0.06	0.5	1.0	2000 Feb 5.11756	07 15 11.3	+22 36 25	23.0	41.4	11	2000-F02
2001 FK_{185}	43.5	0.04	1.2	1.0	2001 Mar 25.34855	13 14 07.3	−07 03 36	25.0	41.7	7	2001-M34
2001 KE_{76}	43.1	0.03	0.5	1.0	2001 May 22.19395	15 43 24.6	−19 18 37	22.5	42.9	1	2001-M59
2001 QO_{297}	42.7	0.04	1.1	1.0	2000 Aug 26.21908	23 12 31.1	−05 35 41	22.3	43.5	2	2001-T38
2000 CF_{105}	44.2	0.04	0.5	1.1	2000 Feb 5.14503	08 11 10.8	+20 31 16	22.8	42.3	9	2000-F02
2003 FH_{127}	43.8	0.07	0.3	1.1	2003 Mar 30.19674	11 06 45.8	+05 58 18	23.4	37.0	3, 5	2003-H05
53311	44.3	0.06	0.4	1.2	1999 Apr 18.20550	13 29 32.7	−09 11 28	22.4	43.8	6	1999-K12
1998 WY_{31}	45.4	0.12	2.0	1.2	1998 Nov 18.42695	04 49 19.2	+22 47 18	23.1	45.3	11	1999-B26
1999 HS_{11}	44.3	0.02	2.6	1.2	1999 Apr 17.20248	13 34 18.7	−07 00 48	22.2	43.8	6	1999-K12
2002 CD_{251}	42.9	0.01	1.4	1.2	2002 Feb 8.22033	10 01 08.5	+13 40 09	23.0	42.5	5	2002-G19
2001 OQ_{108}	45.7	0.01	2.3	1.3	2001 May 24.02456	14 14 28.3	−10 59 47	22.8	45.8	2	2001-Q24
2001 QS_{322}	43.8	0.04	0.2	1.6	2001 Aug 19.24406	23 19 01.3	−04 24 35	21.5	42.3	5	2001-V12
2002 FW_{36}	43.2	0.03	2.4	1.6	2002 Mar 18.19343	10 23 58.8	+12 33 53	22.4	42.2	2, 10	2002-K12
2001 RW_{143}	42.8	0.03	3.0	1.9	2001 Sep 12.36734	00 56 15.0	+03 06 32	22.8	41.6	5	2001-V11
2002 CU_{154}	44.1	0.07	3.3	1.9	2002 Feb 6.20787	09 15 31.4	+17 33 10	22.2	41.2	5	2002-D25
1998 WV_{24}	39.0	0.04	1.5	2.0	1998 Nov 18.12480	02 45 33.3	+14 56 31	22.6	38.2	11	1998-X12
1999 HR_{11}	43.9	0.04	3.3	2.0	1999 Apr 17.16538	12 41 52.7	−00 59 36	22.9	42.3	6	1999-K12
2001 QJ_{298}	43.9	0.04	2.2	2.0	2001 Aug 21.16381	21 56 08.4	−11 56 33	21.3	45.2	5	2001-T54
2001 FK_{193}	44.3	0.07	3.5	2.1	2001 Mar 25.37166	13 44 35.2	−07 22 33	23.9	42.6	1, 2	2001-U19
2001 KT_{76}	45.4	0.10	1.7	2.1	2001 May 24.04654	14 19 54.0	−12 56 54	22.8	42.3	1	2001-M60
2001 QZ_{297}	44.1	0.06	1.9	2.2	2000 Aug 27.99951	20 38 56.5	−20 15 47	22.5	41.8	2	2001-T40
2002 CC_{249}	47.5	0.20	0.8	2.2	2002 Feb 8.37219	11 06 16.3	+04 49 45	21.8	38.9	8	2002-F27
2000 ON_{67}	42.8	0.03	3.1	2.3	2000 Jul 31.34031	22 39 12.7	−11 55 43	22.0	44.2	2	2000-T41
2001 FL_{185}	44.5	0.08	3.6	2.3	2001 Mar 26.14239	10 48 40.6	+11 28 29	23.6	40.9	7	2001-M34
2002 CB_{225}	44.4	0.09	3.8	2.3	2002 Feb 7.34740	10 43 02.5	+11 37 42	22.6	42.0	5	2002-D39
2002 VT_{130}	42.5	0.03	1.2	2.3	2002 Nov 7.33569	03 51 09.5	+21 21 24	21.4	42.7	7	2002-X10
2000 CQ_{114}	46.5	0.12	2.7	2.4	2000 Feb 6.35956	10 34 36.2	+11 36 10	22.6	45.1	11	2000-J45
2001 QX_{297}	43.9	0.03	0.9	2.4	2000 Aug 28.13725	21 52 13.7	−12 11 56	21.2	43.6	5	2001-T39
2002 VV_{130}[c]	42.5	0.19	2.4	2.4	2002 Nov 7.14405	01 15 31.9	+06 42 15	22.7	37.1	10	2002-X25
60454	44.6	0.09	1.2	2.5	2000 Feb 5.41595	10 52 10.0	+06 44 39	22.0	44.0	9	2000-F02
2001 KF_{76}	44.4	0.02	3.2	2.5	2001 May 22.20493	16 03 10.1	−21 25 34	22.7	44.5	1	2001-M59
2002 FX_{36}	44.5	0.04	1.1	2.5	2002 Mar 18.19731	10 34 46.5	+08 12 30	22.0	45.7	2, 10	2002-K12
1998 WX_{31}	45.6	0.11	3.0	2.6	1998 Nov 18.41641	04 24 39.2	+23 11 38	22.1	40.7	11	1999-B25
2001 RZ_{143}	43.9	0.06	2.1	2.6	2001 Sep 12.38169	01 09 49.6	+07 49 11	22.2	41.5	5	2001-V12
2002 PA_{149}[c]	42.6	0.12	4.1	2.6	2002 Aug 11.36045	23 18 05.0	−08 26 08	21.2	42.0	7, 8	2002-V20
1999 HH_{12}	43.8	0.02	1.3	2.7	1999 Apr 18.34230	14 36 05.8	−10 25 14	23.9	44.1	6	1999-N11
2001 QQ_{322}	43.8	0.05	4.0	2.7	2001 Aug 21.27515	23 09 02.4	−09 51 02	21.6	43.6	5	2001-V11
2003 UN_{284}	42.9	0.06	3.1	2.7	2003 Oct 24.38129	03 27 58.6	+19 51 50	23.2	42.5	5	2003-X20
1999 HV_{11}	43.1	0.02	3.2	2.8	1999 Apr 18.21595	13 34 59.9	−07 29 49	23.1	43.6	6	1999-K12
2000 CL_{105}	43.3	0.04	4.2	2.8	2000 Feb 6.29299	09 09 12.9	+17 58 09	22.4	45.0	11	2000-F02
2002 PQ_{145}	43.6	0.06	3.1	2.8	2002 Aug 10.13748	20 42 57.8	−16 13 59	20.9	45.9	8	2002-S49
2001 QT_{322}	36.9	0.02	1.8	2.9	2001 Aug 21.29450	23 26 39.5	−01 57 01	21.9	36.9	5	2001-V12
2000 CM_{105}	42.5	0.07	3.8	3.1	2000 Feb 6.29758	09 13 38.0	+20 05 07	22.1	41.7	9	2000-F02
2000 OU_{69}	43.0	0.04	4.4	3.1	2000 Jul 29.07350	20 06 22.7	−23 21 16	22.0	41.1	2	2001-M34
2001 QQ_{297}	44.2	0.08	4.4	3.1	2001 Aug 19.31029	23 40 41.5	−07 00 04	22.0	42.3	2	2001-T38
2002 CT_{154}	47.2	0.12	3.5	3.1	2002 Feb 6.40649	11 07 00.6	+06 02 25	22.7	41.8	5	2002-D24
1999 HJ_{12}	43.2	0.04	4.5	3.2	1999 Apr 18.34230	14 36 05.8	−10 25 14	23.6	44.2	6	1999-N11
2000 OL_{67}	44.9	0.11	2.0	3.2	2000 Jul 29.31302	22 32 00.0	−08 43 58	22.6	42.2	2	2000-T41
2000 CN_{105}	44.9	0.09	3.4	3.3	2000 Feb 6.34631	10 10 10.2	+14 31 46	21.4	45.7	11	2000-F02
2001 QB_{298}	42.4	0.09	1.8	3.3	2001 Aug 20.12602	21 46 05.2	−12 23 02	21.5	39.0	5	2001-T40

TABLE 9—*Continued*

Designation	a (AU)	e	i (deg)	i_K (deg)	UT Discovery Date	R.A. (J2000)	Decl. (J2000)	Frame Mag.	R (AU)	Desig. Telescope[a]	MPEC No.[b]
2003 KO_{20}[e]	46.0	0.01	1.8	3.4	2003 May 30.02965	14 04 05.7	−13 04 57	22.1	45.8	2	2003-N18
2002 PD_{149}	42.8	0.07	4.9	3.5	2002 Aug 11.36606	23 20 16.1	−09 07 57	22.1	45.4	8	2002-S49
1999 HT_{11}[c]	44.0	0.12	5.1	3.6	1999 Apr 17.24637	13 42 01.2	−05 39 49	23.1	41.6	6	1999-K12
2001 UN_{18}	44.1	0.08	3.6	3.6	2001 Oct 19.38168	01 09 29.0	+07 05 21	22.7	46.3	5	2001-V13
2002 XH_{91}	44.1	0.09	5.0	3.6	2002 Dec 4.42070	06 48 04.0	+24 42 58	21.7	47.7	5	2003-A05
2001 KN_{76}[c]	43.9	0.09	2.6	3.8	2001 May 23.98778	13 58 44.3	−14 45 52	22.7	40.6	1	2001-M60
2001 QD_{298}	42.4	0.05	5.0	3.8	2000 Aug 28.04742	21 27 59.2	−19 57 48	20.6	41.0	2, 5	2001-T41
2002 VE_{130}	44.6	0.06	3.3	3.8	2002 Nov 7.35099	04 01 42.1	+23 44 23	22.6	47.4	5	2002-W30
2001 QT_{297}	43.8	0.03	2.6	4.0	2000 Aug 1.29094	21 40 29.7	−13 03 36	21.0	44.9	5, 7	2001-T38
2000 OH_{67}	44.0	0.02	5.6	4.3	2000 Jul 29.24438	21 30 50.0	−20 00 27	22.5	43.5	2	2000-T41
2002 VS_{130}	45.1	0.12	3.0	4.4	2002 Nov 7.32383	03 33 09.9	+21 10 50	21.8	41.3	7	2002-X10
2003 FD_{128}	38.5	0.03	5.3	4.5	2003 Mar 31.30333	11 08 27.2	+07 14 05	22.7	37.6	3, 5	2003-H07
2001 FM_{185}	38.8	0.06	5.4	4.6	2001 Mar 26.15174	10 50 09.0	+08 30 00	23.5	39.0	5	2001-M34
2001 KH_{76}	46.1	0.12	3.3	4.7	2001 May 22.23447	16 27 37.3	−22 30 14	22.0	44.7	1	2001-M59
2003 QB_{91}[e]	43.3	0.13	6.2	5.1	2003 Aug 25.29780	00 09 19.3	−03 56 28	21.6	44.1	2	2003-Q58
2000 OK_{67}	46.3	0.13	4.9	5.2	2000 Jul 29.28069	22 15 13.1	−13 51 07	21.8	40.9	2	2000-T41
2001 UQ_{18}	44.2	0.06	5.2	5.6	2001 Oct 21.28067	03 19 40.7	+22 37 21	22.0	45.1	5	2001-V13
2002 GS_{32}[c]	42.4	0.11	4.3	5.7	2002 Apr 9.26285	14 57 05.8	−19 23 38	22.6	37.6	2	2002-K13
2003 UZ_{291}[e]	45.0	0.12	5.3	6.3	2003 Oct 22.37434	03 43 56.0	+18 38 49	22.8	48.0	5	2003-Y80
2002 PD_{155}	43.1	0.02	5.8	6.9	2002 Aug 12.29280	22 39 19.9	−06 42 37	21.7	43.0	5	2003-B55
1998 WW_{31}	44.7	0.08	6.8	7.9	1998 Nov 18.21509	03 21 32.6	+18 59 07	22.6	46.6	6, 11	1999-B24
2000 CP_{104}	44.6	0.10	9.5	8.3	2000 Feb 6.34631	10 09 49.8	+14 37 26	22.6	46.8	11	2000-E64
2002 CY_{248}	46.3	0.13	7.0	8.4	2002 Feb 6.15461	08 24 15.1	+18 52 29	21.6	52.1	10	2002-F27
2003 QX_{111}[e]	41.2	0.08	9.2	8.5	2003 Aug 25.27910	23 51 17.9	−04 17 23	21.5	39.0	3	2003-S19
2002 CZ_{154}	43.8	0.07	10.1	9.3	2002 Feb 6.42614	11 16 27.7	+07 19 19	22.9	40.9	5	2002-D25
2001 KU_{76}	45.2	0.16	10.6	9.9	2001 May 24.04654	14 20 15.2	−12 28 39	22.2	38.5	1	2001-M60
2000 CJ_{105}	44.4	0.10	11.6	10.8	2000 Feb 5.42049	10 56 38.0	+08 25 52	21.9	47.6	9	2000-F02
2001 FO_{185}	46.8	0.12	10.6	11.1	2001 Mar 26.38324	13 11 30.2	−08 52 35	24.2	41.2	5	2001-M34
19521	45.8	0.11	12.0	11.2	1998 Nov 19.41122	03 35 39.5	+20 47 23	20.5	43.0	7	1998-X08
2002 GJ_{32}	44.4	0.10	11.6	12.9	2002 Apr 9.22168	14 14 43.9	−19 21 40	20.5	42.8	2	2002-K12
2001 KA_{77}	47.5	0.09	11.9	13.1	2001 May 24.19589	16 27 47.6	−19 46 18	21.2	48.9	1, 7	2001-N01
2002 CX_{224}	46.2	0.13	16.9	16.1	2001 Oct 21.31035	03 29 33.6	+23 01 28	22.6	48.7	5	2002-D39

[a] Telescope(s) on which the frames used for object designation were taken: (1) Baade; (2) Blanco; (3) Clay; (4) INT; (5) Mayall; (6) NOT; (7) Perkins; (8) Shane; (9) Steward; (10) UH 2.2 m; (11) WIYN.
[b] Minor Planet Electronic Circular in which the object was designated.
[c] Classification based on nominal position and either the minus or plus 3 σ position.
[d] Object found in an untargeted observation, but for which the DES does not have official discovery credit according to MPC protocol.
[e] Classification based on nominal position.

in the histogram of Figure 5. The two bars farthest to the right show the designated, unclassified objects for the DES and all other surveys. For each of these bars, the lower hatched area represents those objects not yet lost—of which the DES has a much larger fraction, because of our extensive recovery program. Figure 6 shows plots of eccentricity (Fig. 6*a*) and inclination (Fig. 6*b*) versus semimajor axis for dynamically classified DES objects, and Figure 7 extends the plots of Figure 6 to larger semimajor axes. Orbital elements plotted in Figures 6 and 7 are osculating, heliocentric, and referenced to the mean ecliptic of J2000.

4. BIAS REMOVAL

A prime objective of our survey is to infer properties of the general population of KBOs. However, the properties of the objects, taken as a group, are influenced by various biases that make certain objects more likely to be discovered and recovered than others. In this section we discuss these biases, quantifying the effects where possible and describing our procedures for removing those biases that can be quantified. The procedure we describe here applies to establishing unbiased distribution functions without attempting to parameterize or model the distribution.

4.1. *General Procedure*

For a physical or orbital quantity q associated with each KBO (such as its orbital inclination), we want to infer the distribution function, $f_q(q)$, that applies to the general population (or a subset of the general population, such as a dynamical class). In this notation, $f_q(q)$ represents the fraction of objects per unit of q, so that the integral of $f_q(q)$ over all accessible values of q should equal unity. We shall also be interested in unnormalized distribution functions, such as the density of objects versus latitude. To establish these distribution functions for any desired quantity, we must remove the biases introduced by observational selection, data processing, recovery techniques, and other factors.

Generally we follow four steps for establishing the probability distribution for any particular quantity: (1) pick a set of survey nights to be used, (2) for each object discovered on those nights, calculate the relative probability to have found that object in each search field, (3) bin the objects and search fields into a set of intervals for the quantity, and (4) calculate a relative unbiased population fraction for each bin.

Specifically, consider a set of N_0 objects ($j = 1, \ldots, N_0$) discovered in a set of N_F search fields ($k = 1, \ldots, N_F$). Each

TABLE 10

Log of Discoveries: Unclassified Objects (Sorted by Decreasing Arc Length)

Designation	Arc Length (days)	UT Discovery Date	R.A. (J2000)	Decl. (J2000)	Frame Mag.	R (AU)	Desig. Telescope[a]	MPEC No.[b]
2002 PO_{149}	438.92	2002 Aug 12.30038	22 39 43.9	−09 11 57	21.8	46.3	2	2002-S50
2002 VA_{131}	380.02	2002 Nov 9.20366	01 40 07.3	+12 34 52	22.2	40.0	10	2002-X25
2003 FK_{127}	351.05	2003 Mar 30.25224	11 15 46.7	+07 15 34	22.5	40.8	5	2003-H05
2002 VB_{131}	350.11	2002 Nov 7.14405	01 14 44.4	+06 21 38	22.4	44.7	10	2002-X26
2003 UV_{292}	143.76	2003 Oct 24.41206	03 47 09.4	+19 26 34	22.2	33.9	5	2003-Y84
2003 WQ_{188}	98.78	2003 Nov 20.46691	06 27 01.3	+28 02 03	22.6	48.2	5	2003-Y79
2003 WU_{188}	96.85	2003 Nov 24.40778	06 09 57.4	+23 55 33	21.7	43.1	7	2004-A44
2003 QE_{91}	92.97	2003 Aug 23.14198	22 32 27.1	−11 34 05	22.5	42.3	2	2003-Q59
2003 QR_{91}	91.97	2003 Aug 25.02878	20 55 13.7	−15 00 42	20.8	38.7	2	2003-Q60
2001 KW_{76}	90.82	2001 May 22.19395	15 42 00.1	−18 51 18	23.0	40.4	1	2001-N01
2003 QH_{91}	89.05	2003 Aug 25.03681	21 00 49.8	−15 12 53	21.9	41.7	2	2003-Q59
2001 KE_{77}	88.85	2001 May 24.22514	16 34 03.7	−18 20 41	22.9	38.7	1	2001-N03
2003 QA_{112}	87.82	2003 Aug 26.27197	23 04 40.3	−11 34 07	21.5	47.2	3	2003-S19
2002 GU_{32}	69.94	2002 Apr 9.25899	14 55 41.9	−11 20 36	21.7	36.1	2	2002-K13
2002 GN_{32}	66.06	2002 Apr 6.19153	14 08 32.4	−13 37 07	21.0	34.3	10	2002-K13
1998 WZ_{24}	64.91	1998 Nov 18.44295	05 03 14.5	+22 28 12	22.5	32.0	1	1998-X16
2003 FM_{127}	62.96	2003 Apr 1.40718	14 04 27.5	−11 01 27	22.8	42.5	3, 5	2003-H05
2001 QF_{331}	62.89	2001 Aug 19.23948	23 18 35.7	−05 01 44	21.5	35.1	5	2003-B55
2003 QU_{90}	62.03	2003 Aug 24.10783	22 11 57.9	−09 11 29	22.5	42.9	2	2003-Q58
2003 QO_{91}	61.97	2003 Aug 24.24550	22 45 18.2	−10 17 57	21.7	39.6	2	2003-Q60
2003 QG_{91}	61.08	2003 Aug 24.01276	20 50 56.0	−19 58 44	22.7	41.9	2	2003-Q59
2003 QV_{91}	61.06	2003 Aug 24.26947	23 06 15.6	−07 48 58	22.9	38.4	2	2003-Q61
2003 QB_{92}	61.03	2003 Aug 25.20245	21 53 00.4	−14 29 47	21.9	37.2	2	2003-Q61
2003 QT_{90}	61.02	2003 Aug 23.18206	23 10 46.1	−06 24 08	22.1	45.6	2	2003-Q58
2003 QP_{91}	60.99	2003 Aug 24.30123	23 31 31.2	−07 26 54	21.8	39.6	2	2003-Q60
2003 QF_{91}	60.98	2003 Aug 23.16993	23 03 11.3	−08 25 42	22.5	42.0	2	2003-Q59
2003 QY_{90}	60.96	2003 Aug 24.09096	21 49 12.5	−15 49 08	21.3	44.8	2	2003-Q58
2003 QQ_{91}	60.94	2003 Aug 24.32825	00 05 25.0	−04 36 56	22.1	41.4	2	2003-Q60
2003 QV_{90}	60.92	2003 Aug 24.30508	23 35 00.0	−04 12 10	22.0	44.0	2	2003-Q58
2003 QX_{91}	60.92	2003 Aug 24.27331	23 10 05.5	−09 49 37	22.5	33.4	2	2003-Q61
2002 GV_{32}	60.14	2002 Apr 9.27375	15 02 14.8	−14 04 27	21.3	34.3	2	2002-K13
2003 QX_{90}	60.07	2003 Aug 24.03648	21 11 32.1	−19 29 45	21.8	44.7	2	2003-Q58
2003 QN_{91}	60.06	2003 Aug 25.23376	22 38 06.4	−11 51 12	21.7	38.3	2	2003-Q60
2003 QS_{91}	60.03	2003 Aug 25.21054	22 07 47.1	−08 34 12	22.4	40.3	2	2003-Q60
2003 QL_{91}	59.94	2003 Aug 26.21790	22 12 35.8	−10 41 27	21.9	42.7	2	2003-Q59
2003 QC_{112}	59.88	2003 Aug 24.26947	23 06 17.4	−07 45 44	21.8	25.4	3	2003-S20
2003 QA_{91}	59.85	2003 Aug 25.20245	21 53 22.8	−14 32 23	21.2	45.2	2	2003-Q58
2003 GF_{55}	59.65	2003 Apr 1.39515	13 47 44.2	−06 37 34	23.0	46.0	2	2003-N18
2003 QE_{112}	59.15	2003 Aug 26.08132	22 05 31.4	−15 27 10	21.5	44.9	7	2003-T20
2003 QW_{111}	58.86	2003 Aug 25.23376	22 39 11.6	−11 27 14	21.6	45.9	3	2003-S19
2003 QT_{91}	58.84	2003 Aug 26.26631	23 15 12.6	−04 53 27	22.0	41.4	2	2003-Q60
2003 QC_{91}	58.76	2003 Aug 26.23401	22 32 03.3	−09 15 07	22.6	43.3	2	2003-Q58
2003 QY_{111}	57.97	2003 Aug 25.27910	23 51 34.5	−04 08 53	22.2	42.6	3	2003-S19
2003 QM_{91}	57.87	2003 Aug 26.28761	23 33 52.4	−03 45 37	20.0	44.4	2	2003-Q59
2003 QU_{91}	57.87	2003 Aug 26.29153	23 39 10.7	−00 28 38	22.1	39.5	2	2003-Q60
2002 XF_{91}	56.98	2002 Dec 4.37398	06 09 41.2	+21 38 39	22.3	42.0	5	2003-A05
2002 XE_{91}	56.97	2002 Dec 4.37006	06 06 12.6	+24 05 39	22.4	51.4	5	2003-A05
2003 QZ_{111}	56.96	2003 Aug 26.25819	22 52 18.9	−06 23 40	22.0	40.2	3	2003-S19
2003 QB_{112}	56.96	2003 Aug 26.30322	00 02 06.3	−03 06 41	21.8	40.5	3	2003-S19
2003 QD_{112}	56.95	2003 Aug 26.29534	23 53 53.0	−02 12 15	20.3	11.5	3	2003-S20
2001 FU_{185}	56.86	2001 Mar 26.22648	12 12 24.2	−05 07 10	25.3	34.6	2	2001-N03
2001 FV_{185}	56.77	2001 Mar 26.34637	12 25 39.1	+01 03 32	24.1	34.6	2	2001-N03
2001 FS_{185}	56.76	2001 Mar 26.41581	13 48 47.1	−06 28 06	24.0	41.5	2	2001-M60
2000 CO_{114}	53.88	2000 Feb 5.38049	10 01 49.0	+16 44 29	23.5	49.2	11	2000-J45
2000 CP_{114}	53.00	2000 Feb 6.27528	09 01 08.1	+20 09 49	23.4	39.0	11	2000-J45
2002 FY_{36}	51.07	2002 Mar 20.23512	11 07 52.2	+04 05 37	22.2	25.8	2	2002-K15
1999 HD_{12}	49.83	1999 Apr 17.15461	12 31 54.8	−01 03 07	22.9	13.1	6	1999-K18
1999 HA_{12}	49.82	1999 Apr 17.19181	13 30 41.3	−05 34 46	23.4	40.9	6	1999-K15
2002 CQ_{154}	41.96	2002 Feb 6.33930	10 32 02.9	+10 13 11	22.4	43.2	5	2002-D24
2002 CC_{251}	41.94	2002 Feb 6.34319	10 33 08.0	+11 33 16	23.5	34.0	5	2002-G19
2003 QD_{91}	40.28	2003 Aug 23.14198	22 31 07.4	−11 40 07	22.2	41.2	2	2003-Q59
2003 QZ_{91}	39.32	2003 Aug 24.04059	21 13 50.0	−19 37 15	20.7	24.3	2	2003-Q61
2003 QJ_{91}	39.28	2003 Aug 25.06814	21 17 23.1	−17 53 47	22.4	45.0	2	2003-Q59
2003 QA_{92}	39.26	2003 Aug 24.09096	21 47 52.8	−15 24 31	20.7	37.6	2	2003-Q61

TABLE 10—*Continued*

Designation	Arc Length (days)	UT Discovery Date	R.A. (J2000)	Decl. (J2000)	Frame Mag.	*R* (AU)	Desig. Telescope[a]	MPEC No.[b]
2003 KP_{20}	39.18	2003 May 30.24183	16 46 51.5	−21 14 00	22.4	40.0	2	2003-N19
2001 RY_{143}	38.86	2001 Sep 12.37098	00 56 48.3	+08 03 36	23.4	49.6	5	2001-V12
2003 QK_{91}	38.09	2003 Aug 26.02489	20 52 58.4	−15 01 15	21.8	40.6	2	2003-Q59
2001 RV_{143}	38.02	2001 Sep 12.33019	00 46 29.6	+03 33 32	22.7	43.0	5	2001-V11
2003 LC_{7}	37.29	2003 Jun 2.16051	16 27 23.9	−20 44 59	22.2	52.0	2	2003-N19
2003 LA_{7}	37.28	2003 Jun 2.14881	15 42 00.6	−22 07 19	21.6	46.4	2	2003-N18
2003 LF_{7}	37.26	2003 Jun 2.15656	15 47 51.2	−22 04 06	22.3	34.9	2	2003-N20
2001 RL_{155}	37.07	2001 Sep 12.32214	00 39 07.2	+05 16 01	23.5	39.1	5	2003-C12
2002 CO_{154}	37.02	2002 Feb 6.20390	09 12 09.4	+16 25 05	23.0	42.6	5	2002-D24
2002 CA_{249}	36.97	2002 Feb 6.19986	09 12 54.7	+15 48 24	22.0	12.8	8	2002-F27
2003 LB_{7}	36.32	2003 Jun 2.11348	15 16 58.4	−18 17 19	21.4	39.1	2	2003-N19
2003 LD_{7}	36.19	2003 Jun 2.16444	16 28 29.6	−19 50 39	21.9	41.2	2	2003-N19
2003 LD_{9}	36.19	2003 Jun 1.12481	16 28 49.1	−20 21 29	23.1	39.7	7	2003-P05
2003 LG_{7}	35.18	2003 Jun 2.14031	15 34 49.5	−19 55 14	22.3	33.1	2	2003-N20
2002 CB_{249}	34.81	2002 Feb 8.38018	11 04 37.1	+09 12 56	20.9	14.2	7	2002-F27
2002 CZ_{224}	34.16	2002 Feb 8.18356	09 09 12.8	+18 03 10	22.9	47.4	5	2002-D39
2002 CA_{225}	34.00	2002 Feb 8.22033	09 59 00.9	+13 08 56	23.1	40.7	5	2002-D39
2003 US_{291}	32.87	2003 Oct 22.31593	02 49 56.5	+15 52 41	23.2	45.3	5	2003-Y79
2003 UB_{292}	32.05	2003 Oct 23.19270	02 06 50.3	+15 17 04	22.1	50.4	5	2003-Y80
2003 UQ_{292}	32.03	2003 Oct 23.21645	02 08 48.7	+09 58 08	21.4	35.0	5	2003-Y84
2003 UR_{292}	31.92	2003 Oct 24.19583	00 38 52.5	+02 03 30	20.8	27.3	5	2003-Y84
2002 CV_{154}	31.15	2002 Feb 6.35895	10 46 09.8	+10 36 52	23.1	47.5	5	2002-D25
2002 CR_{154}	31.07	2002 Feb 6.35104	10 40 12.8	+12 17 00	23.1	42.0	5	2002-D24
2002 CP_{154}	30.25	2002 Feb 6.20787	09 13 57.2	+17 30 14	21.9	42.5	5	2002-D24
2002 CZ_{248}	30.24	2002 Feb 6.17091	08 54 38.8	+17 02 05	22.7	36.2	10	2002-F27
2003 GM_{53}	30.10	2003 Apr 1.37064	13 19 24.4	−10 43 58	22.5	44.8	10	2003-K17
2002 PG_{150}	30.05	2002 Aug 12.30876	23 21 54.2	−10 16 36	22.9	37.2	8	2002-S51
2003 UO_{292}	29.97	2003 Oct 22.33546	03 08 15.6	+16 14 48	22.1	32.6	5	2003-Y84
2003 UT_{291}	29.96	2003 Oct 22.33145	03 01 39.5	+17 02 54	22.6	44.8	5	2003-Y79
2003 UV_{291}	29.95	2003 Oct 23.20080	02 10 09.7	+13 34 50	23.3	44.2	5	2003-Y79
2002 GG_{166}	29.39	2002 Apr 9.03136	12 38 23.7	−00 39 16	21.9	30.8	10	2002-L21
2002 GJ_{166}	29.38	2002 Apr 9.04640	12 43 07.8	−01 06 21	22.5	31.9	10	2002-L21
2002 GH_{166}	29.37	2002 Apr 9.04270	12 41 59.4	−04 40 33	20.7	33.6	10	2002-L21
2002 PN_{149}	29.03	2002 Aug 12.27617	22 07 41.8	−11 12 34	22.3	41.9	8	2002-S50
2003 UA_{292}	29.00	2003 Oct 22.37434	03 44 29.5	+18 41 03	23.5	53.6	5	2003-Y80
2003 UE_{292}	29.00	2003 Oct 23.34395	03 19 57.0	+21 47 48	22.2	38.1	5	2003-Y80
2003 UD_{292}	28.99	2003 Oct 23.33629	03 16 25.6	+14 23 05	22.6	41.3	5	2003-Y80
2003 UY_{292}	28.98	2003 Oct 23.34395	03 19 58.6	+22 11 30	21.9	15.9	5	2003-Y84
2000 QO_{252}	28.95	2000 Aug 28.17999	22 30 11.3	−07 05 49	22.4	39.4	2	2003-C11
2003 UU_{291}	28.05	2003 Oct 23.16899	01 23 17.0	+07 24 49	23.2	44.1	5	2003-Y79
2003 UC_{292}	28.05	2003 Oct 23.20490	02 10 25.0	+12 32 53	22.6	41.5	5	2003-Y80
2003 UP_{292}	28.05	2003 Oct 23.18856	02 04 06.7	+14 15 16	22.0	29.6	5	2003-Y84
2003 UW_{292}	28.04	2003 Oct 23.20876	02 10 06.1	+11 12 04	21.0	19.4	5	2003-Y85
2003 UW_{291}	28.03	2003 Oct 23.21264	02 10 32.1	+10 24 04	22.5	44.5	5	2003-Y79
2003 UX_{292}	28.03	2003 Oct 23.21264	02 09 08.8	+10 31 41	22.2	39.0	5	2003-Y84
2003 UK_{293}	28.03	2003 Nov 20.15834	02 06 57.7	+10 39 28	22.5	41.4	5	2004-C56
2003 UX_{291}	28.00	2003 Oct 23.36340	03 33 33.5	+15 03 11	23.4	46.4	5	2003-Y79
2003 UF_{292}	28.00	2003 Oct 23.35950	03 30 09.5	+15 46 21	22.7	39.6	5	2003-Y80
2003 UG_{292}	28.00	2003 Oct 23.38278	03 44 44.5	+15 55 09	22.7	39.4	5	2003-Y80
2003 UL_{292}	27.99	2003 Oct 24.32681	03 13 12.0	+13 58 14	23.3	41.8	5	2003-Y80
2003 UU_{292}	27.98	2003 Oct 24.35068	03 21 03.7	+14 37 41	23.4	34.7	5	2003-Y84
2003 UK_{292}	27.97	2003 Oct 24.32681	03 10 55.6	+14 23 20	23.2	47.4	5	2003-Y80
2003 UM_{292}	27.97	2003 Oct 24.36220	03 23 16.0	+15 36 50	22.5	38.1	5	2003-Y80
2003 UT_{292}	27.97	2003 Oct 24.33088	03 14 07.3	+12 05 47	21.2	31.4	5	2003-Y84
2003 UZ_{292}	27.97	2003 Oct 24.33530	03 16 34.3	+13 03 19	23.1	38.0	5	2003-Y84
2000 QN_{252}	27.92	2000 Aug 28.04279	21 21 16.4	−14 07 15	23.4	36.4	2	2003-C11
2003 UH_{292}	27.00	2003 Oct 24.20353	00 52 26.3	+02 49 53	23.5	41.2	5	2003-Y80
2003 US_{292}	27.00	2003 Oct 24.20735	00 57 03.7	+04 00 38	22.7	32.8	5	2003-Y84
2003 UJ_{292}	26.99	2003 Oct 24.21518	01 04 51.0	+06 14 39	21.8	40.8	5	2003-Y80
2003 UN_{292}	26.97	2003 Oct 24.37748	03 29 46.7	+19 26 40	23.1	41.3	5	2003-Y80
2000 QK_{252}	26.94	2000 Aug 27.00871	20 42 11.5	−16 28 35	23.0	52.9	2	2003-C11
2000 QL_{252}	26.89	2000 Aug 27.14216	22 26 33.6	−06 35 28	22.7	37.5	2	2003-C11
2002 VG_{131}	26.02	2002 Nov 9.17961	00 54 58.0	+12 07 52	22.5	14.7	10	2002-X26
2002 VE_{131}	25.09	2002 Nov 7.37778	04 33 57.2	+18 41 43	23.4	57.2	10	2002-X26
2002 VW_{130}	25.07	2002 Nov 7.17311	01 18 05.7	+08 51 27	22.6	41.5	10	2002-X25

TABLE 10—*Continued*

Designation	Arc Length (days)	UT Discovery Date	R.A. (J2000)	Decl. (J2000)	Frame Mag.	*R* (AU)	Desig. Telescope[a]	MPEC No.[b]
2000 CN_{104}	24.87	2000 Feb 5.38927	10 12 46.1	+11 12 32	22.5	42.8	9	2000-E64
2002 VC_{131}	24.08	2002 Nov 7.15253	01 12 13.0	+05 30 20	22.5	49.0	10	2002-X26
2002 VY_{130}	24.07	2002 Nov 7.31992	03 27 12.8	+18 22 57	23.1	33.1	10	2002-X25
2002 VF_{131}	24.05	2002 Nov 7.38945	04 46 10.1	+20 30 15	22.5	47.5	10	2002-X26
2000 CS_{105}	24.00	2000 Feb 6.38156	10 54 52.7	+10 25 07	22.5	38.8	9	2000-F07
2000 QJ_{252}	23.91	2000 Aug 25.18831	22 35 09.2	−10 44 29	23.0	38.3	2	2003-C11
2001 QR_{297}	23.17	2001 Aug 20.11433	21 42 19.2	−13 19 28	21.6	43.8	5	2001-T38
2001 QU_{297}	23.17	2001 Aug 20.12970	21 53 23.6	−14 40 20	22.1	42.8	2	2001-T39
2001 QS_{297}	23.16	2001 Aug 20.11804	21 41 45.8	−12 27 36	21.9	43.5	2	2001-T38
2002 VZ_{130}	23.11	2002 Nov 9.19187	01 15 55.3	+12 36 15	23.1	41.7	10	2002-X25
2001 QG_{331}	22.14	2001 Aug 21.15991	21 56 27.6	−11 11 03	21.5	39.3	5	2003-C12
2000 CM_{104}	21.88	2000 Feb 5.38927	10 12 32.6	+11 06 54	23.0	42.5	11	2000-E64
2000 CP_{105}	21.10	2000 Feb 5.17626	09 03 44.1	+16 54 48	22.6	37.1	11	2000-F07
2000 CY_{105}	21.07	2000 Feb 5.16269	08 43 10.5	+17 24 14	23.5	49.2	11	2000-F46
1999 HZ_{11}	19.86	1999 Apr 17.15990	12 39 51.9	−00 28 24	24.0	37.4	6	1999-K15
1999 HY_{11}	19.85	1999 Apr 17.14936	12 32 04.8	−00 13 21	23.9	39.8	6	1999-K15
2001 KM_{76}	18.87	2001 May 22.23814	16 28 38.9	−20 30 59	22.5	41.7	1	2001-M60
2001 KS_{76}	17.05	2001 May 24.03559	14 20 19.7	−11 24 34	23.2	40.2	1	2001-M60
2001 KZ_{76}	17.05	2001 May 24.02820	14 14 54.7	−10 14 42	23.4	42.8	1	2001-N01
2001 KQ_{76}	16.04	2001 May 24.01356	14 03 48.6	−10 52 11	22.4	41.6	1	2001-M60
2002 GX_{31}	4.41	2002 Apr 6.19898	14 19 02.4	−12 40 13	22.7	40.1	2, 10	2002-K12
2002 GY_{31}	4.41	2002 Apr 6.21029	14 25 53.1	−14 35 50	22.1	42.5	2, 10	2002-K12
2002 GM_{32}	4.41	2002 Apr 6.17600	13 21 36.2	−14 52 08	22.3	27.9	10	2002-K13
2002 GC_{32}	4.36	2002 Apr 7.15670	13 34 56.7	−07 51 33	22.9	41.9	2, 10	2002-K12
2002 GR_{32}	4.31	2002 Apr 7.16033	13 46 25.0	−10 54 17	21.8	29.8	10	2002-K13
2002 GQ_{32}	4.30	2002 Apr 7.14880	13 29 33.0	−09 02 37	22.1	33.0	10	2002-K13
2003 WS_{184}	4.05	2003 Nov 20.32284	04 10 17.5	+18 52 36	23.2	41.9	5	[c]
2003 WV_{188}	3.98	2003 Nov 20.28249	03 28 15.5	+16 00 36	23.8	45.8	5	2004-C56
2002 PE_{155}	3.09	2002 Aug 12.15575	20 53 59.0	−15 02 13	22.1	43.1	2	2003-C12
2003 WW_{188}	3.07	2003 Nov 21.38531	05 51 18.8	+28 38 22	22.8	41.1	5	2004-C56
2002 GV_{31}	2.97	2002 Apr 8.99899	10 23 45.0	+12 23 59	21.1	39.4	2	2002-K12
2002 PJ_{149}	1.13	2002 Aug 12.27980	22 06 48.2	−09 04 14	21.8	48.4	2	2002-S51
2002 PK_{149}	1.13	2002 Aug 12.27980	22 07 45.4	−09 26 10	22.3	37.0	2	2002-S50
2002 GT_{32}	1.12	2002 Apr 9.22541	14 34 16.0	−12 51 05	22.8	32.8	2	2002-K13
2003 LZ_{6}	1.12	2003 Jun 2.11739	15 15 36.0	−17 40 07	22.5	43.4	2	2003-N18
2003 LE_{7}	1.12	2003 Jun 2.11739	15 17 10.6	−17 50 29	22.2	32.0	2	2003-N20
2002 GO_{32}	1.11	2002 Apr 6.25380	14 42 55.8	−14 33 31	22.8	36.3	2	2002-K13
2002 PL_{149}	1.10	2002 Aug 12.26890	22 04 43.5	−09 57 50	22.7	19.8	2	[c]
2003 QW_{91}	1.10	2003 Aug 23.18206	23 10 41.4	−06 40 53	23.3	29.6	2	2003-Q61
2001 QV_{297}	1.09	2001 Aug 20.12970	21 54 43.2	−14 49 30	22.3	43.9	2	2001-T39
2002 CW_{154}	1.09	2002 Feb 6.38675	10 58 58.9	+08 58 45	23.0	49.0	5	2002-D25
2002 GE_{32}	1.09	2002 Apr 8.12135	13 15 06.0	−08 54 36	22.4	39.8	2	2002-K12
2003 QY_{91}	1.07	2003 Aug 24.32434	00 02 38.8	−04 34 56	22.4	35.4	2	2003-Q61
2000 QA_{243}	1.06	2000 Aug 26.28602	23 26 03.7	−02 01 51	23.1	43.2	2	2000-T42
2003 WS_{188}	1.06	2003 Nov 20.42485	05 35 21.3	+29 06 43	23.4	30.8	5	2003-Y84
2002 PE_{149}	1.04	2002 Aug 12.08848	20 56 10.5	−23 37 11	22.6	43.0	2	2002-S49
2002 PQ_{149}	1.04	2002 Aug 12.30468	22 42 47.1	−07 50 06	21.5	37.3	2	2002-S50
2002 XJ_{91}	1.04	2002 Dec 5.16228	03 54 58.7	+24 17 18	22.9	31.8	5	2003-A05
2002 GK_{32}	1.01	2002 Apr 9.22903	14 41 09.5	−13 02 40	22.4	43.1	2	2002-K12
2002 PF_{149}	1.01	2002 Aug 12.10351	21 30 29.9	−17 42 44	22.5	42.8	2	2002-S49
2003 QZ_{90}	1.01	2003 Aug 25.02878	20 54 44.4	−15 13 58	22.7	43.5	2	2003-Q58
2002 PH_{149}	1.00	2002 Aug 12.12272	21 39 36.5	−19 10 25	22.3	40.6	2	2002-S51
2002 PM_{149}	1.00	2002 Aug 12.14197	22 04 02.9	−10 17 05	21.4	41.8	2	2002-S51
2003 LH_{7}	1.00	2003 Jun 2.16444	16 29 06.3	−20 02 19	22.8	12.7	2	2003-N20
2002 XD_{91}	0.99	2002 Dec 4.34647	05 31 16.6	+24 45 17	22.7	35.2	5	2003-A05
2002 XG_{91}	0.99	2002 Dec 4.38567	06 22 31.4	+23 33 22	23.1	38.1	5	2003-A05
2002 PN_{147}	0.97	2002 Aug 10.14123	20 44 19.3	−19 35 49	22.4	44.4	2	2002-S49
2003 KQ_{20}	0.96	2003 May 30.22260	16 33 32.9	−22 12 50	21.8	8.7	2	2003-N20

[a] Telescope(s) on which the frames used for object designation were taken: (1) Baade; (2) Blanco; (3) Clay; (4) INT; (5) Mayall; (6) NOT; (7) Perkins; (8) Shane; (9) Steward; (10) UH 2.2 m; (11) WIYN.

[b] Minor Planet Electronic Circular in which the object was designated.

[c] Given a provisional designation from the MPC but an MPEC was never issued.

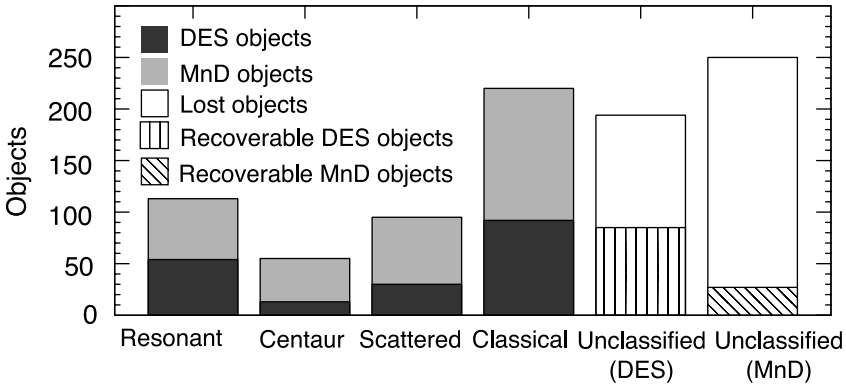

FIG. 5.—Dynamical classifications of all MPC-designated objects. The bars above the headings "Resonant," "Centaur," "Scattered," and "Classical" represent provisional dynamical classifications (see § 3.4), with the black areas corresponding to designated DES objects and the gray areas corresponding to designated MPC objects that are not DES objects ("MnD"). The two bars at the far right correspond to designated objects that are not yet dynamically classified in the DES and MnD categories. The hatched segments of these bars correspond to objects that are not yet "lost," and the clear segments correspond to "lost" objects. We define an object to be "lost" if the error in its position exceeds 1000″ (approximately half the width of a Mosaic field). By definition, an object is securely classified if the fractional uncertainty (3 σ) in its initial semimajor axis is less than 10%, and if initial orbital solutions 1, 2, and 3 yield identical classifications (based on a 10 Myr integration).

object has associated with it a value q_j for the quantity of interest, and we want to determine the unbiased fraction of the population accessible to our survey for a set of N_q bins ($n = 1, \ldots, N_q$) that we have chosen for q. We define $\zeta_{j,k}$ to be a quantity proportional to the probability that an object with a value q_j would have been detected in the kth search field, and we define the object likelihood factor, ζ_j—which is proportional to the probability that the jth object would have been detected in any of the search fields—to be the sum of the $\zeta_{j,k}$ over all search fields:

$$\zeta_j = \sum_{k=1}^{N_F} \zeta_{j,k}. \tag{2}$$

The next step is to assign each object to one of the N_q bins for the quantity of interest. We define Z_n as a quantity that is proportional to the probability of finding an object in the nth bin, which contains N_n objects. Values for the likelihood factor Z_n can be determined in several ways. First, one could assume that the density of objects per interval of q is constant over the bin and then solve for Z_n analytically or numerically. When one is not concerned about the distribution function varying within a bin and has good a priori knowledge of the likelihood factors, this would be the most robust method. Or, one could simply average ζ_j for the detected objects in the bin. This approach would be preferred if the object likelihood factors were likely to contain significant errors in a parameter affecting the likelihood, as is the case for objects near the detection limit. We define an index j' for the objects in the nth bin and write an equation for Z_n as follows:

$$Z_n = \frac{1}{N_n} \sum_{j'=1}^{N_n} \zeta_{j'} \tag{3}$$

for cases when the likelihood factor might be changing over the bin. When we have good a priori knowledge of the likelihood factor (as for the inclination distribution), the most accurate approach is to set the reciprocal of Z_n equal to the average of the reciprocals of the object likelihood factors, ζ_j, for all objects in the nth bin:

$$\frac{1}{Z_n} = \frac{1}{N_n} \sum_{j'=1}^{N_n} \frac{1}{\zeta_{j'}}. \tag{4}$$

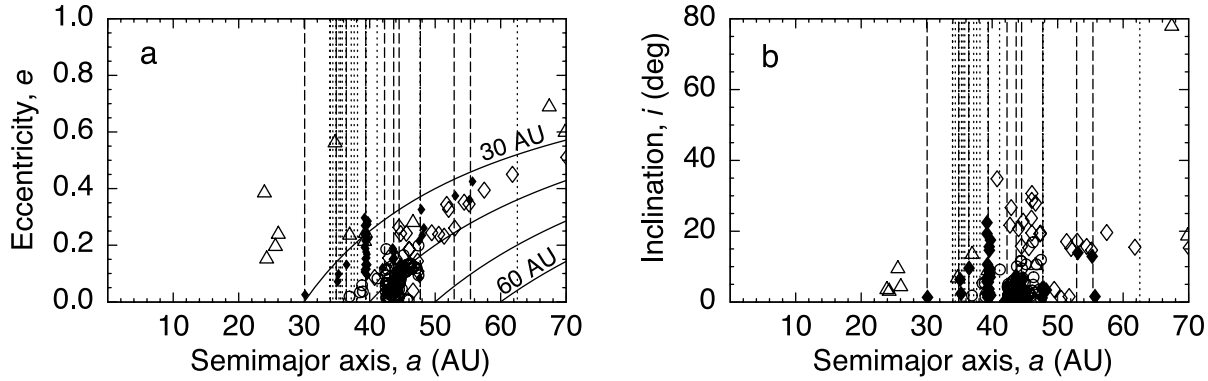

FIG. 6.—(*a*) Eccentricities and (*b*) inclinations for dynamically classified KBOs with semimajor axes less than 70 AU. Filled symbols and open symbols represent Resonant and nonresonant objects, respectively. For the open symbols, the triangles represent the Centaurs, the diamonds represent the Scattered (Near and Extended), and circles represent the Classical objects. Vertical lines indicate locations of nominal resonances with Neptune, with the dashed lines representing those for which we have found members. In (*a*), each solid line corresponds to a constant perihelion distance. Only DES objects have been plotted. Orbital elements refer to osculating, heliocentric orbits for the mean ecliptic and epoch of J2000.

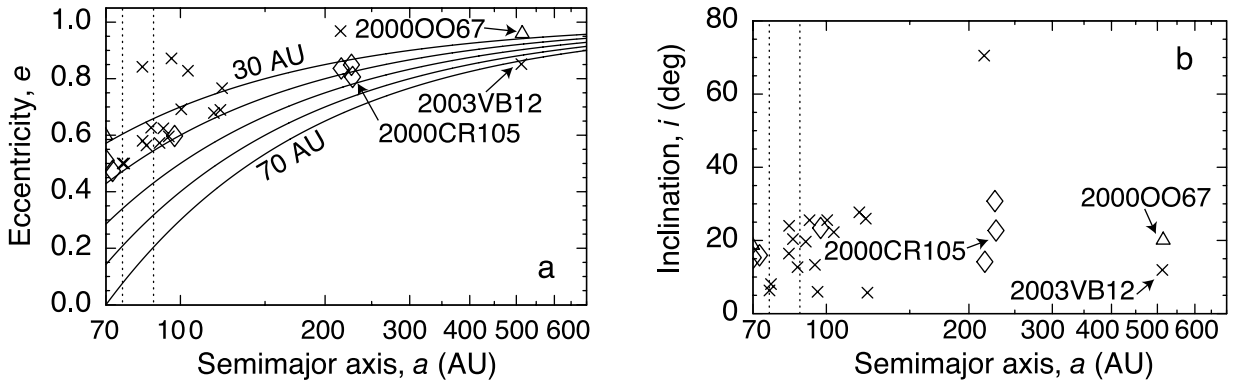

FIG. 7.—(*a*) Eccentricities and (*b*) inclinations for dynamically classified KBOs in the outermost regions of the solar system. Dotted lines correspond to the nominal locations of the 4:1 and 5:1 resonances, but all objects in this figure are nonresonant. Open symbols represent objects discovered by the DES, with the diamonds corresponding to Scattered (Near and Extended) objects and the triangles to Centaurs. The crosses represent objects not discovered by the DES. In (*a*), each solid line corresponds to a constant perihelion distance. Orbital elements refer to osculating, heliocentric orbits for the mean ecliptic and epoch of J2000.

The results will be the most accurate if one can choose bins with significant numbers of objects and with the differences among the ζ_j for objects within the bin not showing great disparity. This ideal may not always be attainable in practice.

If $f_{q,n}$ is the unbiased fraction of the population per unit interval for q (for which the observed objects are a sample) for the nth bin, γ is a constant of proportionality, and Δq_n is the width of the nth bin, then, on average, these quantities are related by the equation

$$N_n = \gamma f_{q,n} \Delta q_n \mathrm{Z}_n. \tag{5}$$

Noting that the sum of $f_{q,n}\Delta q_n$ over all N_q bins must equal unity, we solve equation (5) for $f_{q,n}\Delta q_n$, sum over all bins, and then solve the resulting equation for γ:

$$\gamma = \sum_{n=1}^{N_q} \frac{N_n}{\mathrm{Z}_n}. \tag{6}$$

With this knowledge, we can now solve equation (5) for $f_{q,n}$, which we write with i' as a dummy summation index in place of n:

$$f_{q,n} = \frac{N_n/\mathrm{Z}_n}{\Delta q_n \sum_{i'=1}^{N_q} (N_{i'}/\mathrm{Z}_{i'})}. \tag{7}$$

Next, we write an equation for the error in $f_{q,n}$, which we denote by $\sigma(f_{q,n})$, based on the standard deviation for a binomial distribution for N_0 independent trials with a probability of success of $f_{q,n}\Delta q_n$ for each trial:

$$\sigma(f_{q,n}) = \sqrt{\frac{f_{q,n}(1 - f_{q,n}\Delta q_n)}{\Delta q_n N_0}}. \tag{8}$$

Finally, we write an equation for the fractional error in $f_{q,n}$, which we see is approximately the reciprocal of the square root of the number of objects in the nth bin:

$$\frac{\sigma(f_{q,n})}{f_{q,n}} = \sqrt{\frac{1 - f_{q,n}\Delta q_n}{f_{q,n}\Delta q_n N_0}} \approx \frac{1}{\sqrt{f_{q,n}\Delta q_n N_0}}. \tag{9}$$

Hence a sample of 100 objects equally divided into 10 bins would have fractional errors of about ±30% on the empirical distribution function.

This concludes our general approach for removing observational biases when determining an empirical distribution function, $f_{q,n}(q)$, with the biases encapsulated in the relative probabilities, $\zeta_{j,k}$, that appear in equation (2).

4.2. *Quantifying Bias Effects*

In Table 11 we list the factors that may have introduced biases into the samples of objects given in Table 4. We divide these biases into several categories; we list separately those biases that are inherent to (1) properties of the search fields, (2) characteristics of the observations, (3) characteristics of the objects, (4) data reduction techniques, and (5) characteristics of

TABLE 11
BIAS EFFECTS

Category	Bias
Search fields	Kuiper belt plane latitude[a]
	Kuiper belt plane longitude
	Density of stars and galaxies[a]
	Time since last visit
	Solar elongation
Observations	Limiting magnitude[a]
	Image quality
	Filter
	Mismatch in field registration[a]
	Saturated objects[a]
	Magnitude[a]
Objects	Color
	Rate of motion
	Orbital elements[b]
	Distance
	Kuiper belt plane coordinates
Reduction	Detection efficiency[a]
	Detection algorithm
Recovery	Recovery opportunities
	Number of attempts
	Difficulty of recovery
	Uniqueness of orbit

[a] Bias that has been quantified for the analyses in this paper.
[b] Only inclination bias has been quantified for the analyses in this paper.

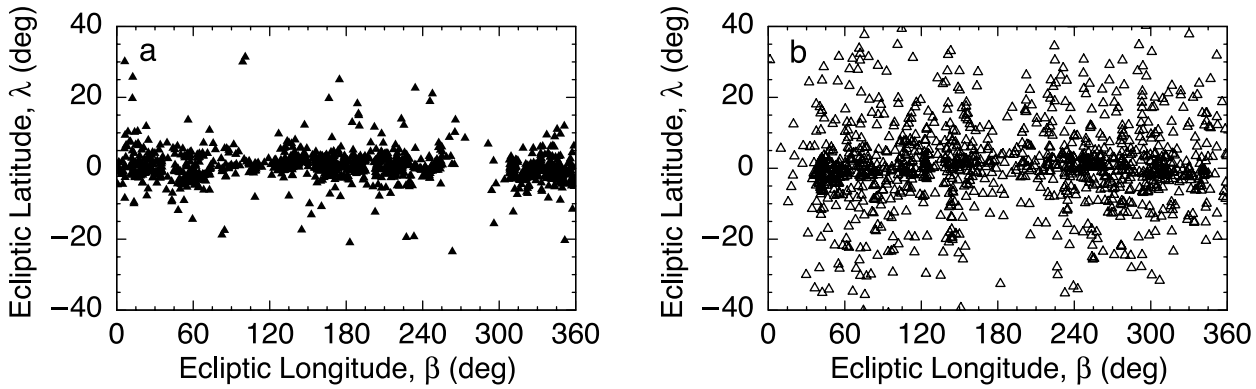

FIG. 8.—KBO positions and velocity directions. (*a*) The positions, in heliocentric ecliptic coordinates, of all MPC KBOs (sample 2.2) at 0000 UT on 2004 April 15. The gap around 270° is due to the extremely high density of stars near the Galactic center, which is avoided by most current KBO surveys. (*b*) The directions of the KBO velocity vectors, also in heliocentric ecliptic coordinates.

recovery observations. The biases that have been quantified for the analyses carried out in this paper are noted in Table 11. Details of how we quantify the effects of these biases will be discussed as needed in later sections.

5. PLANE OF THE KUIPER BELT

A natural reference system for KBO orbits is the mean orbit plane of the Kuiper belt itself, henceforth referred to as the KBP. Observationally, one might define the average plane for a given set of KBOs to be the plane of symmetry of their positions. However, the positions of the cataloged KBOs are not far from their discovery positions, which are biased by the locations of the search fields used in KBO surveys. Brown & Pan (2004) noted that even though the average of the KBO discovery positions is biased, the directions of the KBO velocities can be used to determine the KBP: the average of the KBO sky-plane velocities observed in any patch of sky should be parallel to the KBP. Brown & Pan then proceeded to find the KBP by establishing the plane of symmetry for the directions of the sky-plane velocities at the time of discovery for all the 728 KBOs listed by the MPC on 2003 June 1 (two have since been linked to other objects in the list). In this section we adopt the same basic approach of the velocity symmetry used by Brown & Pan, and we explore five methods for implementing this approach. We also explore solutions for the different subsets of the sample of designated KBOs currently available (Table 4).

5.1. *Methods for Determining the KBP*

Figure 8*a* shows the heliocentric ecliptic coordinates (on 2004 April 15) of the 872 KBOs (sample 2.2) used in our analysis, and Figure 8*b* shows the direction of their velocity vectors, again in ecliptic coordinates (all ecliptic coordinates discussed in this section are heliocentric). To establish the KBP from these velocities, we must determine the plane in the sky about which the velocity directions are symmetric.

We can write the ecliptic latitude, β_0, as a function of ecliptic longitude, λ, for a plane that has an inclination, i, and ascending node, Ω, with respect to the plane of the ecliptic:

$$\beta_0(i, \Omega, \lambda) = \arcsin\left[\sin i \sin(\lambda - \Omega)\right]. \quad (10)$$

For small inclinations this can be approximated by

$$\beta_0(i, \Omega, \lambda) \approx i \sin(\lambda - \Omega). \quad (11)$$

Our task is to determine the parameters i and Ω for the KBP from the direction of the KBO velocity vectors, and we describe five methods that we have used to achieve this goal.

Our first method—that used by Brown & Pan (2004)—establishes the values for i and Ω that minimize the sum of the absolute values of the deviation of all the data in Figure 8*b* from the curve described by equation (11). Brown & Pan prefer this approach over least squares because an underlying assumption of the least-squares method is that the deviations of the data from the model follow a Gaussian distribution—which is not the case for the velocity directions. As can be seen in Figure 8*b*, although these data cluster near the ecliptic, they have too many outliers to be faithfully described by a Gaussian. This can be seen more clearly by collapsing the points in Figure 8*b* into the distribution with ecliptic latitude, as shown in Figure 9*a*. The distribution is strongly peaked on the equator and drops with increasing distance from the central peak—but the tails of the distribution are more suggestive of a power law than a Gaussian. Hence a least-squares fit of equation (11), our second method, does not seem a priori to be the optimum method to establish the KBP, but we include it as a benchmark.

Our third method recognizes that velocity directions of the KBOs are distributed about their average plane as a result of dynamical interactions among themselves and with other bodies. We note that although their average is an unbiased estimate of the average KBP and the velocity of each KBO lies in its (instantaneous) orbit plane, the latitude distribution of the velocity directions does not represent the latitude distribution of KBOs. This is due to the preference for the velocities of KBOs observed in any patch of sky to be parallel to the plane of the Kuiper belt, so that the distribution of velocity directions is biased to those near the KBP. Here we describe the distribution of velocity directions with a function chosen for mathematical convenience.

We simultaneously model the latitude distribution of velocity vectors for the KBOs and the orientation of the KBP relative to the ecliptic (as specified by i and Ω).We define $\beta_{\mathrm{K},v,\mathrm{FWHM}}$ to be the full width at half-maximum of the velocity-direction distribution in Kuiper belt latitude, which we denote by β_{K}, and we then define a dimensionless parameter b as a function of the ecliptic latitude β:

$$b \equiv \left| \frac{2[\beta - \beta_0(i, \Omega, \lambda)]}{\beta_{\mathrm{K},v,\mathrm{FWHM}}} \right|. \quad (12)$$

Also, we define $n_{\mathrm{K},v,0}$ to be the sky density of KBO velocity directions on the Kuiper belt equator for the sample of objects

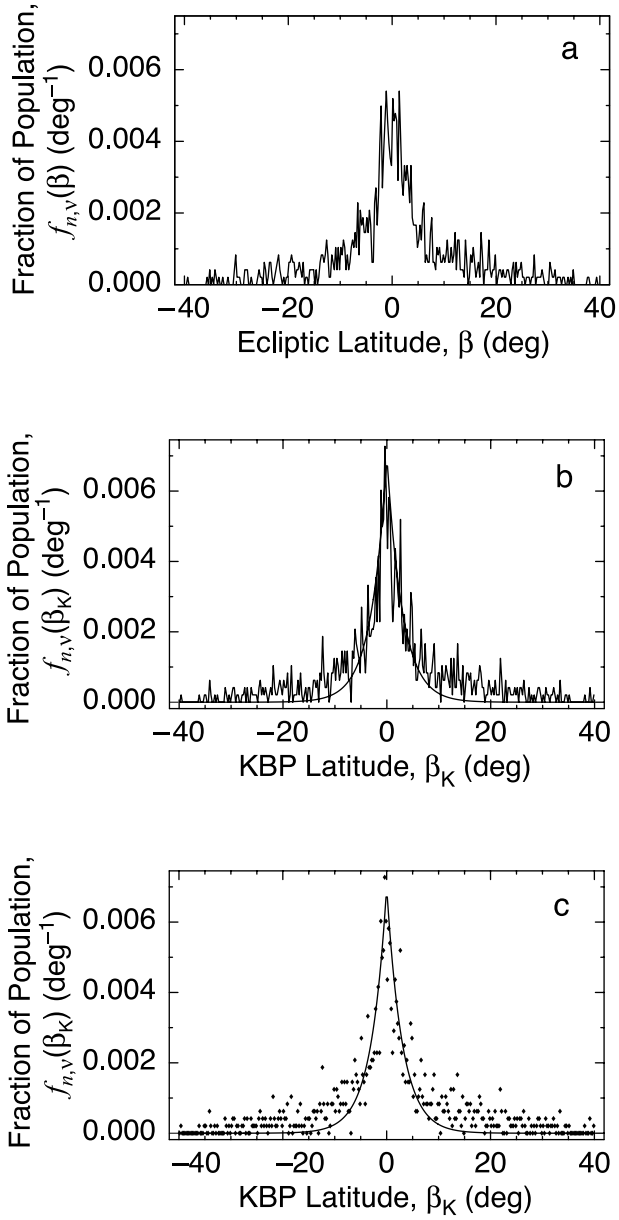

FIG. 9.—Latitude distributions of KBO velocity directions. (*a*) The number of KBO velocity directions (taken from Fig. 8*b*), which have been binned at 0.°5 intervals of ecliptic latitude. (*b*) The velocity directions binned according to their KBP latitudes (as derived in § 5.4). Note that the distribution of data in (*b*) is more sharply peaked than that in (*a*). The solid line represents an exponential fit to match the peak of the data distribution; the data points in (*b*) are displayed unconnected in (*c*) to better show the fit. Note that the tails of the data distribution lie well above the tails of the exponential that matches the peak of the data distribution.

being considered—the peak of the sample. Having no a priori knowledge of the distribution function for the velocity directions of these bodies about their equatorial plane, we try fitting several different functional forms. The most successful—in that it fits the distribution well with the fewest number of free parameters—is an inverse power series in b, with an adjustable coefficient, $c_{j'}$, for each term. Then the sky density of KBO velocity directions, $n_v(\beta)$, is given by

$$n_v(\beta) = n_{\mathrm{K},v,0}\left(1 + c_1 b + \frac{c_2}{2!}b^2 + \frac{c_3}{3!}b^3 + \cdots\right)^{-1}. \quad (13)$$

If all the coefficients $c_{j'}$ were equal to 1 and the series had an arbitrarily large number of terms, it would be the series for e^{-b}. For fitting, we use only a small number of terms and shall hereafter refer to this series as a "truncated exponential" series (similar to the truncated Gaussian series used by Schechter et al. 1993 for fitting point-spread functions to astronomical images). In practice we use $\beta_{\mathrm{K},v,\mathrm{FWHM}}$ as a fitted parameter, which fixes the value of the coefficient c_1 to be

$$c_1 = 1 - \left(\frac{c_2}{2!} + \frac{c_3}{3!} + \cdots\right). \quad (14)$$

In summary, the fitted parameters of our model are i, Ω, $n_{\mathrm{K},v,0}$, $\beta_{\mathrm{K},v,\mathrm{FWHM}}$, and an appropriate number of coefficients $c_{j'}$ ($j' \geq 2$). The velocity directions for the sample of KBOs being considered are divided into bins of ecliptic latitude and longitude, and the model just described is fitted to the binned data by least squares.

The fourth method we used to determine the KBP is also based on this model, but instead of fitting the model by least squares, we find the set of parameters (i, Ω, $n_{\mathrm{K},v,0}$, $\beta_{\mathrm{K},v,\mathrm{FWHM}}$, $c_{j'}$) that yields the maximum likelihood (Bevington & Robinson 2003) for the sample of KBOs being considered. The formal error in each parameter is set at the value for which the likelihood has dropped by a factor of $e^{-1/2}$ from its maximum value, which is equivalent to the formal error in a least-squares fit if the noise were rigorously Gaussian.

The fifth method uses the maximum likelihood technique as well, but we do not bin the velocity directions. Instead we simply compute the likelihood of the ensemble as the product of the likelihoods for each object in the sample. The probability density function used to establish the individual likelihoods is given by

$$p_{v,\beta}(\beta) = \begin{cases} \dfrac{n_v(\beta)}{\int_{\beta_{\min}}^{\beta_{\max}} n_v(\beta)d\beta}, & \text{if } \beta_{\min} \leq \beta \leq \beta_{\max}, \\ 0, & \text{otherwise}, \end{cases} \quad (15)$$

where the interval from $\beta_{\min}$ to $\beta_{\max}$ represents the range of the ecliptic latitudes of the velocity directions being considered and $n_v(\beta)$ is given by equation (13).

5.2. *Implementation*

We use all five methods described in the previous section to determine the KBP, and we compare these with the results of Brown & Pan (2004) that are given in the first row of Table 12. These analyses were based on a sample of 726 objects (sample 2.1.1), which is identical to the 728-object sample (sample 2.1) used by Brown & Pan, except for two objects that were subsequently linked to two other objects in their sample. One difference between our work and the Brown & Pan analysis is that they used the sky-plane velocities reported at discovery and here we have used three-dimensional velocities on 2004 April 15, based on orbital elements available on that date. Also, in some cases we have eliminated a few of the objects (as noted by sample 2.1.1.1) with the largest ecliptic latitudes in order to keep the computation times tractable for the analyses with binned data. Details of our implementation for each of the five methods that we used to determine the KBP are described in the following subsections.

5.2.1. *Minimize the Sum of the Absolute Values of the Residuals*

The parameters of equation (11) were adjusted to minimize the sum of the absolute values of the differences between the

TABLE 12

COMPARISON OF METHODS FOR DETERMINING THE KUIPER BELT PLANE

			Fitted Parameters					Derived Parameters		
Fit	Analysis Method	Sample[a]	Inclination, i (deg)	Node, Ω (deg)	$\beta_{K,v,FWHM}$ (deg)	Peak, $n_{K,v,0}$ (deg^{-2})	c_2	c_1	R.A., α_p (J2000, deg)	Decl., δ_p (J2000, deg)
0.....	BP2004[b]	2.1	1.86	81.6	...	...	...	...	274.57 ± 0.91	66.22 ± 0.37
1.....	MAVR[b]	2.1.1	1.86	98.80	...	...	...	...	274.67 ± 0.47	66.78 ± 0.19
2.....	LS 1D[c]	2.1.1	2.49 ± 0.62	104.0 ± 12.0	...	...	...	...	276.21 ± 1.60	67.04 ± 0.52
3.....	LS 2DB[d]	2.1.1.1	1.65 ± 0.17	97.4 ± 5.7	2.6 ± 0.5	3.0 ± 0.4	0.18 ± 0.08	0.91 ± 0.04	274.14 ± 0.42	66.72 ± 0.16
4.....	ML 2DB[e]	2.1.1.1	1.70 ± 0.18	100.0 ± 6.0	2.6 ± 0.2	3.0 ± 0.2	0.17	0.91	274.25 ± 0.45	66.80 ± 0.18
5[f].....	**ML 2DU**[g]	**2.1.1**	**1.74 ± 0.23**	**99.2 ± 6.6**	**4.0 ± 0.5**	...	**0.44 ± 0.15**	**0.78 ± 0.08**	**274.36 ± 0.60**	**66.78 ± 0.20**

[a] See Table 4.
[b] Minimize sum of absolute values of the residuals (§ 5.2.1).
[c] Least-squares fit for the plane only (§ 5.2.2).
[d] Least-squares fit for the plane and velocity-direction distribution function (binned; § 5.2.3).
[e] Maximum likelihood fit for the plane and velocity-direction distribution function (binned; § 5.2.4).
[f] Adopted solution.
[g] Maximum likelihood fit for the plane and velocity-direction distribution function (unbinned; § 5.2.5).

latitudes of the velocity direction in Figure 8*b* and the model. All 726 unique objects (sample 2.1.1) were used, and the results are listed in the second row of Table 12, along with the right ascension and declination of the KBP pole derived from the fitted inclination and node.

5.2.2. *Least-Squares Fit for the Plane Only*

For this method, the model of equation (11) is fitted to the latitudes of the velocity directions in Figure 8*b* by (nonlinear) least squares, and iterations continue until each parameter changes by less than 0.01 of its formal error. The results are presented in the third row (fit 2) of Table 12. Significantly lower formal errors can be attained by dropping outliers in successive steps and terminating this process when the formal errors in the parameters begin to increase as a result of the smaller number of points. Interpreting the results of this data-elimination approach is not straightforward, however, and we have therefore not included them in Table 12.

5.2.3. *Least-Squares Fit for the Plane and the Velocity-Direction Distribution Function*

Our procedure for simultaneous fitting of the KBP and velocity-direction distribution function in KBP latitude calls for binning the velocity directions into a set of rectangular bins, each measuring 10° of ecliptic longitude by $0.^\circ5$ of ecliptic latitude. These bins cover all ecliptic longitudes, but the central ecliptic latitudes extend only between $\pm 40^\circ$ (for a total of 5796 bins). The model value for the number of objects in each bin is calculated as the value for the central longitude, but the model is integrated over the ecliptic latitude, β. In the fit, each bin is weighted inversely proportionally to the model value for the number of objects in that bin. The weighting is updated with each least-squares iteration, and iterations continue until the parameters change by less than 0.01 of their formal error.

The results of the binned fits are given as fit 3 in Table 12. The parameters i, Ω, $n_{K,v,0}$, $\beta_{K,v,FWHM}$ and c_2 are fitted, while c_1 and the coordinates of the pole have been calculated from the fitted parameters.

5.2.4. *Maximum Likelihood Fit for the Plane and Velocity-Direction Distribution Function: Binned*

We use maximum likelihood analysis in two ways. The first is to apply it to the binned data that we fitted with least squares, as described in the previous section. In the binned method, a grid of parameter values for i, Ω, $\beta_{K,v,FWHM}$, $n_{K,v,0}$, and c_2 is created, with the central value for each parameter set to the least-squares fit value for each. The grid for each parameter encompassed ± 1.5 formal errors from the least-squares fit. We calculate the likelihood for each bin with the binomial distribution, using the total number of objects in the sample, the actual number of objects in the bin, and the mean for the bin given by equation (13) as the parameters for this distribution. The likelihood for each point on the parameter grid is then calculated as the product of the probabilities for the bins. The set of parameter values for the maximum likelihood solution is determined by interpolation of the likelihood grid. The formal error in each parameter is defined as the increment in that parameter required for the likelihood to drop to $e^{-1/2}$ of the maximum likelihood with the other parameters allowed to vary, such that correlations are accounted for in a manner analogous to least squares. The results of our maximum likelihood fit to the binned data is given as fit 4 in Table 12.

5.2.5. *Maximum Likelihood Fit for the Plane and Velocity-Direction Distribution Function: Unbinned*

The second use of the maximum likelihood method is to apply it directly to each object, without binning. For this method we again use a grid of model parameters as described in § 5.2.4, and for each object the likelihood is calculated with the normalized probability function given by equation (15). The product of these is set to be the likelihood for each point on the grid of model parameters; then the model parameters and their formal errors are determined as described in § 5.2.4. Since the number of objects involved is nearly an order of magnitude less than the number of bins, the computation time is considerably less than applying the maximum likelihood method to the binned data. The results are given in the last row (fit 5) of Table 12, and the distribution function from this fit is plotted as the solid line in Figures 9*b* and 9*c*.

5.3. *Comparison of Methods*

The right ascension and declination for the pole of the KBP for each of the methods (given in the last two columns of Table 12 in J2000 coordinates) are plotted in Figure 10 for visual comparison. Values and error bars are similar for all the approaches that we used, except for the least-squares solution

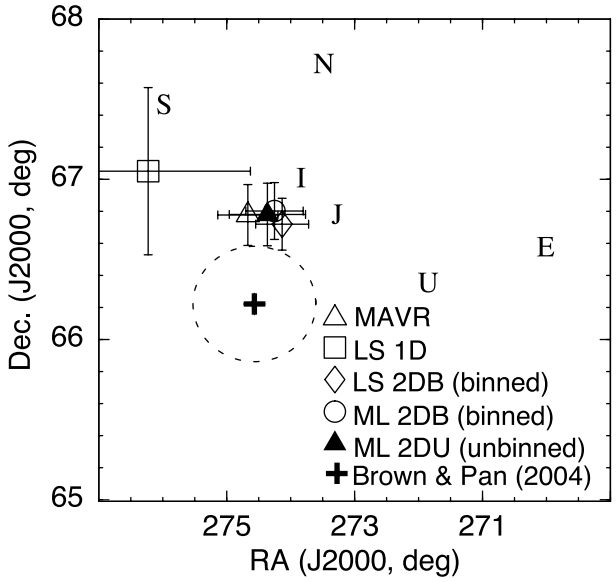

FIG. 10.—Kuiper belt pole positions for different analysis methods. The Kuiper belt pole positions for fits 1–5 in Table 12 are plotted in J2000 coordinates. The poles of the ecliptic (E) and invariable (I) planes are also indicated, as are the orbit poles of Jupiter (J), Saturn (S), Uranus (U), and Neptune (N). We note a cluster of results, just to the lower left of the invariable pole, that includes the three methods that fit both the pole and the distribution of objects about the KBP. These include fits 3–5 in Table 12. Just to the left to this cluster is the open triangle for the method that used the minimum absolute value of the residuals ("MAVR"; fit 1 in Table 12). Since both methods used virtually the same object sample, our MAVR result should agree with the pole position for the KBP derived by Brown & Pan (2004; *plus sign*), tabulated as fit 0 in Table 12. This position is surrounded by a dashed circle that represents their 84.1% confidence limit. We attribute the difference between our result and that derived by Brown & Pan to the fact that they used the object discovery velocities, which would be expected to have larger errors than velocities based on more accurate orbital elements (see § 9.2.1). As expected, the one-dimensional least-squares result ("LS 1D"; *square*) has much larger errors than the other methods. Of the three most precise methods, we have adopted the maximum likelihood unbinned method ("ML 2DU"), since it is the most computationally efficient.

(*square*), which has much larger formal errors than the others. The orbit poles of Jupiter (J), Saturn (S), Neptune (N), Uranus (U), the ecliptic (E), and the invariable plane (I) are also plotted, as is the orbit pole for the Kuiper belt as determined by Brown & Pan (2004). Surrounding their point is a dashed circle that indicates their 84.1% confidence interval. Except for the fact that our error bars represent the standard 68.3% confidence interval for $\pm 1\ \sigma$ for a Gaussian distribution, the Brown & Pan result (Fig. 10, *plus sign*) should be directly comparable to our fit 1 in Table 12 (*open triangle*), since they are based on virtually the same data and we employed their method. However, the two results differ by about $0\overset{\circ}{.}6$ in declination. We attribute the difference to the fact that they used sky-plane velocities reported at discovery, while we used velocities based on current orbital elements. We reserve further discussion of this issue for later (§ 9.2.1).

The results from the other three methods, which derive the KBP in conjunction with the distribution function of the velocity directions, agree well within their formal errors (Fig. 10, *filled triangle, diamond, and circle*). It was anticipated that the least-squares method (*square*) would not give the best results because a fundamental assumption for the least-squares method to yield the optimum solution is violated—the scatter of the velocity directions about their mean plane does not follow a Gaussian distribution. We note that minimizing the sum of the absolute values of the deviations would be optimum only if the velocity directions followed an inverse exponential distribution—however, Figure 9 suggests that this is not the case, since the tails of the distribution appear too high to be well described by an exponential.

Since the maximum likelihood fit to the objects themselves (Fig. 10, *filled triangle*) avoids any bias due to binning of the data, and the computation time for this method is considerably less, we adopt the maximum likelihood method with individual objects as our standard procedure for the remainder of the analyses in this section.

5.4. *Results for the Plane of the Kuiper Belt*

Having established maximum likelihood on unbinned data as our preferred method, we can now continue with our determination of the KBP. In order to use as large an object pool as possible, we begin with the entire database of provisionally designated KBOs and Centaurs from the MPC (sample 2), as they appeared in the Lowell Observatory database on 2004 April 15. From this we select a sample (sample 2.2) that includes all objects (1) with perihelia greater than 5.5 AU that we do not classify as Centaurs (§ 3.2.1), and (2) with solar distance greater than 30.0 AU, if unclassified (§ 3.3). From this pool, we select various samples of objects and determine the mean orbit plane for each. Our results are presented in Table 13. In this table, the first column gives a fit number, and the object samples listed in the second column are cross-referenced to Table 4. In order to limit the objects to those with well-determined orbit planes, we approximate the semimajor axis of the error ellipse for a given object's pole position, σ_p, as the maximum of the standard deviations in the direction of the orbital inclination, σ_i, and node, σ_Ω, as obtained from our orbital solution for each object:

$$\sigma_p = \max(\sigma_i, \sigma_\Omega \sin i). \tag{16}$$

We fit the entire sample of MPC KBOs (fit 1 in Table 13) as a benchmark. Then we limit our sample to those with $\sigma_p < 0\overset{\circ}{.}5$. Note that this criterion reduces the full set of 872 objects to only 565 (fit 2). For the third subset (fit 3) we select Classical objects, and for fit 4 we use only objects in the 3:2 resonances (all those listed in Table 5) with Neptune. The subset for fit 5 contains those objects used in fit 3 that have orbit planes inclined less than 5° from the mean orbit plane. After each iteration for an orbit-plane solution, the subset of objects with inclinations i_K less than 5° is redetermined, and the new subset is used in the next iteration for the orbit plane. For subsets with fewer than 500 objects, we find that the model given by equation (13) tends to have local likelihood maxima because of its ability to generate strong cusps at and near the KBP. For these cases we use a Lorentz function:

$$n_v(\beta) = \frac{n_{K,v,0}}{1 + b^2}. \tag{17}$$

The plane to which orbital elements are referred for distribution analyses is that derived from the Classical objects with low pole errors, fit 5.

Poles for the KBP derived from each of these solutions are plotted in Figure 11. We plot the same comparison points as in Figure 10. The mean pole determined from MPC KBOs (fit 1 in Table 13) is represented by the open triangle, that for all MPC KBOs with pole errors less than $0\overset{\circ}{.}5$ (fit 2) by the square, and that for all MPC Classical KBOs (fit 3) by the filled triangle. These three pole positions are similar.

TABLE 13
THE KUIPER BELT PLANE FOR DIFFERENT SAMPLES OF KBOs

					Fitted Parameters			Derived Parameters		
Fit	Sample Description	Sample[a]	N_{subset}	$\bar{a}_{subset}$ (AU)	i_{subset} (deg)	Ω_{subset} (deg)	$\beta_{K,v,FWHM}$ (deg)	R.A., α_p (J2000, deg)	Decl., δ_p (J2000, deg)	σ_{subset}
1[b]	All MPC KBOs	2.2	872	46.29	1.75 ± 0.19	104.0 ± 5.5	3.1 ± 0.3	274.34 ± 0.50	66.92 ± 0.16	5.55
2[b]	MPC KBOs[c]	2.2.1	565	48.29	1.63 ± 0.23	97.2 ± 6.7	3.5 ± 0.5	274.10 ± 0.58	66.71 ± 0.19	5.41
3	MPC Classical[c]	2.2.1.1	211	43.88	1.51 ± 0.26	100.0 ± 8.8	3.6 ± 0.2	273.77 ± 0.70	66.79 ± 0.22	3.84
4	MPC Resonant[c]	2.2.1.2	66	39.46	2.28 ± 0.78	109.0 ± 11.0	3.0 ± 0.2	275.56 ± 1.80	67.21 ± 0.53	6.32
5[d]	**MPC Classical**[c, e]	**2.2.1.1.1**	**170**	**43.81**	**1.56 ± 0.24**	**96.7 ± 7.4**	**3.1 ± 0.3**	**273.92 ± 0.62**	**66.70 ± 0.20**	**3.15**
6	MPC Classical[c, e, f]	2.2.1.1.1.1	85	44.97	1.62 ± 0.34	97.4 ± 10.0	3.0 ± 0.4	274.07 ± 0.90	66.72 ± 0.29	3.18
7	MPC Classical[c, e, g]	2.2.1.1.1.2	85	42.65	1.58 ± 0.37	98.1 ± 11.0	3.4 ± 0.5	273.95 ± 0.95	66.73 ± 0.30	3.37

[a] See Table 4.
[b] In fits 1 and 2, the parameter c_2 was fitted, yielding the values 0.21 ± 0.07 and 0.55 ± 0.20, respectively. The corresponding, calculated values of c_1 for these two fits are 0.90 ± 0.04 and 0.73 ± 0.10.
[c] With $\sigma_p < 0.^\circ5$.
[d] Adopted solution.
[e] With $i_K < 5^\circ$.
[f] With $a < 44.01$ AU.
[g] With $a > 44.01$ AU.

Our solution for the MPC Classical KBOs is also plotted in Figure 12 (*filled triangle*), along with a line that shows the position of the normal to the Laplacian surface (as a function of semimajor axis) for massless particles in orbits of low eccentricity and inclination, according to the dynamical theory of Brouwer & van Woerkom (1950, hereafter BvW). For a modern transcription of this theory, see chapter 7 of Murray & Dermott (1999), but note that subscripts *i* and *j* in the captions for their Tables 7.2 and 7.3 should be switched; see Chiang (2002) for more information. The BvW theory is a purely secular theory for the motions of the planets in our solar system that is valid to second order in the eccentricities and inclinations of their orbits. It also accounts for the near 5:2 commensurability between the orbits of Jupiter and Saturn.

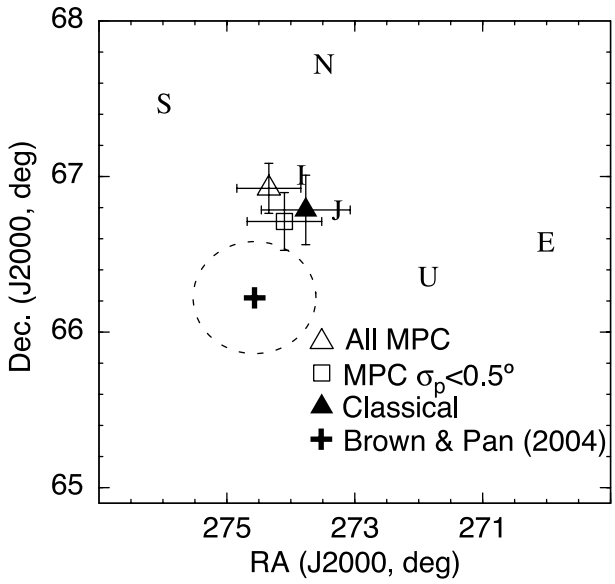

FIG. 11.—Kuiper belt pole positions for different samples of objects. The Kuiper belt pole positions for fits 1–3 in Table 13 are plotted in J2000 coordinates. The poles of the ecliptic (E) and invariable (I) planes are also indicated, as are the orbit poles of Jupiter (J), Saturn (S), Uranus (U), and Neptune (N). The open triangle corresponds to all MPC KBOs (sample 2.2), the square to all MPC KBOs with pole errors less than $0.^\circ5$ (sample 2.2.1), and the filled triangle to all MPC KBOs with pole errors less than $0.^\circ5$ that have been dynamically classified as Classical (according to the classification procedure discussed in § 3.2.4; sample 2.2.1.1). All three object samples give similar results, which lie near the invariable plane. For reference, the plus sign surrounded by an 84.1% confidence dashed circle is the pole position for the KBP derived by Brown & Pan (2004).

All the pole positions that we have derived appear to be more consistent with the pole of the invariable plane than the BvW model. As can be seen in Table 13, the mean semimajor axis for the sample of objects used in fit 3 is 43.88 AU, from which the fitted pole (Fig. 12, *filled triangle*) differs by 2.2 σ from the BvW model. Taken at face value for Gaussian errors, the probability is ~0.03 that the measured pole would differ by this much or more from the BvW pole. Thus, our position for the pole suggests that the BvW model does not correctly describe the situation. The pole determined for the more restricted set of objects used in fit 5 is virtually identical to that in fit 3, which demonstrates the robustness of the result. We choose fit 5 as our adopted solution, since it has the lowest standard error of the fits in Table 13.

To explore the applicability of the BvW model further, we looked for the trend of pole position with semimajor axis as the BvW model predicts. To achieve the greatest statistical accuracy for the comparison, we divided our sample from fit 5 into two equal subsets. The results for finding the KBP determined by these two subsets are given as fits 6 and 7 in Table 13 and plotted in Figure 12. The errors on these two pole positions are larger, as a result of the smaller number of objects in each sample. The sample used in fit 6 has a mean semimajor axis of 44.97 AU, and the sample used in fit 7 has a mean semimajor axis of 42.65 AU. No trend in the positions of the two poles in the direction predicted by the BvW model is evident. Although the result of fit 6 (*diamond*) lies only 0.3 σ from the BvW position, the result of fit 7 (*open triangle*) lies 2.7 σ from the position predicted by the BvW model. The formal probability of the BvW model's correctly describing the pole for the objects used in fit 7 is only ~0.01.

6. PROVISIONAL MAGNITUDE DISTRIBUTION

Having established a general procedure for removing biases connected with the objects and search fields, we now proceed to use this method for deriving the magnitude distribution. Derivation of this distribution requires only that we write equations

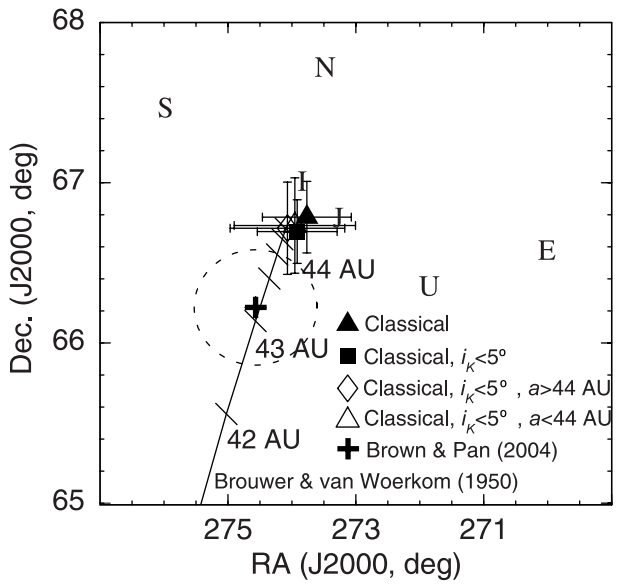

FIG. 12.—Kuiper belt pole positions for different semimajor axes compared with BvW theory. The Kuiper belt pole positions for fits 3 and 5–7 in Table 13 are plotted in J2000 coordinates. The poles of the ecliptic (E) and invariable plane (I) are also indicated, as are the orbit poles of Jupiter (J), Saturn (S), Uranus (U), and Neptune (N). The solid line running from the lower left to the invariable pole is the locus for the pole of the Laplacian surface, as calculated from the theory of Brouwer & van Woerkom (1950). The filled triangle corresponds to all MPC KBOs (sample 2.2.1.1), which have a mean semimajor axis of 43.88 AU. The filled square corresponds to all MPC KBOs with pole errors less than 0°.5 and orbital inclinations with respect to the KBP less than 5° that have been dynamically classified as Classical (sample 2.2.1.1.1). These have a mean semimajor axis of 43.81 AU. This sample has been divided into two equal sets (samples 2.2.1.1.1.1 and 2.2.1.1.1.2), which have mean semimajor axes of 44.97 and 42.65 AU, respectively. These have been plotted with an open diamond and triangle, respectively. The two object samples show no significant difference and are more consistent with the invariable pole than with the pole of the Laplacian surface from the BvW theory. For reference, the plus sign surrounded by an 84.1% confidence dashed circle is the pole position for the KBP derived by Brown & Pan (2004). As discussed in the text (§ 9.2.1), we do not believe that the BvW theory applies to the situation, and we believe our results to be more accurate than those of Brown & Pan (2004).

for the likelihoods, $\zeta_{j,k}$, needed to evaluate equation (2); the other steps follow the general procedure described in § 4.1. The magnitude distribution established here will be "provisional," so termed because we expect to have an improved photometric calibration of our data in the future (as described in §§ 2.2.2 and 9.6.1).

6.1. *Assumptions*

We consider an ideal case for which the sky is surveyed within a certain wavelength band, for which we define a magnitude system and denote the magnitudes by m. We select a survey data set of N_0 objects ($j = 1, \ldots, N_0$) discovered in a set of N_F search fields ($k = 1, \ldots, N_F$). These objects are assumed to be homogenous in their latitude and magnitude distributions. We make further assumptions about the objects in this set: (1) the albedo of a body does not depend on its size, (2) all bodies have the same color, and (3) their distribution in orbital longitude is uniform. For this homogeneous set we define the distribution function in magnitude and latitude (relative to the mean KBP, as determined in § 5) to be $\Sigma(m, \beta_K)$, such that $\Sigma(m, \beta_K)dm$ is the average number of objects (at opposition) observed per square degree at KBP latitude β_K, within a magnitude range dm.

From our assumptions it follows that we can write $\Sigma(m, \beta_K)$ as a product of two functions: (1) a surface-density function, $\Sigma(m, 0)$, which is the number of bodies in the mean orbit plane, per unit magnitude interval, per square degree, and (2) a relative surface-density function $\rho_{\rm lat}(\beta_K)$, which is the relative surface density of objects as a function of latitude, normalized to unity at $\beta_K = 0$:

$$\Sigma(m, \beta_K) = \Sigma(m, 0)\rho_{\rm lat}(\beta_K). \tag{18}$$

Since the functions $\Sigma(m, 0)$ and $\rho_{\rm lat}(\beta_K)$ appear as a product, knowledge of one is needed to remove its bias in the search fields in order to determine the other, and vice versa. In practice, however, if one is willing to make the assumption that the limiting magnitudes of the search fields are not correlated with β_K, then the magnitude distribution can be determined first, followed by the latitude distribution.

6.2. *Procedure*

Each of the N_F fields of the survey data set has a magnitude for which the detection efficiency has dropped to $\frac{1}{2}$, which we denote by $m_{1/2,k}$ for the kth field. If $\epsilon_{\rm max}$ is the maximum efficiency at bright magnitudes and σ_m is a parameter that specifies a characteristic range over which the survey efficiency drops from $\epsilon_{\rm max}$ to 0, we describe the detection efficiency as a function of magnitude, $\epsilon(m, m_{1/2,k})$, with the functional form used by Trujillo et al. (2001):

$$\epsilon(m, m_{1/2,k}) = \frac{\epsilon_{\rm max}}{2}\left[1 + \tanh\left(\frac{m_{1/2,k} - m}{\sigma_m}\right)\right]. \tag{19}$$

We have included $m_{1/2,k}$ as an explicit argument for $\epsilon(m, m_{1/2,k})$, since it has different values for different survey fields, while $\epsilon_{\rm max}$ and σ_m should be the same for all survey fields. We express $m_{1/2,k}$ relative to $m_{2\sigma,k}$, which is the magnitude of an object whose peak pixel is two standard deviations of the background (above the mean background) for the shallower exposure for a pair of search frames. We assume that the difference between $m_{1/2,k}$ and $m_{2\sigma,k}$ is a constant offset, $\Delta m_{1/2-2\sigma}$, that applies to all search frames:

$$m_{1/2,k} = m_{2\sigma,k} - \Delta m_{1/2-2\sigma}. \tag{20}$$

Each frame of our survey fields has the same solid angle, Ω_s, of sky exposure. However, some of this solid angle is obscured by the presence of other objects. Furthermore, the two frames of the pair have their centers offset, and this misregistration results in an additional loss of solid angle. If the sum of these two losses for the kth survey field is $\Delta\Omega_k$, then the net solid angle for the kth search field, Ω_k, is

$$\Omega_k = \Omega_s - \Delta\Omega_k. \tag{21}$$

We define the average latitude-density factor, $\xi_{{\rm lat},k}$, to be an average of $\rho_{\rm lat}(\beta_K)$ (over solid angle) for a search field centered on $\beta_K = \beta_{K,k}$:

$$\xi_{{\rm lat},k} = \frac{1}{\Omega_k}\int_{\lambda_{K,\,{\rm min},k}}^{\lambda_{K,\,{\rm max},k}}\int_{\beta_{K,\,{\rm min},k}}^{\beta_{K,\,{\rm max},k}} \rho_{\rm lat}(\beta'_K)\cos\beta'_K\, d\beta'_K\, d\lambda'_K, \tag{22}$$

where $\lambda_{K,\min,k}$, $\lambda_{K,\max,k}$, $\beta_{K,\min,k}$, and $\beta_{K,\max,k}$ are respectively the minimum and maximum KBP longitudes and latitudes on the frame. The solid angle normalizing factors are

$$\xi_{\mathrm{ang},\,k} = \Omega_k/\Omega_s. \tag{23}$$

The likelihood factors for the magnitude distribution for the jth object on the kth frame are the product of these relative probabilities and the detection efficiency:

$$\zeta_{\mathrm{MAG},j,k} = \xi_{\mathrm{lat},k}\xi_{\mathrm{ang},k}\epsilon(m_j, m_{1/2,k}). \tag{24}$$

6.3. *Empirical Distribution*

We can now determine the empirical magnitude distribution for the DES KBOs with the procedure described in § 4. The first step in this process is to establish the magnitude distribution of the detected objects, without yet including the latitude bias factor, $\xi_{\mathrm{lat},k}$, or the detection efficiency, $\epsilon(m, m_{1/2,k})$. We do not include the latitude bias factor because the latitude and magnitude distributions for the population are intertwined and must be determined by successive approximation. Since most of our data were recorded in the *VR* filter, we construct the empirical magnitude distribution with this sample (sample 1.3.1). The magnitude bins range from 20 to 25 in 0.2 mag increments, and we approximate $\xi_{\mathrm{lat},k} = 1.0$ for all β_k. In this, and all the analyses discussed in this paper involving the removal of observational biases, we treat each of the eight detectors in the Mosaic cameras as a distinct search field, with its own bias factor.

The resulting empirical distribution for objects observed in the *VR* filter is shown as the filled points with error bars in Figure 13*a*. Beginning at the bright end, the numbers rise sharply because of the greater number of KBOs at fainter magnitudes, peaking between magnitudes 22 and 23. For fainter magnitudes, the number of objects drops because of the decreasing sensitivity of the survey.

6.4. *Single Power-Law Fit*

We denote the sky density of KBOs brighter than magnitude m at KBP latitude β_K by $\Sigma(<m, \beta_K)$. This integral magnitude distribution has also been termed the "luminosity function" (e.g., Jewitt et al. 1998), which can be defined with two parameters: m_0, the magnitude for which the sky density of objects brighter than m_0 is 1 per square degree (at opposition and for $\beta_K = 0$), and α, the logarithmic slope of the distribution. On the KBP equator, this can be written as

$$\Sigma(<m, 0) = 10^{\alpha\,(m-m_0)}. \tag{25}$$

The differential magnitude distribution, $\Sigma(m, 0)$, is then found by differentiating equation (25) with respect to m:

$$\Sigma(m, 0) = (\alpha \ln 10)10^{\alpha\,(m-m_0)}. \tag{26}$$

We also define $\Omega_{N_F,0}(m)$ as the equivalent solid angle at $\beta_K = 0$ covered by the N_F fields of the survey. In terms of previously defined quantities, this can be written

$$\Omega_{N_F,0}(m) = \sum_{k=1}^{N_F} \epsilon(m, m_{1/2,k})\Omega_k\xi_{\mathrm{lat},k}. \tag{27}$$

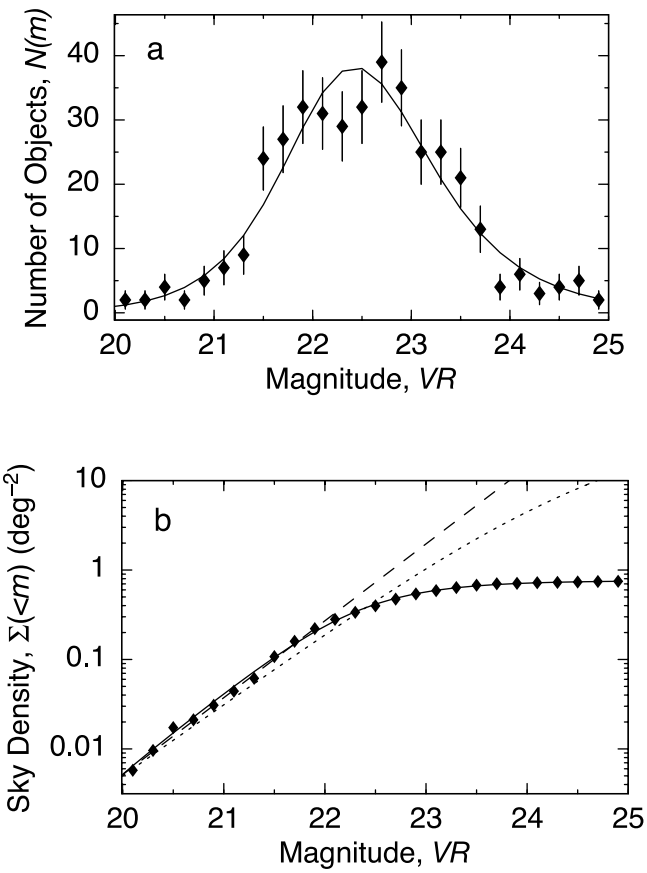

FIG. 13.—Provisional KBO magnitude distribution. (*a*) The number of KBOs discovered by the DES in a *VR* filter (sample 1.3.1), binned at 0.2 mag. Hence each point represents $N(m, \Delta m)$ given by eq. (28), with $\Delta m = 0.2$. The solid line is the model fit of eq. (28) to these data, which describes the KBO magnitude distribution as a single power law and describes the sensitivity function for the DES frames by the function given in eq. (19). The rise of the curve at the bright end is due to the increasing number of KBOs at fainter magnitudes, while the drop on the faint end is due to the decreasing sensitivity of the survey at fainter magnitudes. The apparent discontinuity at 21.5 mag is not statistically significant, according to a K-S test. (*b*) The solid line shows our provisional integral magnitude distribution of KBOs (luminosity function) that corresponds to the model fit displayed in (*a*). The dashed line corresponds to the fitted power-law component (only) for KBO magnitude model, and the dotted line corresponds to the dual power-law distribution from Bernstein et al. (2004). Although the results are similar at the magnitudes where the DES is sensitive, the DES distribution indicates a somewhat higher sky density and steeper power law than Bernstein et al. (2004).

With these definitions, the number, $N(m, \Delta m)$, of objects detected by the survey in a given bin of magnitude width Δm is given by

$$N(m, \Delta m) = \Delta m\Omega_{N_F,0}(m)\Sigma(m, 0). \tag{28}$$

We perform least-squares fits of the model function $N(m, \Delta m)$ to the DES data shown in Figure 13*a*. The free parameters of the fit fall into two categories: (1) α and m_0, which describe the magnitude distribution, and (2) σ_m and $\Delta m_{1/2-2\sigma}$, which describe the sensitivity of the survey as given by equations (19) and (20). The parameter $\epsilon_{\max}$ is fixed at 1.0. Between each iteration of the least-squares fit, the equivalent solid angle at zero KBP latitude, $\Omega_{N_F,0}(m)$, is recalculated, as required to update the model function in equation (28).

Model fits were performed for different samples of KBOs, and the results are given in Table 14. Fit 1 includes all KBOs discovered by the DES, irrespective of the filter used or

TABLE 14
Fits for the Magnitude Distribution

Fit (1)	DES Sample[a] (2)	Sample[b] (3)	Objects (4)	Offset, $\Delta m_{1/2-2\sigma}$ (mag) (5)	σ_m (mag) (6)	Exponent, α (7)	m_0 (mag) (8)
1	All KBOs	1.3	512	1.34 ± 0.12	0.58 ± 0.03	0.88 ± 0.08	22.70 ± 0.10
2[c]	**All *VR* KBOs**	**1.3.1**	**393**	**1.43 ± 0.15**	**0.58 ± 0.03**	**0.86 ± 0.10**	**22.70 ± 0.13**
3	Designated KBOs	1.3.2	339	1.33 ± 0.14	0.49 ± 0.03	0.85 ± 0.10	22.80 ± 0.14
4	Designated *VR* KBOs	1.3.2.1	270	1.52 ± 0.16	0.52 ± 0.03	0.88 ± 0.12	22.70 ± 0.15
5	Classical *VR* KBOs	1.3.2.1.1	59	1.25 ± 0.26	0.49 ± 0.06	0.72 ± 0.17	23.90 ± 0.48
6	Classical *VR* KBOs	1.3.2.1.1	59	1.43[d]	0.58[d]	0.74 ± 0.05	23.70 ± 0.08
7	Excited *VR* KBOs	1.3.2.1.2	59	1.80 ± 0.58	0.62 ± 0.12	0.72 ± 0.29	23.40 ± 0.94
8	Excited *VR* KBOs	1.3.2.1.2	59	1.43[d]	0.58[d]	0.58 ± 0.09	24.00 ± 0.24
9	Resonant *VR* KBOs	1.3.2.1.3	41	1.65 ± 0.54	0.58 ± 0.13	0.60 ± 0.29	24.00 ± 1.21
10	Resonant *VR* KBOs	1.3.2.1.3	41	1.43[d]	0.58[d]	0.52 ± 0.08	24.40 ± 0.30
11	Scattered *VR* KBOs	1.3.2.1.4	18	2.39 ± 0.71	0.51 ± 0.26	1.29 ± 0.94	22.88 ± 1.40
12	Scattered *VR* KBOs	1.3.2.1.4	18	1.43[d]	0.58[d]	0.74 ± 0.15	24.40 ± 0.33

[a] All of these samples include only objects discovered by the DES, and none of them includes Centaurs or unclassified objects at heliocentric distances less than 30 AU.
[b] See Table 4.
[c] Adopted solution.
[d] Fixed parameter in the least-squares fit.

whether the objects are designated. Fit 2 (boldface) includes all objects discovered by the DES in a *VR* filter. This model—displayed as the solid line in Figure 13*a*—should match the data points. Fits 3 and 4 in Table 14 are the same as fits 1 and 2, respectively, but with only designated objects.

Given the differences in object samples used in the first four fits, the results (cols. [5]–[8] of Table 14) are remarkably similar. Columns (5) and (6) of Table 14 give the fitted offset magnitude and transition width for the detection efficiency function. Although we determined the two parameters for our detection efficiency function in Paper I (see Fig. 4 of Paper I), this earlier estimate was based on a limited amount of synthetic data, and here we have the benefit of using a much larger data set to establish these parameters directly from fitting the actual data. Hence we consider fit 2 to be our best provisional *VR* magnitude distribution for the entire KBO population.

Next we consider the magnitude distributions for different dynamical classes—Classical, Resonant, and Scattered objects discovered in the *VR* filter—which are described by the next eight fits in Table 14. Following Bernstein et al. (2004), we define "Excited" as simply the combination of the Scattered and Resonant classes. Since the number of objects in these samples is low, one fit for each of these dynamical classes has fixed parameters for the detection efficiency function at the values determined in fit 4 (all designated *VR* objects). The four cases with the fixed parameters will be the most reliable for intercomparison of the parameters describing the population distribution, α and m_0.

Returning to Figure 13, the dashed line in Figure 13*b* shows the single power-law model for our preferred fit parameters for the entire KBO population (fit 2 in Table 14). The solid line (the fitted model) shows the integral of the distribution of the sky density of KBOs folded in with the detection efficiency of the DES versus magnitude, and the points indicate the integral distribution of the objects detected by the DES. To the extent that the actual integral distribution of KBOs follows the fitted power law, the difference between the dashed and solid lines on the logarithmic scale gives the efficiency of the DES. At *VR* magnitude of approximately 22.5, the solid line falls below the dashed line by 0.3 on the logarithmic scale, indicating the half-efficiency magnitude. For comparison, the double power-law model of Bernstein et al. (2004) has been plotted as the dotted line. Comparisons of our provisional magnitude distribution with Bernstein et al. (2004) and other work appear in § 9.4. Current work for calibration of the photometry is discussed in § 9.6.1, and calibration of the detection efficiency is discussed in § 9.6.2.

7. LATITUDE DISTRIBUTION

Next we consider the distribution of KBOs as a function of latitude relative to the KBP derived in § 5.4. The approach presented in this section is to establish the latitude distribution by taking a census of the latitudes of the DES objects at their discovery locations and applying the bias-removal technique described in § 4. Later (in § 8.3) we shall infer the latitude distribution from the inclination distribution.

We choose a set of N_n latitude bins over which we have search coverage. The correction of the observational biases for objects discovered in each of these latitude bins requires that we specify the likelihood factors Z_n for the latitude bins. One component of Z_n is the amount of solid angle that each search frame contributes, which we call $\xi_{\mathrm{ang},k,n}$ for the kth search frame. This is analogous to the quantity defined by equation (23) for the magnitude analyses in § 6.2. We define $\beta_{\mathrm{K,min},k,n}$ and $\beta_{\mathrm{K,max},k,n}$ to be the minimum and maximum values of KBP latitude on the kth search frame contained in the latitude range covered by the nth bin. We also define $\lambda_{\mathrm{K,min},k}(\beta_{\mathrm{K}})$ and $\lambda_{\mathrm{K,max},k}(\beta_{\mathrm{K}})$ to be the minimum and maximum values of KBP longitude as a function of KBP latitude on the kth search frame, noting that either of these values may be determined by the boundary of the nth bin passing through the kth search frame (see Appendix B). Then the solid-angle component of the likelihood factor for the kth search frame for the nth bin can be found by integration over the solid angle of the kth search field that is contained in the nth latitude bin and multiplying by the factor used in equation (23) to account for the solid-angle loss due to bright objects and misregistration of the search frames:

$$\xi_{\mathrm{ang},k,n} = \frac{\Omega_k}{\Omega_s} \int_{\beta_{\mathrm{K,min},k,n}}^{\beta_{\mathrm{K,max},k,n}} \int_{\lambda_{\mathrm{K,min},k}(\beta'_{\mathrm{K}})}^{\lambda_{\mathrm{K,max},k}(\beta'_{\mathrm{K}})} \cos\beta'_{\mathrm{K}}\, d\lambda'_{\mathrm{K}}\, d\beta'_{\mathrm{K}}. \quad (29)$$

We can simplify equation (29) by noting that the integration over $\lambda'_{\rm K}$ depends only on the difference $\Delta\lambda_{{\rm K},k}(\beta_{\rm K}) = \lambda_{{\rm K},{\rm max},k}(\beta_K) - \lambda_{{\rm K},{\rm min},k}(\beta_{\rm K})$, which is given by equation (B4) in Appendix B:

$$\xi_{{\rm ang},k,n} = \frac{\Omega_k}{\Omega_s} \int_{\beta_{{\rm K},{\rm min},k,n}}^{\beta_{{\rm K},{\rm max},k,n}} \Delta\lambda_{{\rm K},k}(\beta'_{\rm K}) \cos\beta'_{\rm K}\, d\beta'_{\rm K}. \quad (30)$$

We carry out this integration with the aid of equation (B5) in Appendix B, under the assumption that $\cos\beta'_{\rm K}$ does not vary significantly within the kth search frame.

The magnitude component of the likelihood factor for the kth search frame, $\xi_{{\rm mag},k}$, can be found by integrating the product of the magnitude distribution of the population distribution and the detection efficiency over magnitude. We approximate the population distribution as a single power law between $m_{\rm min}$ and $m_{\rm max}$, the minimum and maximum magnitudes of a sample of objects:

$$\xi_{{\rm mag},k} = \alpha \ln 10 \int_{m_{\rm min}}^{m_{\rm max}} 10^{\alpha(m-m_0)} \epsilon(m, m_{1/2,k}) dm. \quad (31)$$

The magnitude component for the nth bin, $\xi_{{\rm mag},k,n}$, is found by integrating over the magnitudes in that bin. Combining the components for magnitude and solid angle in equations (30) and (31), we find the likelihood factor for the kth frame and the nth bin:

$$\zeta_{{\rm LAT},k,n} = \xi_{{\rm mag},k,n}\xi_{{\rm ang},k,n}. \quad (32)$$

Finally, we find the probability factor for the nth bin by summing the likelihood factors that each search frame contributes to the nth bin:

$$\zeta_{{\rm LAT},n} = \sum_{k=1}^{N_F} \zeta_{{\rm LAT},k,n}. \quad (33)$$

Using equation (33) and the bias-removal procedure discussed in § 4, we determine the unbiased latitude distribution, $f_{\beta_{\rm K}}(\beta_{\rm K})$, for all DES KBOs (sample 1.3). A power-law exponent of $\alpha = 0.86$ (fit 2 in Table 14) was employed, and the integral in equation (30) was evaluated with the approximation discussed in Appendix B. A plot of this latitude distribution appears in Figure 14, which is further discussed in § 8.3.

Now that we know both the magnitude and latitude distributions for the KBOs discovered by the DES, we can calculate the effective solid angle versus magnitude for the survey. To do this, we use equation (27), with the detection efficiency parameters determined in fit 2 of Table 14 and the $m_{1/2}$ and σ for each search frame. The result for the DES, through 2003, is displayed as the solid line in Figure 15. The horizontal dashed line indicates the total solid angle on all the DES frames considered. The difference between the lines for bright magnitudes is due to the misregistration of the frame pairs, the presence of bright objects, and exposure fields taken away from the Kuiper belt equator.

8. INCLINATION DISTRIBUTION

In this section we update the inclination distribution that we derived in Paper I, with the addition of the new KBOs reported here. We also derive a latitude distribution from the inclination distribution for comparison with the latitude distribution derived in the previous section.

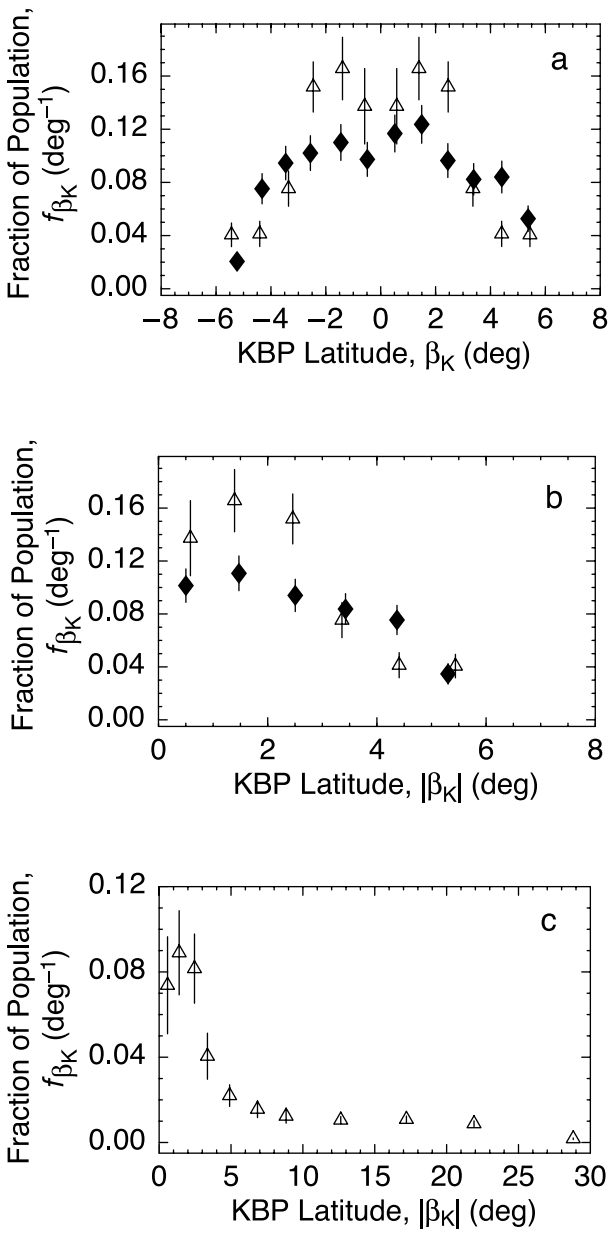

FIG. 14.—Latitude distribution of KBOs from discovery positions and from the inclination distribution. The fraction of objects in the sample is plotted vs. (*a*) KBP latitude and (*b*, *c*) absolute value of KBP latitude. The diamonds represent the latitude distribution found from the object positions, while the triangles represent the distribution obtained using the unbiased inclinations (§ 8.3). The data from object positions are averaged over positive and negative latitudes in (*b*). In (*a*) and (*b*), the inclination distribution is separated into 1° bins and the resulting latitude distribution is normalized from ±6° KBP latitude. In (*c*), the inclination distribution is that from Fig. 16, but extended to much larger inclinations, and the resulting latitude distribution is normalized from ±30° KBP latitude.

8.1. *Bias Removal for Inclinations*

For the inclination bias removal, we refer likelihood factors to those for the detection of a body with $i_{\rm K} = 0°$, in a search field of solid angle of Ω_s, centered on the Kuiper belt equator. To derive the inclination distribution for various subsets of bodies detected by the DES, we must account for likelihood factors relating to (1) field loss due to the offset of centers for the two frames covering the search field, (2) field loss due to

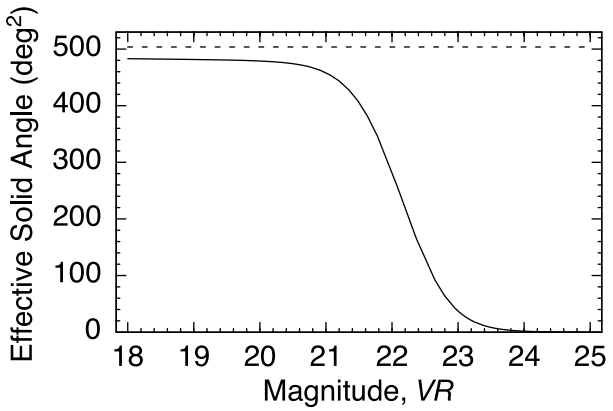

FIG. 15.—Solid-angle coverage for the DES through the end of 2003. The solid line represents the equivalent solid-angle coverage vs. *VR* magnitude, as calculated with eq. (27), and the horizontal dashed line represents the total solid angle of the survey. The difference between the lines for bright magnitudes is due to the misregistration of the frame pairs and the presence of bright objects that obscure KBOs (see § 7).

interfering objects, (3) detection efficiency as a function of the limiting magnitude of the frame, (4) the magnitude distribution of the objects, and (5) geometric biases of detecting more objects with inclinations near the KBP latitude of the search field. For the kth search field, the first two of these effects are combined into the solid-angle likelihood factor, $\xi_{\mathrm{ang},k}$ (given by eq. [23]), the second two into the magnitude likelihood factor, $\xi_{\mathrm{mag},k}$ (given by eq. [31]), and the last effect into the likelihood factor $\xi_{\mathrm{inc},k}$. These likelihood factors have no dependence on bins, since we have assumed that the inclination of a KBO is independent of its magnitude and independent of its KBP longitude.

To compensate for the geometric bias caused by KBOs spending more time at KBP latitudes near their inclination, we use a model based on circular orbits and an assumed barycentric reference point for observation. At latitude β the conditional probability density, $p(i|\beta)$, for finding an object with orbital inclination i is

$$p(i|\beta) = \begin{cases} \dfrac{\sin i}{\pi\sqrt{\sin^2 i - \sin^2\beta}}, & \text{if } \sin i \geq |\sin\beta|, \\ 0, & \text{if } \sin i < |\sin\beta|. \end{cases} \quad (34)$$

The normalization of $p(i|\beta)$ is such that its integral over all inclinations equals 1 for any value of β.

We define $\xi_{\mathrm{inc},k,n}$ as the likelihood factor for detecting objects in the kth search field, with inclinations in the nth bin for i_{K}, where the nth bin spans the inclination range from $i_{\mathrm{K,min},n}$ to $i_{\mathrm{K,max},n}$. We assume that the inclination distribution function for the KBOs varies no more severely than linearly over the nth bin, so that the following equation for $\xi_{\mathrm{inc},k,n}$ is valid:

$$\xi_{\mathrm{inc},k,n} = \int_{i_{\mathrm{K,min},n}}^{i_{\mathrm{K,max},n}} \int_{\beta_{\mathrm{K,min},k}}^{\beta_{\mathrm{K,max},k}} \int_{\lambda_{\mathrm{K,min},k}(\beta'_{\mathrm{K}})}^{\lambda_{\mathrm{K,max},k}(\beta'_{\mathrm{K}})} p(i'_{\mathrm{K}} \mid \beta'_{\mathrm{K}}) \cos\beta'_{\mathrm{K}} \, d\lambda'_{\mathrm{K}} \, d\beta'_{\mathrm{K}} \, di'_{\mathrm{K}}. \quad (35)$$

The integrations are carried out within the limits indicated for the kth search field, noting that the potential full ranges for the variables of integration are $0^\circ \leq i'_{\mathrm{K}} \leq 180^\circ$, $-90^\circ \leq \beta'_{\mathrm{K}} \leq 90^\circ$, and $0^\circ \leq \lambda'_{\mathrm{K}} \leq 360^\circ$. The first step in evaluating the integral, within the approximations discussed in Appendix B, is to note that the integral over λ'_{K} depends only on the interval $\Delta\lambda_{\mathrm{K},k}(\beta'_{\mathrm{K}})$, so that we have

$$\xi_{\mathrm{inc},k,n} = \int_{i_{\mathrm{K,min},n}}^{i_{\mathrm{K,max},n}} \int_{\beta_{\mathrm{K,min},k}}^{\beta_{\mathrm{K,max},k}} p(i'_{\mathrm{K}} \mid \beta'_{\mathrm{K}}) \Delta\lambda_{\mathrm{K},k}(\beta'_{\mathrm{K}}) \cos\beta'_{\mathrm{K}} \, d\beta'_{\mathrm{K}} \, di'_{\mathrm{K}}, \quad (36)$$

where an equation for the interval $\Delta\lambda_{\mathrm{K},k}(\beta'_{\mathrm{K}})$ is given in Appendix B.

The analytic expression for the integral over β'_{K} has different forms, depending on the orbital inclination, i'_{K}. As a function of this quantity, object orbits will either (1) never reach the latitudes of the search field, (2) always be within the latitudes of the search field, (3) have both positive and negative latitudes within the search field, (4) have positive latitudes within the search field and negative latitudes crossing through the search field, (5) have negative latitudes within the search field and positive latitudes crossing through the search field, (6) have both positive and negative latitudes crossing through the search field, (7) peak in the latitudes of the search field, or (8) cross through the latitudes of the search field. The likelihood factors are found by considering each of these cases, accounting for the tilt of the search fields relative to KBP coordinates (Appendix B), and then integrating the conditional probability density for the inclination of each object, $i_{\mathrm{K},j}$, contained in the nth bin over the solid angle covered by the kth search frame. The integrand for i'_k can then be averaged for the sample of objects contained in the nth bin.

Having calculated all the components, we can now write an equation for the inclination likelihood factor for the kth search frame for the nth bin, $\zeta_{\mathrm{INC},k,n}$, as the product of the factors described above:

$$\zeta_{\mathrm{INC},k,n} = \xi_{\mathrm{ang},k}\xi_{\mathrm{mag},k}\xi_{\mathrm{inc},k,n}. \quad (37)$$

Finally, the likelihood factor for the nth bin, $\zeta_{\mathrm{INC},n}$, is found by summing $\zeta_{\mathrm{INC},k,n}$ over all N_F search fields.

8.2. *Calculated Inclination Distribution*

For this distribution, we select designated DES KBOs having errors in inclination, σ_i, less than $0.^\circ5$ (sample 1.3.2.2). The inclinations for these objects are calculated with respect to the KBP (fit 5 in Table 13) and are then divided into 11 bins: one-degree intervals between 0° and 4°, two-degree intervals between 4° and 10°, five-degree intervals between 10° and 25°, and a single 10-degree interval between 25° and 35°. The total inclination distribution, $f_{i_{\mathrm{K}},n}$, is found by substituting these data, along with the likelihoods from equation (37), into equation (7). The results are displayed in Figure 16, with error bars derived from equation (8). The ordinate for Figure 16 is normalized to be the fraction of the population per degree of orbital inclination. Also plotted are the total inclination distribution for comets with periods less than 200 years (*histogram*) and the normalized sin i_{K} distribution, which is expected for objects having poles in random directions (*dashed line*). We have made no attempt to remove the observational selection bias in the comet distribution. In Figure 17, the data from Figure 16 are displayed according to dynamical classification: Classical, Scattered (Near and Extended), Resonant, and unclassified objects (samples 1.3.2.2.1–.4, respectively).

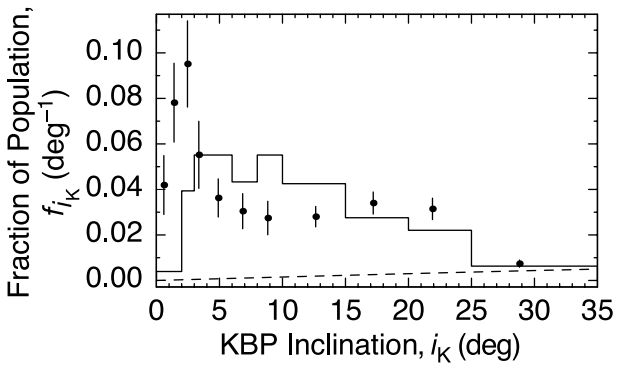

FIG. 16.—The unbiased KBP inclination distribution. The data points represent the fraction of objects in the sample (designated DES KBOs with inclination errors less than 0°.5; sample 1.3.2.2) per degree of inclination, with errors determined from binomial statistics. Bin sizes are one degree from 0° to 4°, two degrees from 4° to 10°, five degrees from 10° to 25°, and a 10-degree bin from 25° to 35°. Each point is plotted at the average inclination for the objects in the bin. For reference, the inclination distribution (biased) of short-period comets (with respect to the KBP) is plotted as a histogram, and the sin i_K inclination distribution, expected from orbits with poles in random directions, is plotted as a dashed line.

The components of the inclination distribution are found by studying Figure 17. The inclination distribution for the Classical objects is double peaked and extends out to approximately 20°. The Resonant objects are fairly evenly distributed, extending out to approximately 25°. The majority of the Scattered objects are found at high inclinations, from approximately 10° to 35°. Thus, as would be expected, the low-inclination peak of Figure 16 is composed primarily of Classical objects while the broader, higher inclination peak is composed of Classical and Resonant objects at lower inclinations (<15°) and Scattered and Resonant objects at higher inclinations.

The KBP inclination distribution divided by sin i_K is shown in Figure 18 and represents the density of KBO orbit poles per square degree. Figures 16 and 18 reveal a "core" of objects at low inclinations and a "halo" of objects at higher inclinations. These populations become particularly apparent in Figure 19,

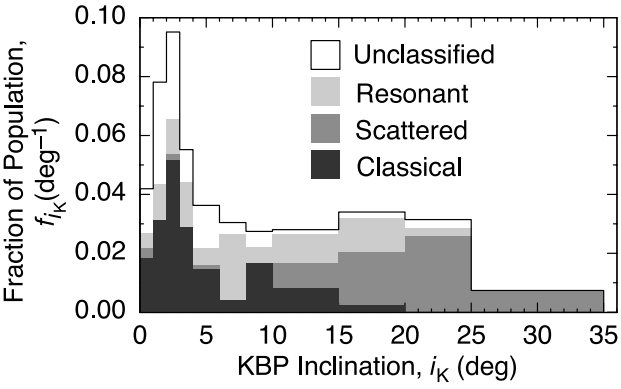

FIG. 17.—The unbiased KBP inclination distribution as a function of KBO classification. The fraction of objects in the sample per degree of inclination is the same as Fig. 16, with each bin shaded to reflect the proportion of objects by classification. Unclassified objects are represented by open areas, Resonant objects are light gray, Scattered (Near and Extended) objects are dark gray, and Classical objects are black. The low-inclination "core" is primarily composed of Classical objects, while the higher inclination "halo" is primarily Scattered objects. Along the KBP inclination axis, the boundary between Classical and Scattered objects is not distinct.

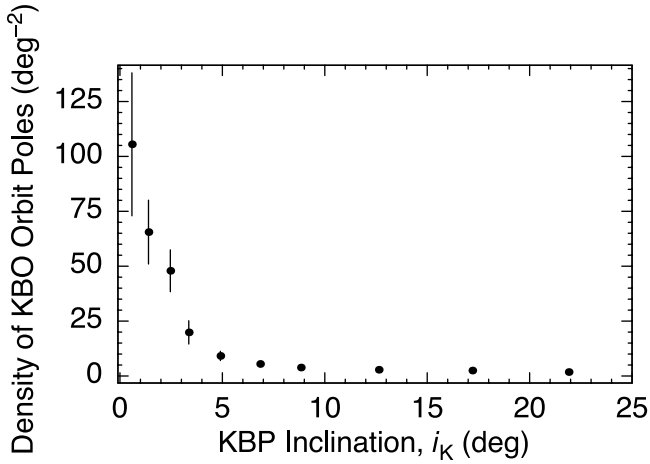

FIG. 18.—KBO pole distribution. The unbiased inclination distribution from Fig. 16 divided by sin i_K, which represents the number of object poles per square degree, is plotted vs. KBP inclination. The peak at low inclinations illustrates the presence of a concentrated core of KBOs.

which shows a concentrated core of KBO orbit poles when plotted in sky coordinates (right ascension and declination). As seen in Figure 18, the FWHM of this core is approximately 2°.3; therefore, we have drawn a circle of diameter 4°.6 in Figure 19 to encompass the orbit poles of these objects.

From Figure 16, we conclude that the KBO population has a total inclination distribution that is broadly similar to that of short-period comets (which contains observational biases)—save for the core population of low-inclination objects. By

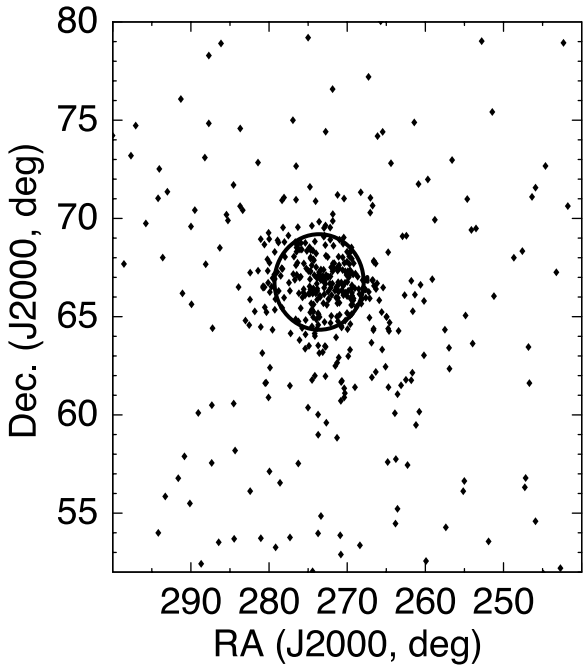

FIG. 19.—Orbit poles for KBOs that have errors in their pole position less than 0°.5 (sample 2.2.1), plotted in right ascension–declination coordinates. Note the cluster of orbit poles, the center of which is the mean orbit pole of the KBP (fit 5 in Table 13). A circle of diameter 4°.6 is plotted that encompasses the core concentration of orbit poles. Surrounding this concentration is a halo with a lower density of orbit poles. The central core may be a dynamical relic of the primordial objects. It is not known, however, if the halo is a tail of the primordial distribution or a distinct population that had a different dynamical origin.

TABLE 15
FITS FOR THE INCLINATION DISTRIBUTION

Model Distribution	Model	$D\sqrt{N}$	Results[a]
Gaussian	Eq. (38)	3.62	$\sigma_1 = 12\overset{\circ}{.}21 \pm 1\overset{\circ}{.}16$
Double Gaussian	Eq. (39)	0.96	$d_1 = 0.94 \pm 0.01$, $\sigma_2 = 1\overset{\circ}{.}94 \pm 0\overset{\circ}{.}19$, $\sigma_3 = 12\overset{\circ}{.}68 \pm 0\overset{\circ}{.}64$
Gaussian plus Lorentzian	Eq. (40)	0.94	$i_{1/2,\mathrm{K}} = 11\overset{\circ}{.}42 \pm 0\overset{\circ}{.}49$, $g = 8.72 \pm 1.51$, $d_2 = 26.93 \pm 4.82$, $\sigma_4 = 2\overset{\circ}{.}15 \pm 0\overset{\circ}{.}15$

[a] These fits represent the fractional inclination distribution and are not normalized to the number of objects in the sample. They can be normalized by dividing by the integral of the distribution from 0° to 180°.

contrast, the KBO distribution of inclinations bears no resemblance to that of an isotropic distribution. To explore the functional form of the distribution, we perform weighted least-squares fits to the data using three different models. The first model tested is a Gaussian multiplied by sin i_{K}:

$$f_{i_{\mathrm{K}}}(i_{\mathrm{K}}) = \exp\left(\frac{-i_{\mathrm{K}}^2}{2\sigma_1^2}\right)\sin i_{\mathrm{K}}. \quad (38)$$

The second model follows that of Brown (2001) and Trujillo et al. (2001); it consists of two Gaussians multiplied by sin i_{K}:

$$f_{i_{\mathrm{K}}}(i_{\mathrm{K}}) = \left[d_1 \exp\left(\frac{-i_{\mathrm{K}}^2}{2\sigma_2^2}\right) + (1-d_1)\exp\left(\frac{-i_{\mathrm{K}}^2}{2\sigma_3^2}\right)\right]\sin i_{\mathrm{K}}. \quad (39)$$

The third model, chosen to investigate the drop-off of the "halo," is a Gaussian plus a generalized Lorentzian multiplied by sin i_{K}:

$$f_{i_{\mathrm{K}}}(i_{\mathrm{K}}) = \left[\frac{1}{1+(2i_{\mathrm{K}}/i_{1/2,\mathrm{K}})^g} + d_2 \exp\left(\frac{-i_{\mathrm{K}}^2}{2\sigma_4^2}\right)\right]\sin i_{\mathrm{K}}. \quad (40)$$

The results of the least-squares fits for each model are listed in Table 15 and are displayed with the data in Figure 20. Note that the coefficients for the fits in Table 15 represent the amplitudes of the fractional inclination distribution (similar to Brown 2001 and Trujillo et al. 2001) and are thus not normalized to the number of objects in the sample. In Figure 20, the single Gaussian is represented by a dot-dashed line, the double Gaussian by a solid line, and the Gaussian plus Lorentzian by a dashed line.

To determine which of these models provides the best fit to the inclination distribution, we use a Kolmogorov-Smirnov (K-S) test (Press et al. 1992). The K-S test is insensitive to the choice of binning, since it uses a cumulative probability distribution. The cumulative probability distribution for the inclination data is plotted in Figure 20*b*, where each object has probability $1/N$ (where N is the total number of objects in the sample). The K-S statistic, $D\sqrt{N}$, is listed for each least-squares fit in Table 15. This statistic is used to calculate a probability that a greater deviation than that observed would occur by chance, if the model and the data were identical. For the number of objects in this sample, the lack of fit is significant when $D\sqrt{N}$ is greater than approximately 1.35 (corresponding to a 5% probability that a greater deviation would occur by chance). The significance level of the K-S statistic for the single Gaussian model is such that a deviation greater than that observed would occur by chance only a fraction of a percent of the time; therefore, this model is a very poor fit to the data. The K-S statistics for the double Gaussian and Gaussian plus Lorentzian models both correspond to a ~30% probability that a deviation greater than this would occur by chance. Thus, these fits are statistically acceptable and comparably good. These results are visually apparent in Figure 20*b*, where the fits are plotted with the cumulative data. We note that when the data are plotted in this way, an anomalous spike in the number of objects becomes apparent at $i_{\mathrm{K}} \approx 22°$; however, the statistical significance of this has not been investigated.

8.3. *Latitude Distribution from the Inclination Distribution*

At inclination i, the conditional probability density for finding an object at latitude β is $p(\beta|i)$. For circular, heliocentric

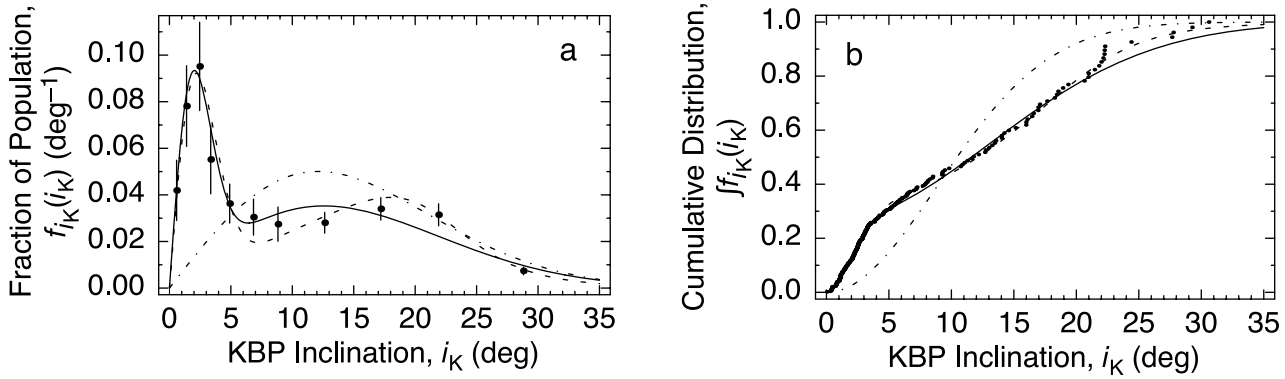

FIG. 20.—Model fits to the unbiased inclination distribution. The dot-dashed lines represent a single Gaussian × sin i_{K} fit, the dashed lines a Gaussian plus Lorentzian × sin i_{K} fit, and the solid lines a double Gaussian × sin i_{K} fit. (*a*) The total inclination distribution from Fig. 16 and the least-squares fits to the data. (*b*) The cumulative inclination distribution and the corresponding least-squares best-fit models. The cumulative representation of the data eliminates fitting biases due to binning. A K-S test on the data in (*b*) demonstrates that the double Gaussian × sin i_{K} and Gaussian plus Lorentzian × sin i_{K} models are equally good fits. An anomalous spike of objects at $i_{\mathrm{K}} = 22°$ is apparent in (*b*); however, the statistical significance of this has not been investigated.

orbits with probability density $p(i)$ for inclinations, the probability density for finding an object at latitude β is

$$p(\beta) = p(\beta \mid i)p(i) = \begin{cases} \dfrac{\cos\beta}{\pi\sqrt{\sin^2 i - \sin^2\beta}}p(i), & \text{if } |\sin\beta| < \sin i, \\ 0, & \text{if } |\sin\beta| \geq \sin i. \end{cases} \quad (41)$$

The total inclination distribution, $f_{i_K,n}$, represents the theoretical probability density for inclinations, $p(i)$. Therefore, the latitude distribution can be obtained by substituting the inclination distribution into equation (41).

Looking back at Figure 14, we compare the results for the latitude distribution determined by our two approaches. The first approach was to establish the density of objects discovered at different KBP latitudes, using all DES objects except for Centaurs (sample 1.3; see § 7). These data are represented as diamonds with error bars, corresponding to the fraction of the population per degree of latitude from the KBP. The second approach is to infer the latitude distribution from the inclination distribution with equation (41). These data are represented as triangles with error bars. Figure 14*a* shows the results from both approaches, over positive and negative latitudes. Since we expect the latitude distribution to be symmetric, Figure 14*b* shows the latitudes obtained from the object positions averaged over positive and negative latitudes, along with the data from the inclination distribution. Figure 14*c* displays the full extent of the latitude distribution as calculated from the inclination distribution shown in Figure 16. These different approaches for calculating the latitude distribution agree roughly, although not always within the error bars. This will be discussed further in § 9.4.

9. DISCUSSION

Identifying a relatively pristine classical belt is a prime objective of Kuiper belt research, since this remnant would be a window into the distant past of the solar system. In this section we discuss several aspects of our work as they relate to this objective. A cornerstone of this quest for the classical belt is our classification system for orbits, which we have formulated to be as dynamically meaningful as possible. We have also pursued the determination of the KBP, since it is the natural reference system for KBO orbits. Inclinations give us information regarding perturbations of the classical belt—some recent, but some likely occurring long ago, during the era of planetary migration. Related to the inclinations is the latitude distribution. Similarly, the magnitude distribution is currently our only handle on the population sizes of the different dynamical components of the Kuiper belt. We complete this section with a discussion of some issues that affect our survey work.

9.1. *Dynamical Classification*

Among all the distinctions drawn in our orbit classifications, the least subjective is between resonant and nonresonant orbits. We have identified an unprecedented number of resonances in the Kuiper belt to be securely occupied. The occupation of several first-order resonances—for example, the 3:2, 2:1, and 4:3 resonances—supports the idea that Neptune migrated outward early in its history over timescales $\geq 10^6$ yr (Malhotra 1995; Chiang & Jordan 2002). Surprisingly, even higher order resonances—for example, the 5:2—are filled to roughly the same degree as the first-order resonances. In the context of the migration model, this requires Neptune's resonances to have swept over a primordial belt having a substantial fraction of already dynamically excited ("preheated") objects (Chiang et al. 2003a). Such preheating is not anticipated by the standard migration scenarios but may find explanation in close encounters with Neptune during the migration era (Gomes 2003b). Furthermore, our discovery of the first Neptune Trojan vindicates long-held theoretical beliefs in their dynamical stability (Holman & Wisdom 1993; Nesvorný et al. 2000), and it promises to constrain the accretion history of Neptune (Chiang et al. 2003a).

The remaining divisions among nonresonant (Centaur, Classical, Scattered-Near, and Scattered-Extended) objects are subject to a variety of objections; for example, one can question the validity of the restricted, circular, three-body problem in describing dynamics that involve the presence of multiple giant planets. The intention behind our definitions is not to fully summarize the dynamics of every individual KBO through simplistic labels. Rather, we wish to provide a practical, first-cut classification scheme that has some basis in physics and that helps to organize thinking regarding the origin and evolution of the Kuiper belt. If our classifications stimulate deeper cosmogonical insights, we will have considered our exercise in drawing lines in the sand to be worthwhile.

To the extent that the classifications group objects according to physically meaningful categories, then the population fractions in each category can test models for the dynamical evolution of the Kuiper belt. Even if we were willing to assume that each class has the same albedo distribution (which likely is not the case), determining the unbiased fraction of objects in each population requires that we remove three principal observational biases from the raw population fractions of a controlled KBO sample, for which the DES qualifies. The first is a magnitude bias that accounts for the different mean distance for the objects in each classification; the second is an inclination bias that accounts for the different inclination distributions for the different classes; and the third is a recovery bias that accounts for the different likelihoods of recovering objects for each dynamical class. We plan to address these matters in the future.

9.2. *Kuiper Belt Plane*

Several issues regarding our determination of the KBP warrant further discussion: (1) comparison of our result with the previous work of Collander-Brown et al. (2003) and Brown & Pan (2004), (2) interpretation of the planes determined for different samples of objects, and (3) discussion of dynamics that might be at work to explain why our result differs from the Brouwer & van Woerkom (1950) theory.

9.2.1. *Comparison with Previous Work*

The first published investigation of the KBP was carried out by Collander-Brown et al. (2003), who calculated the average angular momentum for different subsets of KBOs under different assumptions about the masses of these bodies. We have not plotted their results in Figures 10–12, because they neither removed observational biases from their analyses nor estimated their errors. With unknown systematic and random errors, the significance of their results cannot be assessed. They do state, however, that the most reasonable conclusion from their work is that the plane of the Kuiper belt (if one can be defined) is very close to the invariable plane. To this extent, their results agree with what we have reported here.

A more definitive comparison of our results can be made with those of Brown & Pan (2004), since they used an unbiased method for determining the KBP and estimated their error (fit 0

of Table 12). In fact we have attempted to reproduce their analysis (fit 1 of Table 12), but as seen in Figure 10, our results do not agree with theirs. We attribute this difference to the fact that they used KBO velocities at the time of discovery based on orbits issued by the MPC, which necessarily involve certain assumptions to estimate an orbit from an arc that spans less than 24 hours in some cases (as shown in Table 10). In defense of their procedure, Brown & Pan point out that the velocity directions essentially depend on the inclination, and this is one of the best-determined orbital parameters from a short orbital arc. In Figure 2*b*, however, we note that the designated but not dynamically classified objects (the category into which all newly discovered KBOs fall) have, as a group, a significantly larger average inclination (*gray bar*, *top*) than the average inclination for dynamically classified objects (*black bar*). We believe that this inclination bias is the reason for the difference between the two KBP determinations, and that ours is the more reliable. Therefore we discount the claim by Brown & Pan (2004) that the invariable plane can be ruled out as the KBP at greater than the 3 σ level.

9.2.2. *Mean Orbit Planes for Different Samples of KBOs*

Using the maximum likelihood method, we determined the mean plane for several subsets of the main KBO population (Table 13). We define an index for the internal consistency for each of these subsets, $\sigma_{\rm subset}$, as the product of the standard deviation of the fitted inclination of the plane, $\sigma_{i,\,\rm subset}$ (relative to the ecliptic), and the square root of the number of objects, $N_{\rm subset}$, in the subset:

$$\sigma_{\rm subset} = \sigma_{i,\,\rm subset}\sqrt{N_{\rm subset}}. \tag{42}$$

The square of $\sigma_{\rm subset}$ is the contribution to the variance in the fitted inclination of the mean orbit plane by each object in the subset. Thus, the smaller the value of $\sigma_{\rm subset}$, the more consistently the subset under consideration defines a mean plane. This quantity is tabulated in the final column of Table 13 for each of the subsets investigated.

Using the set of all MPC objects (fit 1 in Table 13) as a benchmark, we see that $\sigma_{\rm subset}$ is reduced by removing the objects with pole errors greater than $0\overset{\circ}{.}5$ (fit 2 in Table 13), which is not surprising. We see a further reduction in $\sigma_{\rm subset}$ when we limit our selection to only Classical objects (fit 3 in Table 13)—what we might characterize as a core population. Finally, we fit the objects in the 3:2 resonance and get an extremely large value for $\sigma_{\rm subset}$, showing that the orbit planes for these objects exhibit a large scatter about their mean plane.

9.2.3. *Dynamical Possibilities*

The sample of Classical objects (fit 3 in Table 13) defines a mean orbit plane with a precision of $\pm 0\overset{\circ}{.}22$, and the subset of Classical objects culled for low inclinations (fit 5 in Table 13) is characterized by virtually the same precision, $\pm 0\overset{\circ}{.}20$. As can be seen in Figure 12, the poles of these planes lie much closer to the pole of the invariable plane (and naturally, the orbit pole of Jupiter) than to the normal of the Laplacian surface defined by the BvW model. The latter is indicated by the line in the lower left of the figure, on which the semimajor axis scale is indicated by the cross ticks. This lack of agreement between the BvW model and the mean plane of the Classical objects (which have a mean semimajor axis of 43.88 AU, as indicated in Table 13) would imply one of the following: (1) the Classical KBOs in our sample do not satisfy the assumptions of the BvW model, or (2) our analysis is flawed by errors or incorrect assumptions.

Why might the BvW theory be inadequate to the task of determining the plane of the KBP? It is a purely secular theory that is good only to second order in the eccentricities and inclinations of the bodies. The sample to which the theory is most appropriately applied is that of fit 5 (Table 13): Classical KBOs whose inclinations with respect to their mean plane are less than 5°. The filter for low inclinations notwithstanding, the restriction to low eccentricity embodied by Classical objects ($e \leq 0.2$) may still be too loose for the low-order BvW theory to be appropriately applied. Note that the sample used in fit 5 overlaps with a region of instability spanning semimajor axes of 40–45 AU and eccentricities near 0.15 (Duncan et al. 1995); the full extent of this region is not contained within the BvW theory. Moreover, purely secular theories like that of BvW, regardless of their order, suffer from the drawback that they do not exhibit the widespread chaos associated with the overlap of high-order mean motion resonances. In summary, higher order resonant and secular perturbations threaten to destroy the invariance of free inclinations that is crucial to the determination of the Laplacian surface in the BvW theory.[14]

We have undertaken a preliminary set of numerical integrations that, to a certain extent, bear these concerns out; they show that free inclinations are increasingly not conserved as greater initial inclinations (with respect to the Laplacian plane) and eccentricities are considered. These same integrations also show that the semimajor axes of Classical KBOs vary with time by as much as 1 AU—behavior that is forbidden in purely secular theories like that of BvW and that blurs the Laplacian surface defined by that theory. A more complete analysis is deferred to future investigation.

If free inclinations are not conserved because of higher order perturbations not accounted for by BvW, then what plane should KBOs respect? The leading candidate would be the invariable plane, since the periods of nodal precession of KBOs about the local Laplacian pole (the free precession periods) are longer than the periods of nodal precession of the planets (the forced precession periods) about the invariable pole. In other words, the periods of orbit precession about the BvW pole are longer than that of the BvW pole about the invariable plane. For Classical KBOs, the factor by which the former are longer is at least a few. In the limit where this factor is large, KBOs see a potential that smears itself axisymmetrically about the invariable pole; then the KBOs would nodally precess about the invariable plane, which is consistent with our observational result.

9.3. *Inclination Distribution*

Our investigation of the inclination distribution confirms the ideas of the "cold" and "hot" populations discussed by previous authors (e.g., Levison & Stern 2001). We find that the data are well fitted by sin *i* multiplied by the sum of two Gaussians having standard deviations of $1\overset{\circ}{.}94 \pm 0\overset{\circ}{.}19$ and $12\overset{\circ}{.}68 \pm 0\overset{\circ}{.}64$ (FWHMs are $4\overset{\circ}{.}57 \pm 0\overset{\circ}{.}45$ and $29\overset{\circ}{.}86 \pm 1\overset{\circ}{.}51$, respectively). This result is generally consistent with that of Brown (2001), who fitted the same function to a smaller sample of objects and obtained Gaussians with standard deviations of $2\overset{\circ}{.}6^{+0.8}_{-0.2}$ and $15^\circ \pm 1^\circ$. This result is also consistent with the double Gaussian fit from Trujillo et al. (2001), which has standard

[14] Free inclinations in the context of the BvW theory are the inclinations with respect to the local Laplacian plane.

deviations of 2.°2 and 18°. Contrary to Trujillo et al. (2001), we do not believe that a single Gaussian adequately describes the inclination distribution. The smaller standard deviations of our Gaussians are likely due to the fact that we use the KBP, rather than the ecliptic, as a reference plane for the orbital inclinations.

Because of the geometric sin i factor in any inclination distribution, the concentration of objects near zero inclination is most evident in a plot that reveals the density of orbit poles in the sky near zero inclination, as shown in Figures 18 and 19. This view reveals a highly concentrated core of objects, with a FWHM of 4.°6 in orbital inclination, surrounded by a less dense concentration of objects (which suggests the descriptive terms, "core" and "halo," as alternative descriptive terms for the "cold" and "hot" populations, respectively). Although the core exhibits a strong peak in the density of orbit poles, the distribution at higher inclinations is much shallower and broader. This terminology is supported by the data being equally well fitted by the Gaussian plus Lorentzian model as by the double Gaussian model.

As expected from our definition of the Classical population having low eccentricity, Figure 17 demonstrates that the core is composed primarily of Classical objects. The lower inclinations of the halo are populated by Classical and Resonant objects, while the Scattered and Resonant objects make up the higher inclinations. The shapes of the inclination distributions for each of these classes are consistent with those of Brown (2001). If one combines the Classical and Scattered populations displayed in Figure 17, the result is relatively flat outside the core (the low notch at 7° could be an artifact of the binning). Objects outside this core could be just an extension of the core population, with the origin of the two populations arising from a common process—or, the core and halo populations could have two quite distinct origins. Establishing the relationship, if any, between the "core" (or "cold") and "halo" (or "hot") populations will require a deeper understanding of the dynamical processes at work in the past and today.

One might question the particular characteristics of objects in this core. Trujillo & Brown (2002) noted a correlation of color with inclination, which has been confirmed by others (e.g., Doressoundiram et al. 2002; Tegler et al. 2003). Further investigations in this area may be fruitful in connecting dynamical properties with physical properties (e.g., Gulbis et al. 2005), which could give us more insight into the ancient history of KBOs—the Classical population in particular.

9.4. *Latitude Distribution*

The distribution of KBO orbital inclinations can be used to determine the latitude distribution. Hence the comparison in Figures 14*a* and 14*b* between the latitude distributions derived from the positions of DES objects in the sky (*diamonds*) and the latitude distribution inferred from our derived inclination distribution (*triangles*) serves as a consistency check of our analyses. Although there is good general agreement, the inclinations indicate a somewhat sharper concentration at the KBP than we find from the distribution of objects. At present we have no explanation for this apparent discrepancy between these two approaches, and it will be a topic of further study.

The distribution above KBP latitudes of 5° is not currently well constrained by DES results, except for what can be inferred from the inclination distribution, which is shown in Figure 14*c*. This region has been investigated by Trujillo et al. (2001, their Fig. 13), who report a sharp decline in the sky density with increasing ecliptic latitude, based on observations at 0°, 10°, and 20° ecliptic latitude. Our results agree with this trend and suggest some additional structure, such as a flattening of the distribution at inclinations between 10° and 25°.

9.5. *Provisional Magnitude and Size Distributions*

We can compare our provisional magnitude distributions given in Table 14 and Figure 13 with those of Bernstein et al. (2004, their Table 3 and Fig. 6). Their compilation of survey results covers a wide range of magnitudes, which allows them to fit a double power-law model with a slope change in the 23–26 mag range (for different subpopulations). Our DES results are restricted to only the brightest objects in this range, so we therefore compare our single power-law results only with the bright-end slope presented by Bernstein et al. (2004).

Furthermore, for the restricted samples of objects (fits 5–12 in Table 14), we use the results with the two survey sensitivity parameters ($\Delta m_{1/2-2\sigma}$ and σ_m) fixed at the value for all designated *VR* KBOs (fit 4 in Table 14). Whatever the sensitivity of the DES, it should be the same to first order for all dynamical classes. The *VR* KBOs constitute our largest photometrically homogeneous sample of DES objects (sample 1.3) and should yield the best values for our sensitivity parameters—with the caveat that a single power-law distribution accurately describes the magnitude distribution function over the range of magnitudes accessible to the DES. If the fixed values of the sensitivity parameters contain systematic errors, they will affect the fitted power-law exponent in the same way for different model fits. Hence, statistically different fitted power-law exponents are meaningful.

As a first comparison, we note that the Bernstein et al. (2004) best-fit solution for the bright-end slope for the population of all KBOs is $\alpha = 0.88$, with a $\pm 1\ \sigma$ range of 0.75–1.2. We find $\alpha = 0.86 \pm 0.10$ (fit 2 in Table 14) for all *VR* DES KBOs, a remarkably good agreement. We note that the Bernstein et al. analysis did not include any DES objects in their compiled catalog of KBOs, so this independent determination of the bright-end slope is a strong confirmation of our mutual results. Bernstein et al. divided their sample into subpopulations—a classical population (whose definition is different but whose members mostly overlap with our definition of Classical bodies) and an excited subpopulation (everything else in the Bernstein et al. sample, including what we classify as Resonant and Scattered objects). Bernstein et al. (2004) find $\alpha = 0.66$ with a $\pm 1\ \sigma$ range of 0.6–0.75 for their excited sample. Here we again find agreement with our power-law fits for Excited ($\alpha = 0.58 \pm 0.09$), Resonant ($\alpha = 0.52 \pm 0.08$), and Scattered ($\alpha = 0.74 \pm 0.15$) populations. Note that the power laws for the Classical and Scattered agree at values near 0.8—it is just the Resonant class that has a shallower power law at 0.52 (see Table 14).

Our agreement does not extend to the Classical subpopulations. Bernstein et al. (2004) find $\alpha = 1.36$ with a range of 1.05–1.5 (upper limit by fiat) compared with our best fit of $\alpha = 0.74 \pm 0.05$. However, at the 2 σ level our results agree with Bernstein et al. (2004). Furthermore, we note that the total Bernstein et al. sample comprises 129 objects throughout their entire magnitude range ($R = 19$–28 or so). Our fits presented here are derived from 415 objects, all of which would fall into Bernstein et al.'s bright-end subpopulation. It is possible that a reconsideration of the Bernstein et al. analysis in light of the DES KBOs presented here would produce a somewhat different result that would be more in agreement with the DES-only result for Classical KBOs in Table 14. In addition, our dynamical classification system does not entirely overlap with the simpler approach of Bernstein et al. (2004). Further analysis is warranted, as these power-law slopes may directly reflect the formation and evolution histories of KBO subpopulations.

The power-law slopes described above are generally represented by α, the exponent of the magnitude distribution. This α is related to q, the power-law exponent for the differential size distribution, through the simple relation $q = 5\alpha + 1$. This relation assumes that all bodies under consideration share a common albedo and that all bodies are at the same distance. We calculate $q = 5.15$ for all DES KBOs, with similar results for the Classical and Scattered subpopulations. The Excited and Resonant populations have q-values of 4.1 and 3.8, respectively, which are closer to the values that have been found in the past. As physical models of KBO evolution—including accretion and collisional grinding—mature, the derived size distributions will act as a strong constraint. We note that as KBO subpopulations become more completely cataloged and as we learn more about KBO albedos in the coming years through observations with the *Spitzer Space Telescope*, we may have to reconsider the assumptions made above when comparing *N*-body model results and observed sky densities.

Finally, we note that our agreement of the power laws for the Classical and Scattered populations adds to the lack of discernment of the distinction between these two dynamical classes that we noted in § 9.3.

9.6. *Survey Issues*

In this section we discuss limitations for the DES imposed by our current magnitude and sensitivity calibrations, followed by commenting on the availability of DES data. We also discuss the value of a community-wide effort to submit all KBO astrometry to the common database provided by the MPC.

9.6.1. *Photometric Calibration*

As described in § 2.2.2, the photometric calibration used here is tied to the magnitudes in the USNO-A2.0 and -B1.0 catalogs. At present, we can only evaluate the accuracy of our current calibration through comparison with the results of a well-calibrated survey, such as the Canada-France-Hawaii Telescope (CFHT) survey of Trujillo et al. (2001)—although their survey used a Mould *R* filter. For all KBOs, they find that the cumulative distribution function for magnitudes yields a magnitude for a sky density of 1 object per square degree, $m_0 = 23.04^{+0.08}_{-0.09}$, and we find $m_0 = 22.70 \pm 0.13$ (fit 2 of Table 14). Taken at face value, the DES magnitudes are 0.34 ± 0.15 too bright. In addition to (1) errors in the current DES photometric calibration, other contributing factors to this difference may be due to (2) not accounting for the differences in KBO density as a function of latitude from the KBP (Fig. 14) for the DES and CFHT surveys and (3) the need for a more accurate calibration of the DES detection efficiency. We are carrying out a photometric calibration program to address point 1 above. This goal requires making ~4000 independent photometric observations, of which we have made ~25% to date. Observations are being made with the 31 inch (0.8 m) telescope at Lowell Observatory in automated data acquisition mode and with the Steward Observatory 61 inch (1.5 m) telescope on Mount Bigelow. We expect to complete the photometric calibration within 6 months of the conclusion of the formal DES program. At that point, the entire DES catalog of photometric measurements can be recalculated, resulting in KBO magnitudes with significantly smaller error bars and fewer systematic uncertainties.

9.6.2. *Calibration of Detection Efficiency*

The detection efficiency for the DES was first addressed in Paper I (Fig. 4 there), where we showed the results of some limited tests that involved the insertion of artificial sources into data frames that were then examined for moving objects. This calibration was carried out with just a few frames. When we attempted to use the efficiency function so derived to analyze the current data set with the parameters fixed at those previously determined, it became apparent that either the magnitude distribution of the KBOs detectable with the DES was not well described by a power law or the detection efficiency parameters were not correct. Pursuing the latter explanation, we then allowed the detection efficiency parameters to be fitted (Table 14), which gave quite satisfactory results with an assumed single power-law distribution. Clearly, to get the most information from the survey data we need an independent calibration of the survey efficiency, and the standard way to accomplish this is by the insertion of synthetic objects into the data stream prior to the moving-object detection. We shall be experimenting with this procedure in the future.

9.6.3. *The Value of KBO Astrometric Measurements*

A not uncommon view within the KBO community is that once a KBO has a provisional designation, there is little point in compiling further astrometric information. However, many provisionally designated KBOs are not yet dynamically classified (Fig. 5). More classifications are needed to achieve a more accurate determination of the KBP so that we can learn whether the KBP is actually the invariable plane (Fig. 12). In addition, follow-up observations of KBOs with large ground-based telescopes, or space-based telescopes such as *HST* and the *Spitzer Space Telescope*, require accurate ephemerides, which can only be generated from accurate long-arc astrometry of these objects. Therefore we urge all who can generate KBO astrometric measurements as a by-product of other KBO work to do so and to submit their measurements to the MPC. Even after KBO orbits become accurate enough for dynamical classification, further improvement in orbital accuracy for the larger bodies will facilitate the prediction of stellar occultations (Elliot & Kern 2003), from which we can directly measure KBO sizes and shapes. Stellar occultation data can also be used to probe for possible tenuous atmospheres and to probe for nearby binary companions—which should be ubiquitous according to at least one model for binary formation (Goldreich et al. 2002).

9.6.4. *Access to DES Data and Survey Results*

Our survey status at NOAO means that all data are archived and freely available to the community from NOAO. In Appendix A, we discuss the information submitted to NOAO, including the key words added to the calibrated frame headers that give the limiting magnitude of each frame and other information to facilitate their use. These data, along with the discovery information in Tables 6–10 (designated discoveries) and the supplementary tables (including Table A4, undesignated discoveries) give all that should be necessary to reproduce and extend the analyses that we have presented. Auxiliary DES resources and the uniform resource locators (URLs) to access them are presented in Appendix A and Buie et al. (2003).

10. CONCLUSIONS

With a 50% detection efficiency at a magnitude of 22.5 (Fig. 13*b*), the DES is an intermediate-magnitude survey, with much more solid-angle coverage than the faint-object surveys (e.g., Bernstein et al. 2004) and many more objects detected than the bright-object surveys (e.g., Trujillo & Brown 2003).

Hence the DES is well suited to probe the dynamical properties of the general population of KBOs. As an aid to understanding these properties, we have sharpened the traditional meanings of the dynamical classes—Resonant, Scattered, and Classical.

In defining "Classical," we are trying to determine those KBOs with orbits that have been relatively undisturbed since the origin of the solar system. Indeed, we see a strong concentration of orbit poles within 2°–3° of the average orbit pole for the Kuiper belt (Fig. 19). This prompts the inference that these core objects represent a distinct population, with a different history from others. Although it is tempting to conclude that this core of KBOs represents what is left of the primordial Kuiper belt, we must bear in mind that the tail of the inclination distribution from the Classical objects blends smoothly into the inclination distribution of Scattered objects (Figs. 18 and 19). At present we see no clear demarcation between these two classes in their orbital elements, and we have somewhat arbitrarily set their boundary at an orbital eccentricity of 0.2. As we gain more dynamical insight, we may want to use a classification criterion based on orbital inclination, as others have done, with 5° being a popular choice for the boundary between the Classical and Scattered classes (e.g., Bernstein et al. 2004). These two dynamical classes have power laws for their respective magnitude distributions that are indistinguishable at present as well.

Contrary to past work, however, we recommend that the inclinations used in a dynamical classification system be referred to the Kuiper belt plane, which needs to be better understood before using an inclination-based criterion for dynamical classification. This is one of our goals for the future. We would also like to establish population estimates for the dynamical classes, to derive the size distribution for each, and to estimate the mass of those components in each class that are accessible to our survey. In order to carry out these tasks, we need to improve the magnitude and sensitivity calibrations of the DES so that the observational biases can be more accurately removed.

Thanks go to J. Pittichová, S. Ash, J. Bauer, T. Chun, Y. Fernandez, H. Hsieh, M. Kadooka, and N. Moskovitz for their help with the observing at Mauna Kea. We are thankful for the help of numerous students, including K. Dekker, L. Hutchison, S. Hylton, J. Kane, L. Lundgren, G. Panova, S. Qu, and M. Trimble under the auspices of the NSF Research Experiences for Undergraduates program and the MIT Undergraduate Research Opportunities Program. We also appreciate the work of numerous observers for their recovery observations, including X. Bussman, J. Lovering, D. Osip, C. Ruggles, C. Salyk, P. Schechter, R. Simcoe, and R. M. Wagner. We thank the telescope operators from KPNO: A. Alday, E. Eastburn, B. Gillespie, H. Halbedel, H. Mathis, G. McDougall, and D. W. Willmarth; from CTIO: A. Alvarez, A. Guerra, S. Pizarro, and P. Ugarte; from Steward: D. Means; and from Magellan: O. Duhalde, G. Martin, V. Meriño, M. Navarrete, H. Nuñez, H. Rivera, F. Sánchez, and H. Valladares. Our work with the KBP was inspired by a seminar given by Mike Brown at Lowell Observatory on 2003 August 1. This research was supported in part by NASA grants NAG 5-13380 and NAG 5-11058 at Lowell Observatory; NASA grants NAG 5-3940, NAG 5-10444, and NNG04GF25G and NSF's Division for Astronomical Sciences grant AST 04-060493 at MIT; the Alfred P. Sloan Foundation at the University of California, Berkeley; and NASA grants NAG 5-4495 and NAG 5-12236 at the University of Hawaii. D. E. T. acknowledges support from the American Astronomical Society in the form of a Small Research Grant and from the Space Telescope Science Institute under grant GO-9433.06. Support for program GO-9433 was provided by NASA through a grant from the Space Telescope Science Institute, which is operated by the Association of Universities for Research in Astronomy (AURA), Inc., under NASA contract NAS 5-26555. NOAO distributes the IRAF program, used for some of the image processing in this paper, and NOAO maintains the observing facilities used in this investigation. NOAO is operated by AURA, Inc., under cooperative agreement with the National Science Foundation.

APPENDIX A

ELECTRONIC RESOURCES

We endeavor to achieve the principle that anyone could reproduce our results, given the images archived at NOAO and the information in this paper. To that end, we present supplementary information in this appendix concerning (1) additional key words on our archived survey frames at NOAO, (2) parameters determined in our reductions that characterize each of the survey frames, (3) the center coordinates for each search field, and (4) characteristics of the undesignated objects used in our analyses.

A1. ARCHIVED FRAMES AT NOAO

The calibrated data are submitted to the NOAO archive with the key words in Table A1 added to the header of each image file. These data are available to download from the NOAO Science Archive.[15] Note that the right ascension and declination in the image header are the pointing coordinates of the telescope for the center of the Mosaic field, and they have not been corrected by the astrometric reduction.

A2. FRAME CHARACTERIZATION

Each Mosaic field comprises eight subframes (corresponding to the eight CCDs). The characteristics of each of the subframes are logged in Table A2. The columns of the table are (1) file name with CCD number extension (FILENAME), (2) the DES internal field name ("Field Name"), (3) length of the exposure in seconds (EXPTIME), (4) air mass of the field (AIRMASS), (5) robust average of the full width at half-maximum of all sources in the image, in pixels (FWHMPX), (6) average sky signal level in data numbers (DN) per pixel (SKY), (7) standard deviation of the sky signal in DN pixel^{-1} (SKYSIG), (8) number of sources detected ("Sources"), (9) fraction of the pixels that exceed the average sky level by 50 times the standard deviation of the sky signal ("Frac. 50Sig"), (10) fraction of the pixels that exceed the average sky level by 5 times the standard deviation of the sky signal ("Frac. 5Sig"), (11) photometric zero-point correction in magnitudes, based on the photometry in the USNO-A2.0 and -B1.0 star catalogs that were

[15] See http://archive.noao.edu/nsa/.

TABLE A1

DESCRIPTION OF KEY WORDS ADDED TO HEADERS OF IMAGE FILES SUBMITTED TO NOAO

Key Word	Explanation of Quantity
DEPTH	The 5 σ detection above the background sky for the case of a Gaussian point-spread function dominated sky (magnitudes). The equation used is DEPTH = ZEROP − 2.5 log (1.2 × 5 × FWHMPX × SKYSIG)
DESGAIN[a]	The gain value used in reducing the data (e^- DN^{-1})[b]
ETA_Cn[c]	Values for (x, y)-to-η transformation; allows conversion from pixel positions to right ascension and declination
ETADECTP, XIDECTP	Declination in the tangent-plane astrometric solution (sexagesimal).
ETARATP, XIRATP	Right ascension in the tangent-plane astrometric solution (sexagesimal)
FWHMPX	The robust average of FWHM of identified astrometric sources in the image (pixels)
MAG_BR	Saturation magnitude: Magnitude of a synthetic object, constructed from a stacked point-spread function taken from the image, whose peak pixel is 65,000 minus the sky signal (SKY). This value is computed by integrating over the scaled point-spread function with the aperture used for the reductions and adding the photometric zero point (PHOTZP).
MAG_LIM	Limiting magnitude: Magnitude of a synthetic object, constructed from a stacked point-spread function taken from the image, whose peak pixel is 3 times the sky signal (SKY). This value is computed by integrating over the scaled point-spread function with the aperture used for the reductions and adding the photometric zero point (PHOTZP).
PHOTZP	The photometric zero point, defined by the average difference between the instrumental magnitudes (with a zero-point magnitude scale of 24.0) and the USNO-A2.0 catalog red magnitudes for the stars used in the astrometric solution
SEEING	The robust average of FWHM of identified astrometric sources in the image (arcsec)
SKY	Sky signal: The robust average of an annulus centered on the source with inner and outer radii of the aperture used for reduction plus 1 and 5 pixels, respectively (DN)[b]
SKYSIG	The standard deviation of the values obtained for calculation of the sky signal (DN)[b]
XI_Cn[c]	Values for (x, y)-to-ξ transformation; allows conversion from pixel positions to right ascension and declination
ZEROP	The USNO-A2.0 or -B1.0 red magnitude of a 1 ADU s^{-1} source[b]

[a] In the archived file headers, this quantity is listed as photons per ADU.

[b] The notations ADU and DN are used interchangeably.

[c] ETA and XI values are submitted for each of the 10 coefficients determined in the astrometric fit, where n = 0, 1, . . . , 9. The formula for this calculation is provided as a comment in the headers of the archived data.

TABLE A2

IMAGE CHARACTERIZATION

FILENAME	Field Name	EXPTIME	AIRMASS	FWHMPX	SKY	SKYSIG	Sources	Frac. 50Sig	Frac. 5Sig	PHOTOZP	Sat. Mag.	Limiting Mag.
000205.001x1.....	S98WA31	300.0	1.11	3.86	6308	46	1474	0.003	0.019	1.757	16.01	23.00
000205.002x1.....	S98WA31	300.0	1.12	3.60	6083	43	1243	0.004	0.018	1.738	16.08	23.16
000205.003x1.....	S98WT31	300.0	1.08	3.90	5638	42	928	0.005	0.020	1.437	15.66	22.78

NOTE.—Column headers in all caps correspond to NOAO key words (see Table A1 for a partial listing and http://iraf.noao.edu/projects/ccdmosaic/Imagedef/mosaic/MosaicV1.html for a complete listing), while the remaining headers are internal designations (defined in Appendix A). Table A2 is presented in its entirety in the electronic edition of the Astronomical Journal. A portion is shown here for guidance regarding its form and content.

TABLE A3

OBSERVED FIELD CENTER COORDINATES

Field Name	UT Observation Date	R.A. (J2000)	Decl. (J2000)
F00005	2000 Sep 19	00 00 01.84	+03 36 24.3
F00006	2003 Oct 24	00 00 01.73	+03 00 03.6
F00008	2000 Aug 6	00 00 03.83	+01 47 23.1

NOTE.—Table A3 is presented in its entirety in the electronic edition of the Astronomical Journal. A portion is shown here for guidance regarding its form and content.

used for the astrometric reduction, and with a zero-point magnitude scale of 24.0 (PHOTOZP), (12) saturation magnitude for a point source ("Sat. Mag."), and (13) the 2 σ limiting magnitude of the image on the faint end, defined as the magnitude of a synthetic object, constructed from a stacked point-spread function taken from the image, whose peak pixel is twice the sky signal ("Limiting Mag."). The 2 σ limiting magnitude is computed by integrating over the scaled point-spread function with the aperture used for the reductions and adding the photometric zero point.

A3. FIELD CENTERS

In Table A3, we provide the center coordinates for each of the survey fields used in our analyses for this paper, regardless of whether an object was found in the field. This table includes (1) the DES field name, (2) UT date of observation, (3) right ascension (J2000) of the center of the field, and (4) declination (J2000) of the center of the field. Note that some of the field names are identical. This represents the situation in which a search field was observed multiple times.

A4. UNDESIGNATED OBJECT INFORMATION

We provide information about undesignated objects in Table A4. This information was used in the comparison of data samples and in the analyses for the magnitude distribution. Table A4 includes (1) internal object name or "Local ID," (2) UT discovery date, (3) discovery right ascension (J2000), (4) discovery declination (J2000), (5) magnitude of the object in the filter in which it was observed (*VR* unless otherwise noted on the night of discovery in Table 1; see Paper I for objects discovered prior to 2000 April), (6) heliocentric distance of the object at the time of discovery, (7) discovery inclination, and (8) longitude of the ascending node at discovery. The latter two quantities are found using the formalism of Bernstein & Khushalani (2000). Since the errors on the calculated orbital elements are quite large for undesignated objects, as discussed in Paper I, these values have been presented to low precision.

A5. OBSERVING RESOURCES

Up-to-date information of survey observations beyond this paper can be found at the DES home page.[16] Current coordinates and orbital elements for all KBOs are available via anonymous ftp from Lowell Observatory.[17] Details about the links and files at these locations are presented in Buie et al. (2003).

APPENDIX B

INTEGRATIONS IN KUIPER BELT PLANE COORDINATES

The calculations required to compute the bias factors for the latitude and inclination distributions of KBOs require certain integrations in Kuiper belt coordinate space, as called for in equations (29) and (35). We assume that the angular intervals involved in these integrations are small. In this appendix, we consider the transformation of a solid-angle element from right ascension–declination (α, δ) coordinates to another spherical coordinate system, defined by longitude and latitude coordinates (λ, β). For small solid-angle elements far from the pole of either coordinate system, the transformation can be well approximated by (1) a transformation of the center coordinates, $(\alpha_0, \delta_0) \rightarrow (\lambda_0, \beta_0)$, followed by (2) a rotation by an angle θ, defined as the position angle (measured from north through east) of the β-axis in the (α, δ) coordinate system. This is illustrated in Figure 21, where the solid-angle element has an extent $\Delta\alpha$ in right ascension and $\Delta\delta$ in declination. The transformation between (α, δ)-coordinates and (λ, β)-coordinates can be specified by the position of the pole, (α_p, δ_p), for the (λ, β) coordinate system. In terms of (α_p, δ_p), the local rotation angle, θ, is determined by equations for its sine and cosine:

$$\sin\theta = \cos\delta_p \sin(\alpha_p - \alpha_0), \qquad \cos\theta = \sin\delta_p \cos\delta_0 - \cos\delta_p \sin\delta_0 \cos(\alpha_p - \alpha_0). \tag{B1}$$

For the case illustrated in Figure 21, which is drawn under the assumption that $|\theta| \leq |\arctan(\Delta\delta/\Delta\alpha \cos\delta_0)|$, we define three auxiliary quantities:

$$\Delta\lambda_{\max} = \Delta\alpha \cos\delta_0 \sec\beta_0 \sec\theta, \qquad \Delta\beta_1 = \Delta\alpha \cos\delta_0 |\sin\theta|, \qquad \Delta\beta_2 = \Delta\delta - \Delta\beta_1 \sec\theta. \tag{B2}$$

Note that the first quantity, $\Delta\lambda_{\max}$, is the maximum λ-interval within the frame (*not* the maximum extent of the frame on the λ-axis; see Fig. 21).

We shall be more concerned with integrations over the latitude coordinate, and for these integrations we require two more auxiliary quantities, $\beta_{\min}$ and $\beta_{\max}$. These quantities are illustrated in Figure 21 and are defined by the following equations:

$$\beta_{\min} = \beta_0 - (\Delta\beta_1 + \Delta\beta_2), \qquad \beta_{\max} = \beta_0 + (\Delta\beta_1 + \Delta\beta_2). \tag{B3}$$

[16] Located at http://www.lowell.edu/Research/DES/.
[17] See ftp://ftp.lowell.edu/pub/buie/kbo/recov/.

TABLE A4
Undesignated Object Discovery Characteristics

Local ID	UT Discovery Date	R.A. (J2000)	Decl. (J2000)	Frame Mag.	R (AU)	i (deg)	Node (deg)
MB2548	2000 Feb 5.140	08 09 39.5	+21 44 20	22.7	28	52	119
MB2651	2000 Feb 5.149	08 29 10.0	+19 35 28	23.8	55	21	124
MB2710	2000 Feb 5.153	08 28 29.7	+19 16 59	23.8	41	8	306

Note.—Table A4 is presented in its entirety in the electronic edition of the Astronomical Journal. A portion is shown here for guidance regarding its form and content.

The integral in equation (29) requires knowledge of the longitude interval, $\Delta\lambda(\beta)$, within the solid angle covered by a search frame. By inspection of Figure 21, this can be written in terms of the quantities defined above as follows:

$$\Delta\lambda(\beta) = \begin{cases} 0, & \text{if } -\pi/2 \le \beta < \beta_{\min}, \\ \Delta\lambda_{\max}\dfrac{\beta - \beta_{\min}}{\Delta\beta_1}, & \text{if } \beta_{\min} \le \beta < \beta_{\min} + \Delta\beta_1, \\ \Delta\lambda_{\max}, & \text{if } \beta_{\min} + \Delta\beta_1 \le \beta \le \beta_{\max} - \Delta\beta_1, \\ \Delta\lambda_{\max}\dfrac{\beta_{\max} - \beta}{\Delta\beta_1}, & \text{if } \beta_{\max} - \Delta\beta_1 < \beta \le \beta_{\max}, \\ 0, & \text{if } \beta_{\max} < \beta \le \pi/2. \end{cases} \tag{B4}$$

If the boundary between two latitude bins occurs at latitude β_b, then the amount of solid angle, $\Omega(<\beta_b)$, at latitudes less than β_b and contained in the schematic frame depicted in Figure 21 is given by

$$\Omega(<\beta_b) = \begin{cases} 0, & \text{if } -\pi/2 \le \beta_b < \beta_{\min}, \\ \frac{1}{2}(\beta_b - \beta_{\min})\Delta\lambda(\beta_b)\cos\beta_0, & \text{if } \beta_{\min} \le \beta_b < \beta_{\min} + \Delta\beta_1, \\ \left(\beta_b - \dfrac{\beta_1}{2} - \beta_{\min}\right)\Delta\lambda_{\max}\cos\beta_0, & \text{if } \beta_{\min} + \Delta\beta_1 \le \beta_b \le \beta_{\max} - \Delta\beta_1, \\ \left[\left(\dfrac{\beta_1}{2} + 2\beta_2\right)\Delta\lambda_{\max} + \dfrac{1}{2}(\beta_b - 2\beta_2 - \beta_{\min})\Delta\lambda(\beta_b)\right]\cos\beta_0, & \text{if } \beta_{\max} - \Delta\beta_1 < \beta_b \le \beta_{\max}, \\ (\beta_1 + 2\beta_2)\Delta\lambda_{\max}\cos\beta_0, & \text{if } \beta_{\max} < \beta_b \le \pi/2. \end{cases} \tag{B5}$$

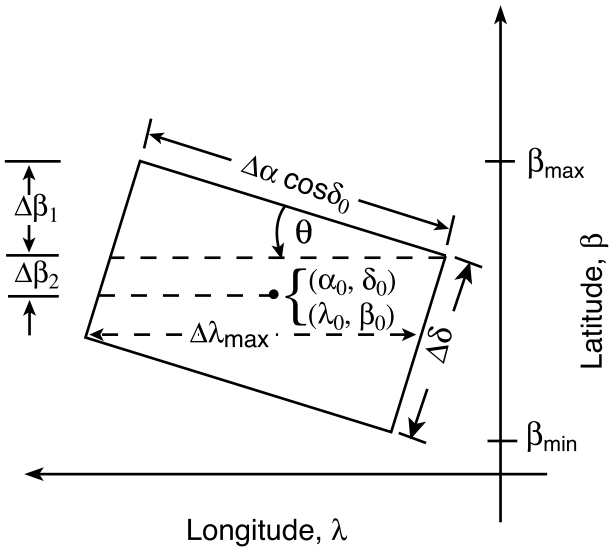

Fig. 21.—Coordinate conversions for solid angles. A rectangular element of solid angle, aligned with the (α, δ) coordinate axes, has an extent $\Delta\alpha$ in right ascension and $\Delta\delta$ in declination. We consider the transformation of this solid angle to another spherical coordinate system that has longitude and latitude coordinates (λ, β). The solid-angle element is far from the pole of either coordinate system, so that we can approximate the coordinate transformation by a rotation of the rectangular element by an angle θ, defined as the position angle (measured from north through east) of the β-axis in the (α, δ) coordinate system. The corners of the rectangle define the minimum and maximum values of β, denoted by $\beta_{\min}$ and $\beta_{\max}$. The two dashed lines are parallel to lines of constant latitude, and these break up the solid-angle element into two triangles and a single parallelogram, over which it is convenient to carry out integrations over solid angles.

APPENDIX C

GLOSSARY OF SYMBOLS

a	Semimajor axis of object orbit
$a_{\rm N}$	Osculating semimajor axis of Neptune
$\bar{a}_{\rm subset}$	Mean semimajor axis of a subset of objects
b	Dimensionless parameter used to model the sky density of object velocity directions
$c_{i'}$	Variable used in dynamical classification
$c_1, c_2, c_3, \ldots, c_{j'}$	Variables used for fitting the distribution of object velocity directions about their equatorial plane
dm	Magnitude range
d_1, d_2	Variables used in fitting the inclination distribution
$D\sqrt{N}$	K-S testing statistic
e	Eccentricity of object orbit
$\boldsymbol{e}_{i'}$	Eigenvectors of the covariance matrix $\sigma_{\boldsymbol{jk}}$
$e_{\rm N}$	Eccentricity of Neptune's orbit
$f_{i_{\rm K}}(i_{\rm K})$	Inclination distribution function, representing fraction of objects per degree KBP inclination
$f_{i_{\rm K},n}$	Binned KBP inclination data for the unbiased fraction of the population
$f_{n_v}(\beta)$	Distribution function for the sky density of KBO velocity directions in ecliptic latitude
$f_{n_v}(\beta_{\rm K})$	Distribution function for the sky density of KBO velocity directions in KBP latitude
$f_{q,n}$	Unbiased fraction of the population per unit interval of q for the nth bin
$f_q(q)$	Distribution function that applies to the general (or a subset) population; represents the fraction of objects per unit of q
$f_{\beta_{\rm K},n}$	Binned KBP latitude data for the unbiased fraction of the population
$f_{\beta_{\rm K}}(\beta_{\rm K})$	Distribution function representing the fraction of objects per degree of KBP latitude
g	Variable in the Gaussian plus Lorentzian fit to the inclination distribution
i	Inclination with respect to the ecliptic plane
i'	Index used in orbital solutions; dummy index used in bias removal
$i_{\rm K}$	Inclination with respect to the KBP
$i'_{\rm K}$	Integration variable in bias factors
$i_{{\rm K},j}$	Inclination of the jth object with respect to the KBP
$i_{{\rm K},\max,n}$	Maximum KBP inclination in the nth bin
$i_{{\rm K},\min,n}$	Minimum KBP inclination in the nth bin
$i_{\rm kN}$	Osculating mutual inclination between the orbit of a KBO and that of Neptune
$i_{\rm N}$	Inclination of Neptune's orbit
$i_{\rm subset}$	Inclination of the fitted plane to a subset of objects
$i_{1/2,{\rm K}}$	Variable used in fitting the inclination distribution; represents a half-width of the generalized Lorentzian
j	Discovered-object index
j'	Index for the objects in the nth bin; index for coefficients in the power series fit to sky density of KBO velocity directions
$\boldsymbol{j}, \boldsymbol{k}$	Any one of the six Cartesian phase-space coordinates, $\{x, y, z, \dot{x}, \dot{y}, \dot{z}\}$, used for reference in the covariance matrix $\sigma_{\boldsymbol{jk}}$
k	Search-field index
m	Object magnitude for an ideal case in which the sky is surveyed within a certain wavelength band and for which we define a magnitude system
m_j	Magnitude of the jth object
$m_{\max}$	Maximum magnitude for which a sample has significant sensitivity
$m_{\min}$	Minimum magnitude for which a sample has significant sensitivity
m_0	Magnitude for which the sky density of objects is 1 per square degree (at opposition and for $\beta = 0$)
$m_{1/2,k}$	Magnitude for which the detection efficiency has dropped to $\frac{1}{2}$ for the kth field
$\bar{m}_{2\sigma}$	Average magnitude two standard deviations above the mean sky level for an observing night
$m_{2\sigma,k}$	Magnitude that is two standard deviations above the mean sky level for the shallower exposure of the kth pair of search frames
n	Bin index
$n_{{\rm K},v,0}$	Peak density of object velocity directions on the Kuiper belt equator
$n_v(\beta)$	Sky density of object velocity directions as a function of ecliptic latitude
N	Fixed value (=3) in orbital solutions; number of objects in sample for inclination analysis
N_F	Total number of search fields ($k = 1, \ldots, N_F$)
$N(m)$	Number of objects as a function of magnitude
$N(m, \Delta m)$	Number of objects detected by the survey per magnitude bin of width Δm
N_n	Number of objects in the nth bin
N_q	Total number of bins ($n = 1, \ldots, N_q$) chosen for q
$N_{\rm subset}$	Number of objects in a subset
N_0	Total number of objects ($j = 1, \ldots, N_0$)

p, q, m, n, r, s	Integers used to calculate the mean motion resonances of Neptune (ϕ)
$p(i)$	Probability density for inclinations
$p(i\|\beta)$	Conditional probability density for finding an object with orbital inclination i at latitude β
$p(\beta)$	Probability density for finding KBOs at latitude β
$p(\beta\|i)$	Conditional probability density for finding an object with latitude β at orbital inclination i
$p_{v,\beta}(\beta)$	Probability density function for individual likelihoods used in maximum likelihood fitting
q	Physical or orbital quantity associated with each object; perihelion distance in discovery tables; differential size distribution power-law exponent
q_j	Quantity of interest associated with the jth object
R	Heliocentric distance
T	Instantaneous Tisserand parameter
α	Power-law index for the cumulative magnitude distribution of KBOs; right ascension coordinate in Appendix B
α_p	Right ascension position of a pole for another spherical coordinate system
α_0	Right ascension center coordinate of a search frame
β	Ecliptic latitude (heliocentric in § 5); latitude coordinate in Appendix B
β_b	Latitude at which there is a boundary between two latitude bins
$\beta_{\rm K}$	KBP latitude
$\beta'_{\rm K}$	Integration variable in bias factors
$\beta_{{\rm K},j}$	KBP latitude of the jth object
$\beta_{{\rm K},k}$	KBP latitude center of the kth search field
$\beta_{{\rm K},{\rm max},k}$	Maximum KBP latitude of the kth search field
$\beta_{{\rm K},{\rm max},k,n}$	Maximum KBP latitude on the kth search field contained in the latitude range of the nth bin
$\beta_{{\rm K},{\rm min},k}$	Minimum KBP latitude of the kth search field
$\beta_{{\rm K},{\rm min},k,n}$	Minimum KBP latitude on the kth search field contained in the latitude range of the nth bin
$\beta_{{\rm K},v,{\rm FWHM}}$	Full width at half-maximum of the velocity-direction distribution in Kuiper belt latitude
$\beta_{\rm max}$	Maximum heliocentric ecliptic latitude of object velocity directions; maximum ecliptic latitude of a search frame
$\beta_{\rm min}$	Minimum heliocentric ecliptic latitude of object velocity directions; minimum ecliptic latitude of a search frame
β_0	Ecliptic latitude center coordinate of a search frame
$\beta_0(i, \Omega, \lambda)$	Heliocentric ecliptic latitude as a function of heliocentric ecliptic longitude λ for the equator of a plane with inclination i and ascending node Ω
γ	Constant of proportionality in bias removal
δ	Declination coordinate
δ_p	Declination position of the pole for another spherical coordinate system
δ_0	Declination center coordinate of a search frame
Δm	Width of magnitude bin
$\Delta m_{1/2-2\sigma}$	Difference between the half-efficiency detection magnitude and the frame magnitude that is two standard deviations above background
Δq_n	Width of the nth bin for the quantity q
$\Delta\alpha$	Angular extent of a search frame in right ascension
$\Delta\beta_1$	Angular extent in ecliptic latitude between two corners of a search frame that are aligned in right ascension and declination (see Fig. 21)
$\Delta\beta_2$	Angular extent in ecliptic latitude from the center to a corner closest to the center in ecliptic latitude of a search frame (see Fig. 21)
$\Delta\delta$	Angular extent of a search frame in declination
$\Delta\lambda_{{\rm K},k}(\beta_k)$	Longitude interval within the solid angle covered by the kth frame as a function of KBP latitude
$\Delta\lambda_{\rm max}$	Longitude interval within the solid angle covered by a search frame at latitudes $\beta_0 \pm \Delta\beta_2$
$\Delta\lambda(\beta)$	Longitude interval within the solid angle covered by a search frame as a function of latitude β
$\Delta\Omega_k$	Extent of loss of solid angle from the kth search field
$\epsilon_{\rm max}$	Maximum detection efficiency at bright magnitudes
$\epsilon(m, m_{1/2,k})$	Detection efficiency as a function of magnitude for the kth search frame
$\epsilon(m_j, m_{1/2,k})$	Detection efficiency for the jth object on the kth search frame
$\zeta_{{\rm INC},k,n}$	Likelihood factor for the unbiased inclination distribution for the kth frame and the nth bin
$\zeta_{{\rm INC},n}$	Likelihood factor for the unbiased inclination distribution for the nth bin
ζ_j	Likelihood factor for detecting the jth object over all search fields
$\zeta_{j,k}$	Quantity proportional to the probability or likelihood of finding an object with value q_j in the kth search field
$\zeta_{{\rm LAT},k,n}$	Likelihood factor for the unbiased latitude distribution for the kth frame and the nth bin
$\zeta_{{\rm LAT},n}$	Likelihood factor for the unbiased latitude distribution for the nth bin
$\zeta_{{\rm MAG},j,k}$	Likelihood factors for calculating the unbiased magnitude distribution
$\mathbf{Z}_n$	Quantity proportional to the probability (i.e., the likelihood factor) for finding an object in the nth search bin for a parameter q
θ	Position angle (measured from north through east) of the ecliptic latitude axis in the right ascension–declination coordinate system
λ	Ecliptic longitude (heliocentric in § 5); longitude coordinate in Appendix B

$\lambda_{i'}$	Eigenvalues of the covariance matrix σ_{jk}
$\lambda'_{\rm K}$	Integration variable in bias factors
$\lambda_{{\rm K},{\rm max},k}$	Maximum KBP longitude of the kth search field
$\lambda_{{\rm K},{\rm max},k}(\beta_k)$	Maximum KBP longitude of the kth search field as a function of KBP latitude
$\lambda_{{\rm K},{\rm min},k}$	Minimum KBP longitude of the kth search field
$\lambda_{{\rm K},{\rm min},k}(\beta_k)$	Minimum KBP longitude of the kth search field as a function of KBP latitude
$\lambda_{\rm N}$	Mean longitude of Neptune
λ_0	Ecliptic longitude center coordinate of a search frame
$\xi_{{\rm ang},k}$	Solid-angle component of the likelihood factor for the kth search frame
$\xi_{{\rm ang},k,n}$	Solid-angle component of the likelihood factor for the kth search frame for the nth bin
$\xi_{{\rm inc},k}$	Inclination component of the likelihood factor for the kth search frame
$\xi_{{\rm inc},k,n}$	Inclination component of the likelihood factor for the kth search frame for the nth bin
$\xi_{{\rm lat},k}$	Latitude component of the likelihood factor for the kth search frame
$\xi_{{\rm mag},k}$	Magnitude component of the likelihood factor the kth search frame
$\xi_{{\rm mag},k,n}$	Magnitude component of the likelihood factor for the kth search frame for the nth bin
ϖ	Mean longitude of perihelion of an object orbit
$\varpi_{\rm N}$	Mean longitude of perihelion of Neptune
$\rho_{\rm lat}(\beta_{\rm K})$	Relative density of objects per square degree as a function of KBP latitude
$\sigma(f_{q,n})$	Error in the unbiased fraction of the population
σ_i	Inclination error of object orbit
$\sigma_{i,{\rm subset}}$	Standard deviation of the fitted inclination of the plane (relative to the ecliptic) for a subset of objects
σ_{jk}	Covariance matrix for orbital solutions
σ_m	Parameter that characterizes the width of the transition between the maximum detection efficiency and zero
σ_p	Error in pole of object orbit
$\sigma_{\rm subset}$	Standard deviation for one object of a subset in defining a mean orbit plane for the subset
σ_Ω	Node error of object orbit
σ_1, σ_2, σ_3, σ_4	Variables in fits to the inclination distribution
$\Sigma(m, 0)$	Number of bodies in the mean KBP, per unit magnitude interval, per square degree
$\Sigma(<m)$	Sky density of KBOs brighter than magnitude m
$\Sigma(m, \beta_{\rm K})$	Distribution function in magnitude and latitude relative to the KBP
$\Sigma(<m, \beta_{\rm K})$	Sky density of KBOs brighter than magnitude m at KBP latitude $\beta_{\rm K}$
ϕ	Resonant argument that characterizes the strongest mean motion resonances established by Neptune exterior to its own orbit
Ω	Longitude of ascending node of orbit or plane
Ω_k	Net solid angle for the kth search field
$\Omega_{\rm N}$	Longitude of ascending node of Neptune
$\Omega_{N_F,0}(m)$	Equivalent solid angle at $\beta_{\rm K} = 0$ covered by all fields of the survey
Ω_s	Solid angle of sky exposure
$\Omega_{\rm subset}$	Ascending node of the fitted plane to a subset of objects
$\Omega(<\beta_b)$	Amount of solid angle within a rectangular element that is below latitude β_b

REFERENCES

Allen, R. L., Bernstein, G. M., & Malhotra, R. 2002, AJ, 124, 2949
Bernstein, G., & Khushalani, B. 2000, AJ, 120, 3323
Bernstein, G. M., Trilling, D. E., Allen, R. L., Brown, M. E., Holman, M., & Malhotra, R. 2004, AJ, 128, 1364
Bevington, P. R., & Robinson, D. K. 2003, Data Reduction and Error Analysis for the Physical Sciences (3rd ed.; New York: McGraw-Hill)
Brouwer, D., & van Woerkom, A. J. J. 1950, The Secular Variations of the Orbital Elements of the Principal Planets (Astron. Pap. Am. Ephemeris Naut. Alm., 13, 81) (Washington: GPO) (BvW)
Brown, M. E. 2001, AJ, 121, 2804
Brown, M. E., & Pan, M. 2004, AJ, 127, 2418
Brown, M. E., Trujillo, C., & Rabinowitz, D. 2004, ApJ, 617, 645
Buie, M. W., et al. 2003, Earth Moon Planets, 92, 113
Chiang, E. I. 2002, ApJ, 573, L65
Chiang, E. I., & Brown, M. E. 1999, AJ, 118, 1411
Chiang, E. I., & Jordan, A. B. 2002, AJ, 124, 3430
Chiang, E. I., et al. 2003a, AJ, 126, 430
Chiang, E. I., Lovering, J. R., Millis, R. L., Buie, M. W., Wasserman, L. H., & Meech, K. J. 2003b, Earth Moon Planets, 92, 49
Collander-Brown, S. J., Melita, M. D., Williams, I. P., & Fitzsimmons, A. 2003, Icarus, 162, 22
Doressoundiram, A., Peixinho, N., de Bergh, C., Fornasier, S., Thebault, P., Barucci, M. A., & Veillet, C. 2002, AJ, 124, 2279 (erratum 125, 1629 [2003])
Duncan, M., Quinn, T., & Tremaine, S. 1988, ApJ, 328, L69
Duncan, M. J., & Levison, H. F. 1997, Science, 276, 1670
Duncan, M. J., Levison, H. F., & Budd, S. M. 1995, AJ, 110, 3073
Edgeworth, K. E. 1949, MNRAS, 109, 600
Elliot, J. L. 2001a, IAU Circ. 7733
———. 2001b, IAU Circ. 7765
———. 2003, IAU Circ. 8235
Elliot, J. L., & Kern, S. D. 2003, Earth Moon Planets, 92, 375
Fernández, J. A. 1980, MNRAS, 192, 481
Gladman, B., Holman, M., Grav, T., Kavelaars, J., Nicholson, P., Aksnes, K., & Petit, J.-M. 2002, Icarus, 157, 269
Gladman, B., Kavelaars, J. J., Petit, J.-M., Morbidelli, A., Holman, M. J., & Loredo, T. 2001, AJ, 122, 1051
Goldreich, P., Lithwick, Y., & Sari, R. 2002, Nature, 420, 643
Gomes, R. 2003a, Nature, 426, 393
Gomes, R. S. 2003b, Icarus, 161, 404
Gulbis, A. A. S., Elliot, J. L., & Kane, J. F. 2005, Icarus, submitted
Hahn, J. M., & Malhotra, R. 1999, AJ, 117, 3041
Holman, M. J., & Wisdom, J. 1993, AJ, 105, 1987
Jewitt, D. 2003, Earth Moon Planets, 92, 465
Jewitt, D., & Luu, J. 1993, Nature, 362, 730
Jewitt, D., Luu, J., & Chen, J. 1996, AJ, 112, 1225
Jewitt, D., Luu, J., & Trujillo, C. 1998, AJ, 115, 2125
Jewitt, D. C., & Luu, J. X. 2000, in Protostars and Planets IV, ed. V. Mannings, A. P. Boss, & S. S. Russell (Tucson: Univ. Arizona Press), 1201
Joss, P. C. 1973, A&A, 25, 271
Kenyon, S. J., & Luu, J. X. 1998, AJ, 115, 2136
———. 1999, AJ, 118, 1101

Kuiper, G. P. 1951, in Astrophysics, ed. J. A. Hynek (New York: McGraw-Hill), 357
Larsen, J. A., et al. 2001, AJ, 121, 562
Levison, H. F., & Duncan, M. J. 1994, Icarus, 108, 18
Levison, H. F., & Stern, S. A. 2001, AJ, 121, 1730
Malhotra, R. 1995, AJ, 110, 420
———. 1996, AJ, 111, 504
Millis, R. L. 2003, IAU Circ. 8251
Millis, R. L., Buie, M. W., Wasserman, L. H., Elliot, J. L., Kern, S. D., & Wagner, R. M. 2002, AJ, 123, 2083 (Paper I)
Muller, G. P., Reed, R., Armandroff, T., Boroson, T. A., & Jacoby, G. H. 1998, Proc. SPIE, 3355, 577
Murray, C. D., & Dermott, S. F. 1999, Solar System Dynamics (Cambridge: Cambridge Univ. Press)
Nesvorný, D., Roig, F., & Ferraz-Mello, S. 2000, AJ, 119, 953
Noll, K., Stephens, D., Grundy, W., Cruikshank, D., Tegler, S., & Romanishin, W. 2002a, IAU Circ. 8034
Noll, K. S. 2003, Earth Moon Planets, 92, 395
Noll, K. S., et al. 2002b, AJ, 124, 3424
Osip, D. J., Kern, S. D., & Elliot, J. L. 2003, Earth Moon Planets, 92, 409
Press, W. H., Teukolsky, S. A., Vetterling, W. T., & Flannery, B. P. 1992, Numerical Recipes in FORTRAN (2nd ed.; Cambridge: Cambridge Univ. Press)
Schechter, P. L., Mateo, M., & Saha, M. 1993, PASP, 105, 1342
Sebring, T. A., Dunham, E. W., & Millis, R. L. 2004, Proc. SPIE, 5489, 658
Sheppard, S. S., & Jewitt, D. 2004, AJ, 127, 3023
Stokes, G. H., Evans, J. B., & Larson, S. M. 2002, in Asteroids III, ed. W. F. Bottke, A. Cellino, P. Paolicchi, & R. P. Binzel (Tucson: Univ. Arizona Press), 45
Tegler, S. C., Romanishin, W., & Consolmagno, G. J. 2003, ApJ, 599, L49
Tiscareno, M. S., & Malhotra, R. 2003, AJ, 126, 3122
Trujillo, C. A., & Brown, M. E. 2002, ApJ, 566, L125
———. 2003, Earth Moon Planets, 92, 99
Trujillo, C. A., Jewitt, D. C., & Luu, J. X. 2001, AJ, 122, 457
Veillet, C., et al. 2002, Nature, 416, 711
Virtanen, J., Tancredi, G., Muinonen, K., & Bowell, E. 2003, Icarus, 161, 419
Weidenschilling, S. J. 2002, Icarus, 160, 212
Wisdom, J., & Holman, M. 1991, AJ, 102, 1528